



Progress Report

NASA Headquarters
Earth Science Division
Land Cover/Land Use Change Program

Comparison of the Advanced Wide Field Sensor to Landsat for Supplying General Land Cover Land Use Change Detection Products Needed for NASA LCLUC Program Science

NASA Grant Number NNX09AR41G

Principal Investigator
Mary Pagnutti

e-mail: mpagnutti@i2rcorp.com

November 8, 2010

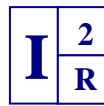
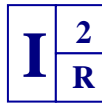


Table of Contents

Table of Contents	2
Project Background and Goals.....	3
Year 1 Achievements:.....	8
Defined Overall Approach	8
Identified and Obtained AWiFS Imagery	8
Validated Relative Radiometry Between Camera Modules.....	9
Generated planetary and surface reflectance maps for AWiFS scenes	11
Evaluated land cover classification schemes	14
Analyzed change in reflection as a function of view angle.....	16
Began developing a statistical BRDF model based on a modified Walthall formulation.....	17
Year 2 Plan/Objectives	23
Summary	24
References	25
Appendices.....	27
Appendix 1. List of Acquired AWiFS scenes	27
Appendix 2. Relative Radiometry Results	29
Appendix 3. Reflectance Variation as a Function of Sensor View Angle	44



Project Background and Goals

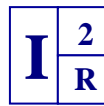
This report summarizes our first year's progress on developing a statistical model to describe the Bidirectional Reflection Distribution Function (BRDF) for the Advanced Wide Field Sensor (AWIFS) and highlights collaborations with the University of Maryland (UMD) and the US Geological Survey (USGS) Center for Earth Resources Observation and Science (EROS) Data Center (EDC).

For over 38 years, the Land Cover Land Use Change (LCLUC) community has heavily relied upon Landsat data to produce regional to global-scale mapping products depicting land cover, land use distributions and terrestrial environmental changes. The current on-orbit Landsat capability for monitoring the land masses of the world at a 30-meter spatial resolution however, may be lost before the next Landsat is available, thus producing a Landsat data gap. The Landsat-5 Thematic Mapper (TM), launched in 1984, is 23 years beyond its expected three year mission life (<http://landsat.gsfc.nasa.gov/about/landsat5.html>). The Landsat-7 Enhanced Thematic Mapper plus (ETM+) lost functionality of its scan line corrector (SLC) in May 2003 and as a result the ETM+ line of sight traces a zigzag pattern across the ground track leaving striped gaps within a scene. Imagery from multiple acquisitions must be merged together to generate a single scene (<http://landsat.gsfc.nasa.gov/about/landsat7.html>). The newest planned Landsat observatory, Landsat Data Continuity Mission (LDCM), is under development, but will not become operational until early 2013 (<http://ldcm.nasa.gov/>).

In 2005 the Office of Science and Technology Policy (OSTP) initiated an effort to stabilize policy and funding for operational land imaging. This resulted in the formulation of the National Land Imaging Program (NLIP), which identified as its central concerns: (1) the expected Landsat data gap and (2) unaffordable requirements for more frequent imagery. To address these concerns, the NLIP specifically recommended augmenting US government systems with data from low-cost international and commercial US systems. The NLIP recommendations are consistent with the most recent Decadal Survey, which concluded that growth in non-US government capability and availability, coupled with US funding constraints, will ultimately increase US Federal agencies' reliance on commercial and international data sources.

Currently there are more than 50 operational satellite land imaging systems, most of which are international, with spatial resolutions comparable or better than Landsat. Most are pushbroom systems in contrast with the cross track scanner technology used in previous and current on-orbit Landsats. Many of these systems are quite capable and can augment Landsat systems due to their spatial resolution characteristics as well their relatively short revisit times. Many of these satellite systems are capable of achieving weekly or better revisits by: being part of a small satellite constellation; incorporating sensors having a wide field of view; or by carrying multiple sensors on a spacecraft.

Pushbroom cameras utilize an array of detectors in the cross track direction whereby the motion of the spacecraft produces an image. Pushbroom cameras are preferred over cross track sensors since they are smaller, lighter, and produce a higher signal-to-noise ratio. The Landsat Data Continuity Mission (LDCM) is currently planned to have a pushbroom sensor on-board. Pushbroom sensors are, however, susceptible to an array of imaging artifacts not routinely observed with cross track scanners. These include relatively large band-to-band mis-registration,



increased stray light, and a point spread function that can vary as a function of band and position within the image. In addition to these artifacts, multiple cameras on a single satellite can introduce radiometric differences between images acquired with different cameras. In principle most of these artifacts and image differences can be corrected in post processing.

In anticipation of the Landsat data gap, in 2005, the Federal agencies responsible for Landsat program management—NASA, Department of Interior/USGS, and Department of Commerce/NOAA—convened a Landsat Data Gap Study Team. The Team recognized that no current or near-future satellite system could fully replace the Landsat satellites but concluded that archiving data from comparable systems into the National Satellite Land Remote Sensing Data Archive (NLSRSDA) at the USGS EDC could reduce the impact of a Landsat data gap. The Study Team assessed the basic characteristics of multiple systems and identified sensors aboard the China/Brazil Earth Resources Satellite (CBERS-2) and the Indian Remote Sensing (IRS) P6 RESOURCESAT-1 satellite as two of the more promising sources of Landsat-like data.

In order to use these new alternative data sets in concert with the long term Landsat archive, systematic geometric and atmospheric effects need to be understood and removed. This project, in collaboration with the “Comparison of the IRS Advanced Wide Field Sensor to Landsat for Supplying General Land Cover Land Use Change Detection Products Needed for NASA LCLUC Program Science” project performed at the University of Maryland (UMD) Geography Department under the direction of Dr. Sam Goward and the “Cross-calibration of the current Landsat sensors with foreign Landsat-class sensors for long-term monitoring of land surface processes” project performed at the USGS EDC by Mr. Gyanesh Chander, begins to evaluate the technical merits of the Advanced Wide Field Sensor (AWiFS) on-board the IRS-P6 RESOURCESAT-1 satellite to augment or potentially, in the case of a data gap, replace Landsat data. While the AWiFS camera module, shown in Figure 1, collects data similar to Landsat, system differences including reduced (lower) spatial resolution, reduced number of spectral bands, multiple cameras and larger off-axis viewing geometry, may impact LCLUC products. Key differences between the two sensors are shown in Table 1.

A significant difference between Landsat and AWiFS is the wider swath of AWiFS, shown in Figure 2. Although this wider swath significantly improves the revisit time of the system, it also increases the degree of off-axis imaging. AWiFS acquires imagery up to ~24 degrees from Nadir as compared to 7.5 degrees for Landsat. This off-axis viewing causes changes in surface reflection and increased atmospheric effects compared to Nadir viewing. Differences in the Normalized Difference Vegetation Index (NDVI) and other derived parameters related to variations in viewing geometry and solar zenith angle at the time of observation may make it difficult to distinguish between expected intra-vegetation type variability (i.e., seasonal or inter-annual variability) and significant land cover change over time (Los et al., 2005; Gutman et al., 1995; Gutman, 1998).



Figure 1. AWiFS camera module imagery.

A second major difference between Landsat and AWiFS is the use of multiple pushbroom cameras within the RESOURCESAT-1 satellite, shown in Figure 3, versus a single cross-track scanner system. The AWiFS camera is split into two separate electro-optic modules (AWiFS-A and AWiFS-B) tilted by 11.94 degrees with respect to Nadir. Imagery from each camera module is split into two separate scenes for ease of use. AWiFS-A acquires quad A and B scenes and AWiFS-B acquires quad C and D scenes. Each AWiFS path/row location therefore has four different possible scenes or quads. The use of multiple pushbroom cameras decreases revisit time, but also creates the increased likelihood of several imaging artifacts not seen in historical Landsat

Table 1. Comparison of Landsat and AWiFS key characteristics.

Parameter	Landsat		AWiFS	
	Band	Microns	Band	Microns
Spectral	1 (Blue)	0.45–0.52	–	NA
	2 (Green)	0.52–0.60	1 (Green)	0.52–0.59
	3 (Red)	0.63–0.69	2 (Red)	0.62–0.68
	4 (NIR)*	0.76–0.90	3 (NIR)	0.77–0.86
	5 (SWIR-1)*	1.55–1.75	4 (SWIR-1)	1.55–1.70
	6 (TIR)*	10.4–12.5	–	NA
	7 (SWIR-2)	2.08–2.35	–	NA
GSD	30-meter at Nadir		56-meter at Nadir	
Quantization	8 bits		10 bits	
Onboard Calibration	Yes		No	
Revisit Time	16 days		5 days	
Orbital-Repeat Cycle	16 days		24 days	
Off-Axis Viewing Capability	Up to 7.5 degrees off Nadir		Up to 24.3 degrees off Nadir	
Altitude	705 km		817 km	
Swath	185 km		737 km (combined)	
Architecture	Cross-track scanner		Pushbroom	

*NIR = near infrared; SWIR = shortwave infrared; TIR = thermal infrared

A third difference between the two systems is the available spectral bands. The AWiFS has only four bands in the visible to near-infrared spectral region as shown in Figure 4. These four bands roughly correspond to Landsat bands 2, 3, 4 and 5. Unlike the Landsat ETM+ sensor, the AWiFS does not have a blue band, SWIR-2 band or thermal infrared band.

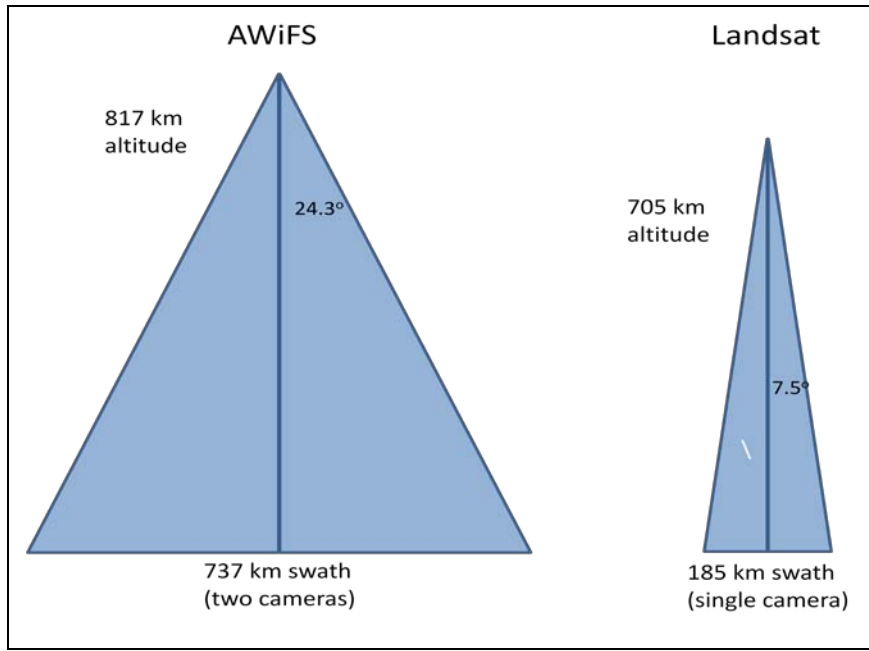


Figure 2. AWiFS collection geometry compared to Landsat

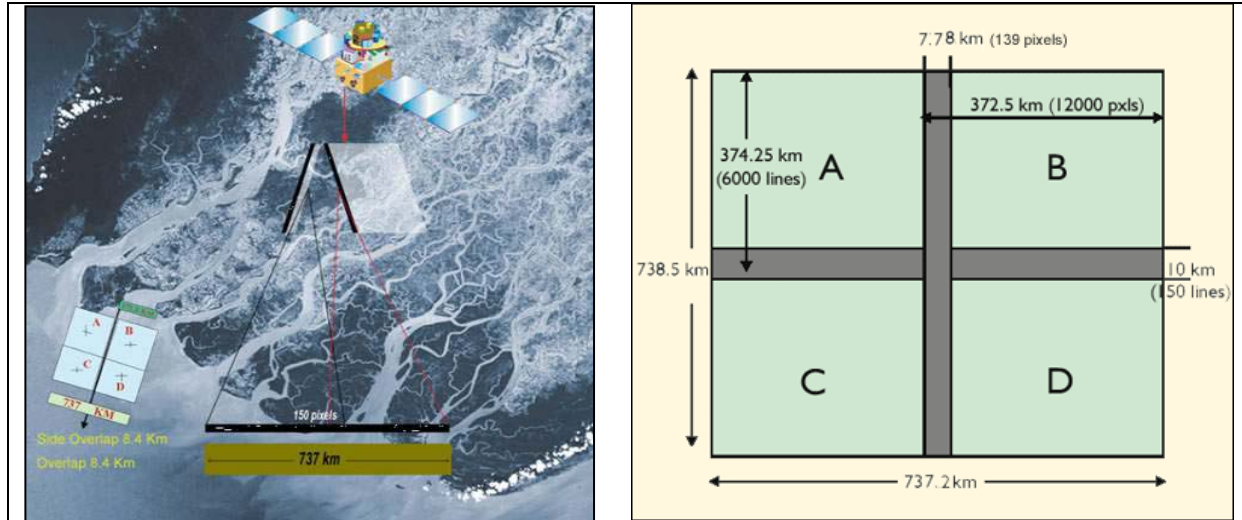


Figure 3. AWiFS camera arrangement and associated scene quads

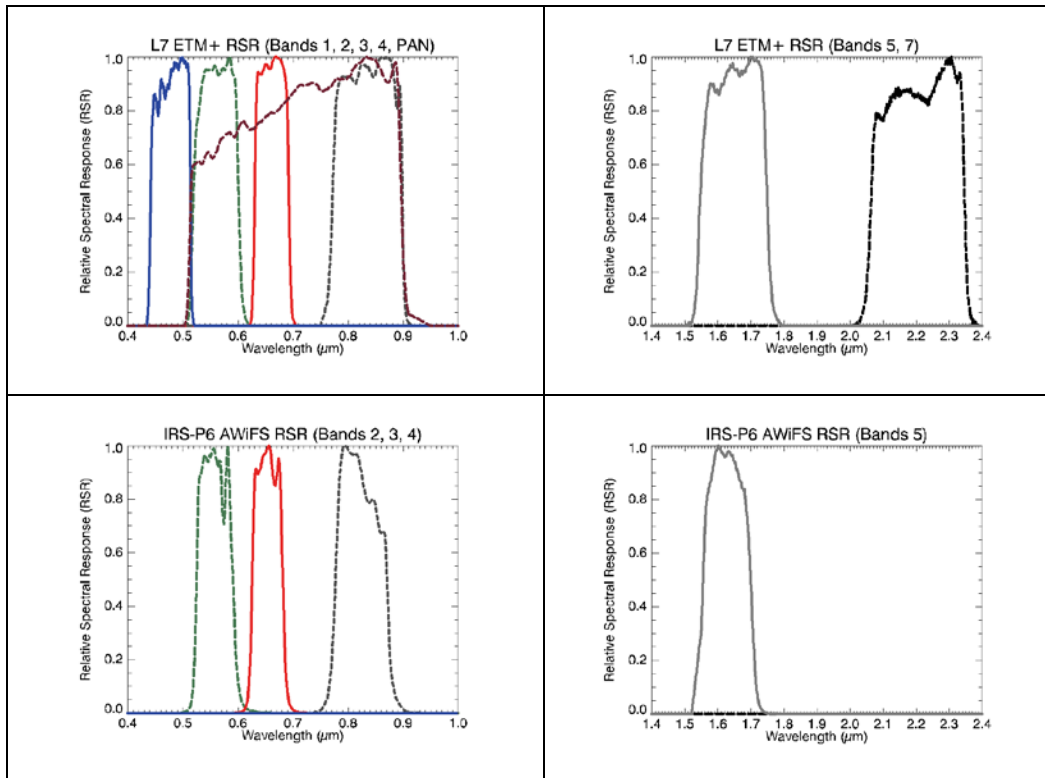
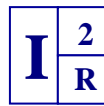


Figure 4. AWIFS spectral bands as compared to Landsat-7 (Chander et al, 2010)

To begin to understand how the characteristics of AWIFS will affect LCLUC research, this project addresses detecting variation in reflectance caused by BRDF effects due to off-Nadir viewing geometries present within the large camera swath width coupled with varying seasonal solar geometries. During this first year we have:

- Defined an overall approach
- Acquired 84 AWIFS scenes, predominantly from the AWIFS-B camera module, over the US and parts of Canada and provided a subset to UMD
- Collaborated with the USGS EDC and reviewed AWIFS radiometry in the context of a 4-quad overlapped “super scene”
- Developed methodology to atmospherically correct AWIFS imagery using NASA MODIS aerosol and water vapor products and began extending it as an atmospheric look-up table
- Produced surface reflectance and top-of-atmosphere (TOA) planetary reflectance maps for several AWIFS images and provided a subset to UMD
- Generated land cover maps based on TOA planetary reflectance maps and compared several land cover classification schemes, both supervised and unsupervised for several AWIFS images
- Developed methodology to evaluate surface reflectance and TOA reflectance values as a function of solar zenith and azimuth angles, and sensor viewing zenith and azimuth angles for a single land cover class



- Began developing a statistical BRDF model based on a modified Walthall formulation.

In addition to collaborating with the USGS EDC and the UMD, we are working closely with Mr. Robert Tetrault at the USDA Foreign Agriculture Service (FAS). The USDA maintains a Satellite Imagery Archive (SIA), which holds the largest collection of US government procured AWIFS imagery. The FAS has also worked extensively with AWIFS imagery, both operationally and on USDA application projects.

Year 1 Achievements:

Defined Overall Approach

For this project, we chose to develop a statistical model of surface BRDF that does not rely on physical parameters to characterize its functional shape. Our approach follows that of Walthall et al. 1985 who used three parameters to define a statistical BRDF model with reasonable success. This type of model has been widely used even though it does not describe some readily observed features such as the hotspot peak. Danaher et al. 2002 modified the Walthall model and tested it against Landsat data sets converted to planetary reflectance for a limited number of land cover classes. In doing so, these researchers considered three different models with increasing complexity and found that the simplest linear model provided the best results. Since we have access to a limited number of data sets, we decided to begin our two-year study with the simplest of the three Danaher statistical BRDF models. Following Danaher, we decided to initiate our study using planetary reflectance values. As we obtain additional AWIFS data and begin to understand the statistical variation in our results, we will consider alternate models found within the literature by Danaher and others.

We understand the importance of an accurate radiometric AWIFS calibration in order to successfully determine BRDF effects, but with the exception of early NASA-funded vicarious calibration efforts (Blonski et al. 2005) and limited cross calibration with Landsat data sets (Chander et al. 2010) there has been a lack of systematic post launch radiometric calibration monitoring by the Indian Space Research Organization (ISRO) and others. During this project we elected to utilize the radiometric calibration coefficients provided by ISRO with AWIFS imagery, as these are the coefficients a researcher would likely use. If the separately funded LCLUC project performed by the USGS EDC recommends that alternate calibration coefficients should be used, we plan to update our analysis.

Identified and Obtained AWIFS Imagery

At the start of this project we identified and obtained 84 AWIFS scenes from the USDA Satellite Imagery Archive. Data obtained from this archive is comprised of 10 bit orthorectified imagery acquired in 2008. The scenes that were acquired were predominately in the US mid-west over agricultural areas. They are, like the vast majority of the archive, predominantly B and D quad scenes taken with the AWIFS-B camera module. For the most part we selected adjacent overlapping scenes within several seasons. By doing so we obtained imagery acquired with seasonally different solar illumination geometry and, when looking at the overlap areas, we have obtained imagery acquired at different viewing geometries. An overview of our data set, sorted by season is shown in Figure 5.

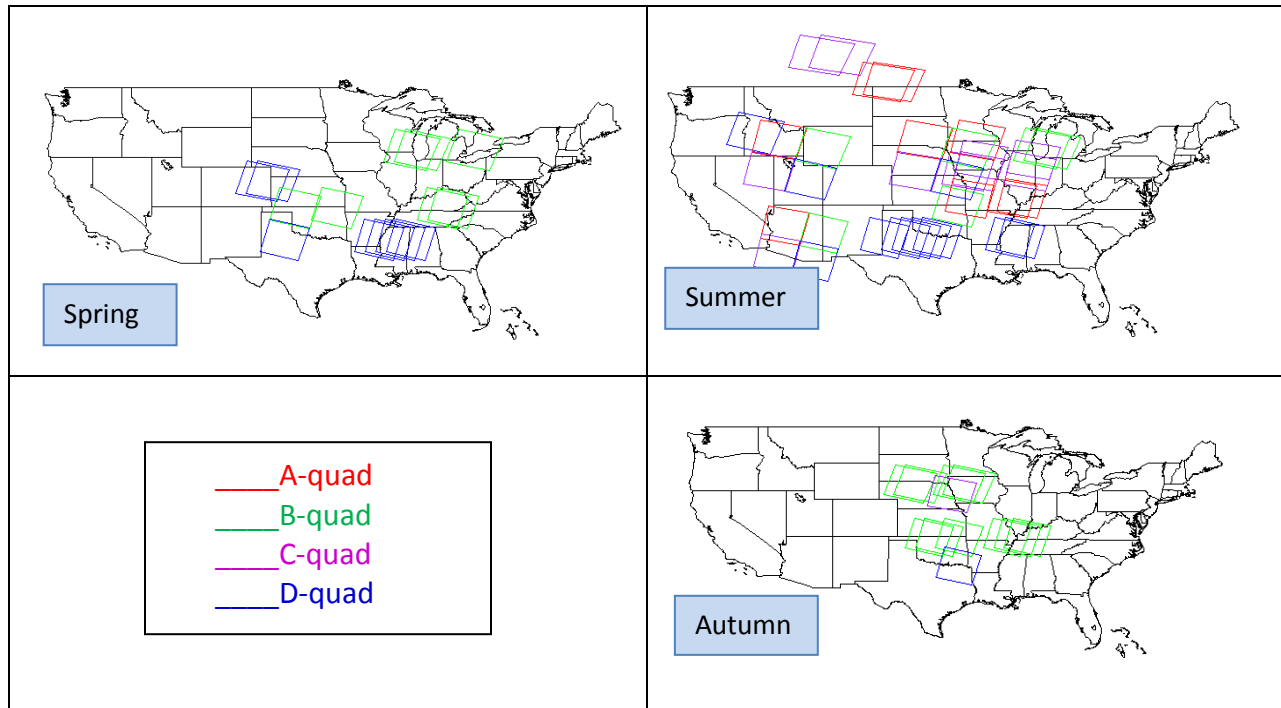


Figure 5. Acquired AWIFS scenes sorted by season

We also have access to the 104 scenes that the NASA John C. Stennis Space Center (SSC) calibration-validation team used to perform imagery evaluations. These scenes are a mix of 8 and 10 bit georectified and orthorectified products, predominately acquired in 2004-2006. Some of these scenes were originally acquired from the USDA archive, while others were acquired from the Space Imaging (now GeoEye) archive.

Finally, we are sharing a limited number of scenes from the USGS archive as part of this project's collaboration. This includes a 4-quad super scene that the USGS EDC ordered.

A complete list of all data obtained for use within this project is summarized in Appendix 1.

Validated Relative Radiometry Between Camera Modules

To begin our analysis, we first compared the relative radiometric performance of the two camera modules. Consistent radiometric performance between the two camera modules is important to establish consistent surface reflectance values. Without that, differences attributable to different viewing geometries may actually be due to different camera module radiometric calibrations. To compare the radiometric calibration between the two camera modules we utilized three sets of 4-quad super scenes. Each super scene contains an overlap area approximately 7.8 km wide (139 pixels) acquired by both camera modules at the same time as shown in Figure 3 and Figure 6. Radiometrically calibrated pixels from quads A and B (or alternatively C and D) were georeferenced, and then mapped to each other to create a one to one pixel correspondence between the two cameras. The pixel values were then plotted against each other as shown for Band 2 in Figure 7. Perfect relative radiometry would yield a straight line, with a slope of 1.

A linear fit was performed on the data to provide a quantitative measure of the agreement of the cameras and shown as a straight line in the figure. In this example, the linear fit produced a slope of 0.98 and a y-intercept of 3.2.

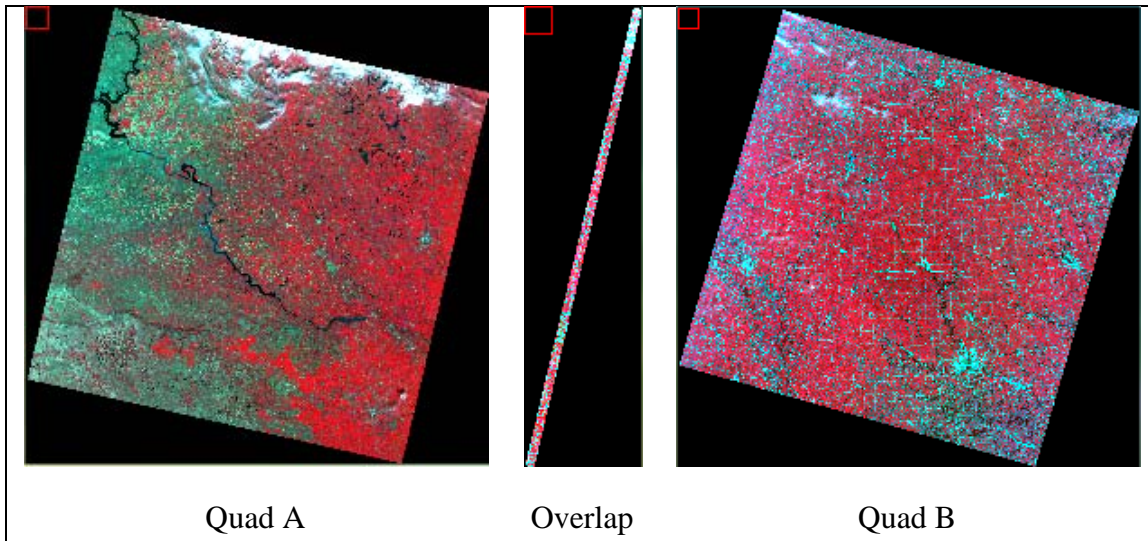


Figure 6. Two AWIFS scenes and their overlap (path 268, row 40, acquired Aug. 2, 2009)

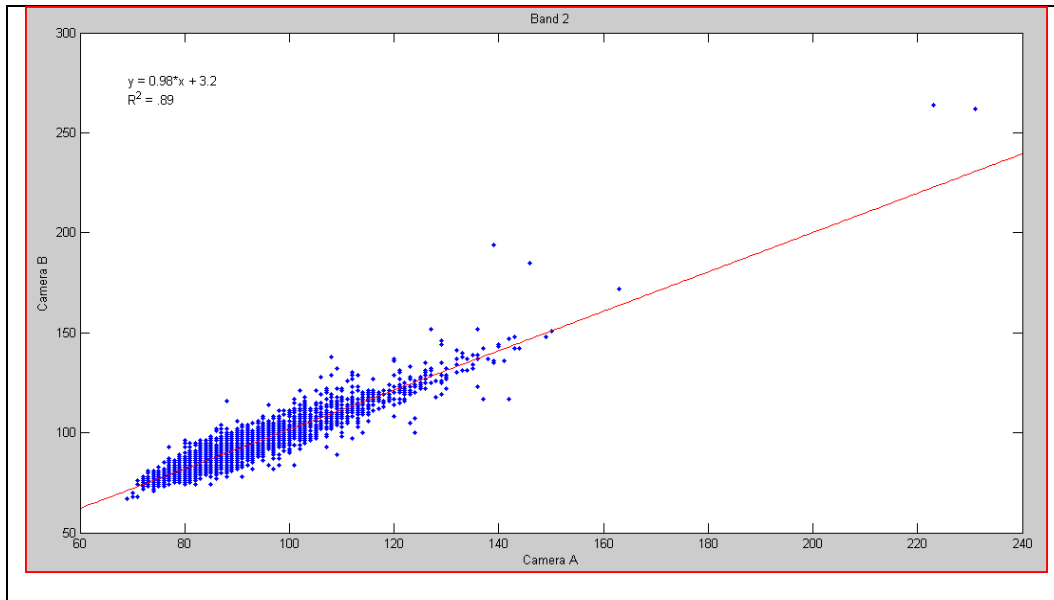


Figure 7. Sample scatter plot comparison of AWIFS A and B cameras in Band 2 (path 268, row 40, acquired Aug. 2, 2009)

We also evaluated the relative radiometric performance of the two camera modules with a slightly different approach, using a 50 pixel average as the basis of comparison instead of single pixel to pixel comparisons. This alternate approach allowed us to compare our results to those obtained by the USGS EDC using a similar method. Pixel averaging increases the signal-to-noise in the calculation and as a result should produce more reliable and consistent results. A sample of these pixel averaged results for the same AWIFS scene is shown in Figure 8. In this case the linear fit produced a slope of 0.97 and a y-intercept of 4.7.

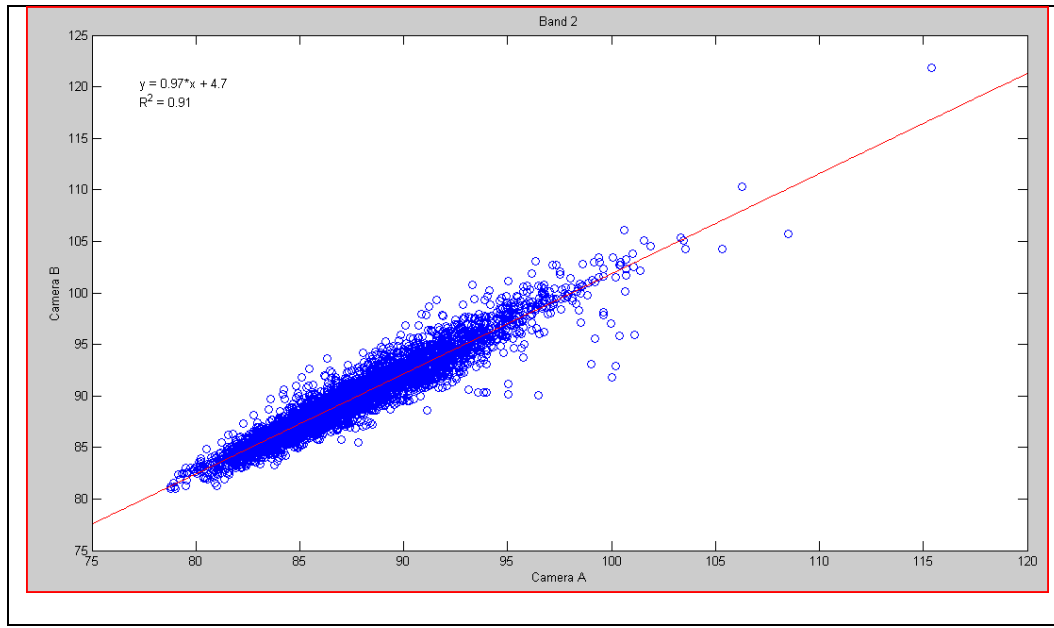


Figure 8. Sample 50 pixel average comparison of AWIFS A and B cameras in Band 2 (path 268, row 40, acquired Aug 2, 2009)

For the most part, the two methods produced very similar results. There were however a small number of instances whereby the pixel-to-pixel comparison showed unexpected large differences between camera modules. After analysis we concluded that this was due to extremely homogeneous agricultural scenes (showing very little difference in reflectance values) that when compared had a small number of noisy points (outliers) driving the linear fit. The 50 pixel average approach reduced the magnitude of the outliers and therefore improved comparisons between the two quads.

Our brief relative radiometric analysis concluded that there was reasonably good agreement between the two AWIFS cameras. Complete results of our analysis are shown in Appendix 2. Absolute radiometric performance of AWIFS is being assessed at the USGS EDC under a separate LCLUC funded project.

Generated planetary and surface reflectance maps for AWIFS scenes

After gaining confidence in the consistent nature of the two AWIFS camera module's radiometric performance, we generated both planetary and surface reflectance maps for each of the four multispectral band images associated with several AWIFS acquisitions. Each reflectance map we generated therefore contains reflectance values associated with band integrated radiance values.

It should be noted that absolute radiometry is based on calibration values provided by the ISRO. These were developed prelaunch and have not been updated. Since planetary and surface reflectance values are both affected by absolute radiometry, we are coordinating closely with the USGS EDC and following their radiometric evaluation studies. If the USGS EDC discovers a large deviation in absolute radiometric calibration coefficients, we will update our results where appropriate.

Planetary Reflectance

Planetary reflectance, also known as top-of-atmosphere (TOA) reflectance, is a first-order approximation that accounts for solar geometry and Earth-sun distance; it uses no knowledge of the atmosphere over the scene (<http://landsathandbook.gsfc.nasa.gov/handbook.html>). The equation used is commonly found in the literature as:

$$\rho_{TOA} = \frac{\pi d^2 L_{TOA}}{E_{sun} \cos \theta} \quad (1)$$

Where: ρ_{TOA} is the target or pixel of interest planetary reflectance; L_{TOA} is the top-of-atmosphere radiance; E_{sun} is the exo-atmospheric spectral irradiance (Thuillier et al., 2003); θ is the angle of incidence; and d is the Earth-Sun distance.

A sample planetary reflectance map is shown below in Figure 9 (RGB using NIR, green, and red bands respectively) of the AWiFS path 265, row 45, quad D scene, acquired on April 18, 2008. Alongside the reflectance map is a histogram plot for each of the bands. TOA planetary reflectance maps were generated for all of the AWiFS imagery acquired during the first year of this project.

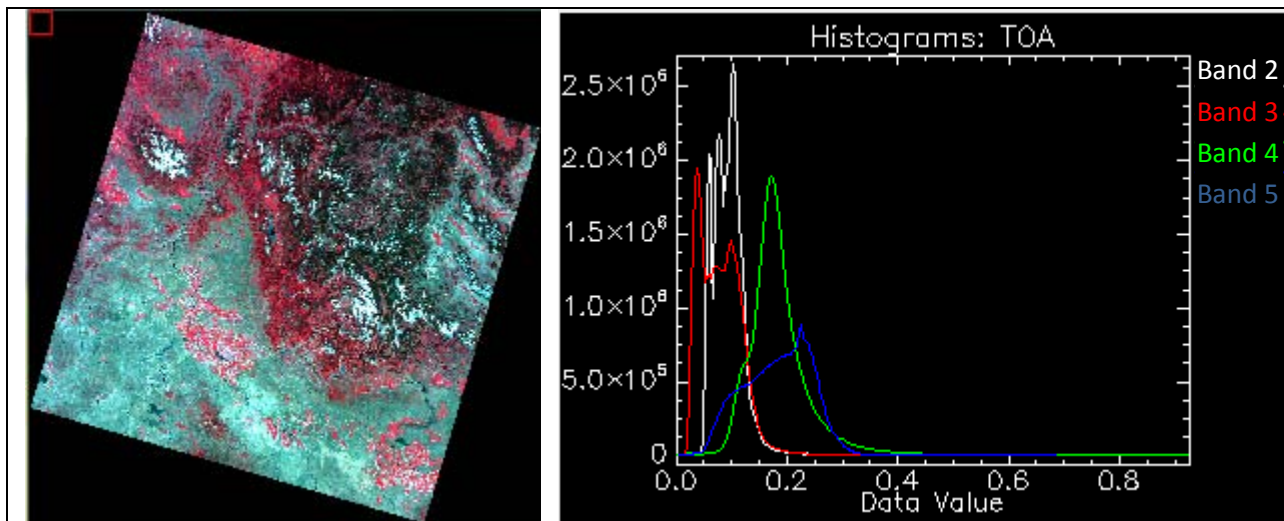


Figure 9. Sample AWiFS planetary reflectance map (RGB using NIR, green, and red respectively) and planetary reflectance histogram plots (all bands) for path 247, row 36, quad D, acquired June 22, 2006

Surface Reflectance

Atmospheric correction is the process of converting satellite signals (at-sensor radiance) to surface reflectance. In general, surface reflectance yields more accurate results than planetary reflectance. New methods were required to atmospherically correct the imagery since the AWiFS band combination cannot be used with existing Landsat atmospheric correction algorithms. For this project we utilized a modified spherical albedo method (Tanre et. al, 1979) to generate surface reflectance maps as shown in the equation below.

$$\rho_T = \left(\rho_{TOA} - \rho_0 - \frac{B\rho_{bg}}{1-s\rho_{bg}} \right) \frac{(1-s\rho_{bg})}{A} \quad (2)$$

Where: ρ_T is the target pixel surface reflectance; ρ_{TOA} is the top-of-atmosphere planetary reflectance; ρ_{bg} is the background reflectance; and A, B, s, and ρ_0 are constants that depend on atmospheric properties and geometry.

Near-coincident NASA observations and the Moderate Resolution Transmittance (MODTRAN) radiative transmission code (Berk, 1999) were used with this formulation to derive the atmospheric gases and aerosols required to invert TOA reflectance values into surface reflectance. Moderate Resolution Imaging Spectrometer (MODIS) MOD04 aerosol optical thickness and MOD05 total perceptible water data products from the Terra (EOS-AM) satellite were obtained and utilized. AWIFS and Terra are both sun-synchronous and are within 1 hour of each other. Daily ozone estimates were also obtained from NASA's Ozone Monitoring Instrument (OMI) onboard the EOS-Aura satellite and used in this formulation. This atmospheric correction method is valid only in cases where the atmosphere is relatively stable and has been validated with commercial high spatial resolution IKONOS and QuickBird imagery (Pagnutti et. al, 2005).

A sample surface reflectance map is shown below in Figure 10 for the same image shown above (RGB of AWIFS path 247, row 36, quad D acquired on June 22, 2006). As with the planetary reflectance map, histogram plots for each of the bands are also provided. While the images and histograms are similar, the histograms associated with the surface reflectance product are tighter and more Gaussian in shape than those generated from the planetary reflectance product.

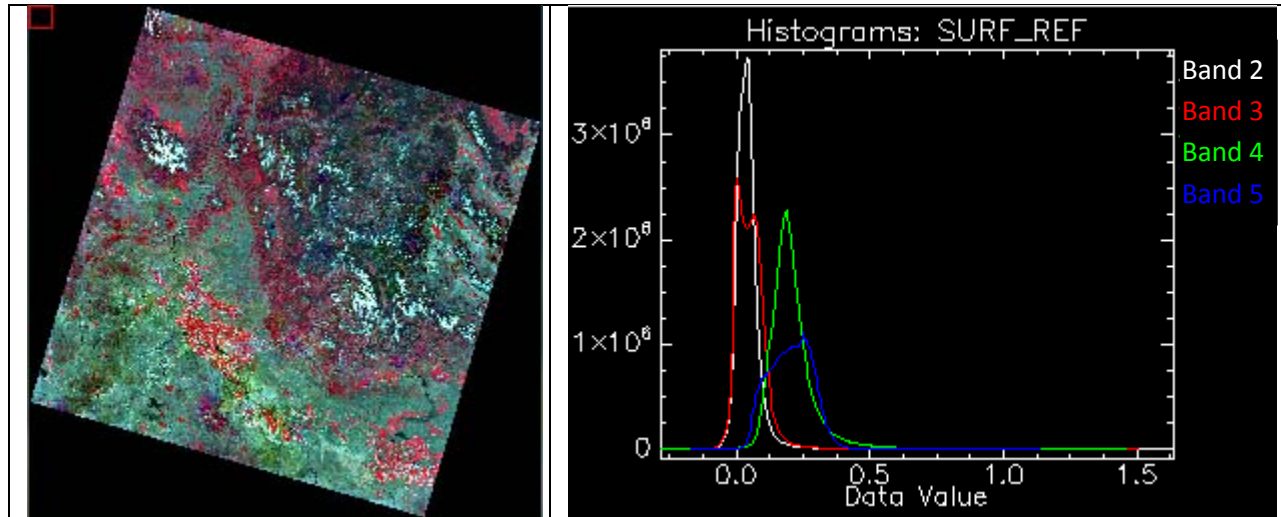
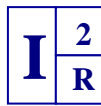


Figure 10. Sample AWIFS surface reflectance map (RGB using NIR, green, and red respectively) and surface reflectance histogram plot (all bands) for path 247, row 36, quad D, acquired June, 22 2006.

Eight AWIFS scenes were atmospherically corrected during this first year. Since the atmospheric correction algorithm is computationally time consuming and there are a significant number of scenes we plan to evaluate during this project, work began during this first year to



extend the atmospheric correction approach to allow for an atmospheric look-up table based on the near coincident MOD04 water vapor and MOD05 aerosol values, ground elevation, solar zenith and azimuth angles, and sensor viewing geometry.

Evaluated land cover classification schemes

During this first year, we examined two classification schemes, one performed by I2R and one provided by the USDA.

Until our AWIFS atmospheric correction look up table is complete and we are able to rapidly produce surface reflectance values, we began generating AWIFS classification maps based on planetary reflectance. We chose the supervised Maximum Likelihood method in ENVI, with an 80% probability threshold, to classify the AWIFS reflectance maps, although Spectral Angle Mapping was useful for some specific tasks such as picking out clouds to produce a cloud mask. We elected to divide the imagery into four general classes during this project, namely: woody vegetation, non-woody vegetation, bare Earth, and water following Danaher et al. 2002. We examined the reflectance values for these four classes and found them to be reasonable.

When available, we also made use of land cover classifications based on the USDA National Agricultural Statistics Service (NASS) Cropland Data Layer (CDL)

(<http://www.nass.usda.gov/research/Cropland/SARS1a.htm>), shown in Figure 11. In order to use this classification map, we applied a cloud mask, and then grouped its far more detailed classes into the four more general ones we are using. This classification scheme, which is based on 56m AWIFS pixels, also incorporates farm level ground truth and other ancillary data. It is however generated only once per year and can therefore contain errors with respect to the AWIFS data we are working with. For example, fields in the AWIFS image used to generate the USDA CDL may contain a particular crop, which is no longer present in the AWIFS image we are working with due to harvest, clearing, replanting, etc.

Figure 12 compares variation in reflectance as a function of sensor view angle for the four classes generated using the Maximum Likelihood algorithm and with the USDA CDL on AWIFS path 265, row 45, quad D, acquired June 5, 2008. Details on how these plots were generated are discussed in the following section. For this scene and in general, the woody, water and bare Earth comparisons show reasonable agreement between the CDL and supervised Maximum Likelihood derived classes, while the water comparison is not as close. The Maximum Likelihood method seemed to produce better results than the CDL for water. This comparison and others we performed also show that there is, in general, more variation in reflectance using the CDL classification. After consideration, this is likely due to the training pixels we selected and the 80% probability percentage we used when we implemented the Maximum Likelihood method. Our implementation of the Maximum Likelihood method leads to a significant number of unclassified pixels, which were likely natural variations within the coarse classes we selected. We plan to investigate this further in the second year of study. As evidenced by our classification comparisons, meaningful results are possible when using the Maximum Likelihood classification method, which we used whenever CDL classifications were unavailable.

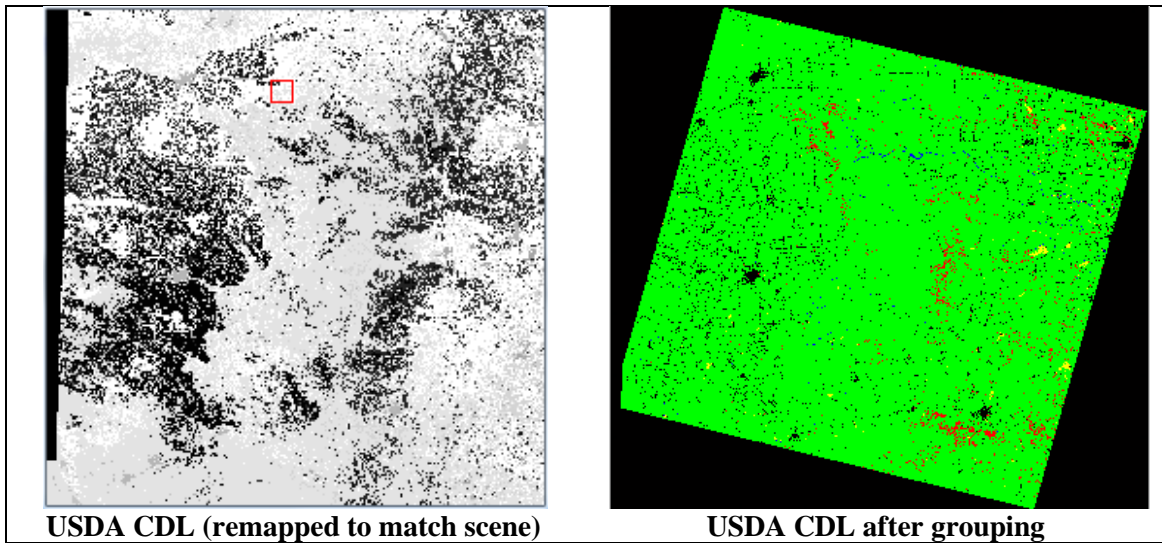


Figure 11. USDA NASS CDL. Path 265, row 45, quad D, acquired April, 18 2008. The original CDL data is composed of integer values identifying almost 200 separate classes, and is here displayed as a gray scale. After class grouping, it is shown with woody vegetation in red, non-woody vegetation in green, bare Earth in blue, and water in yellow.

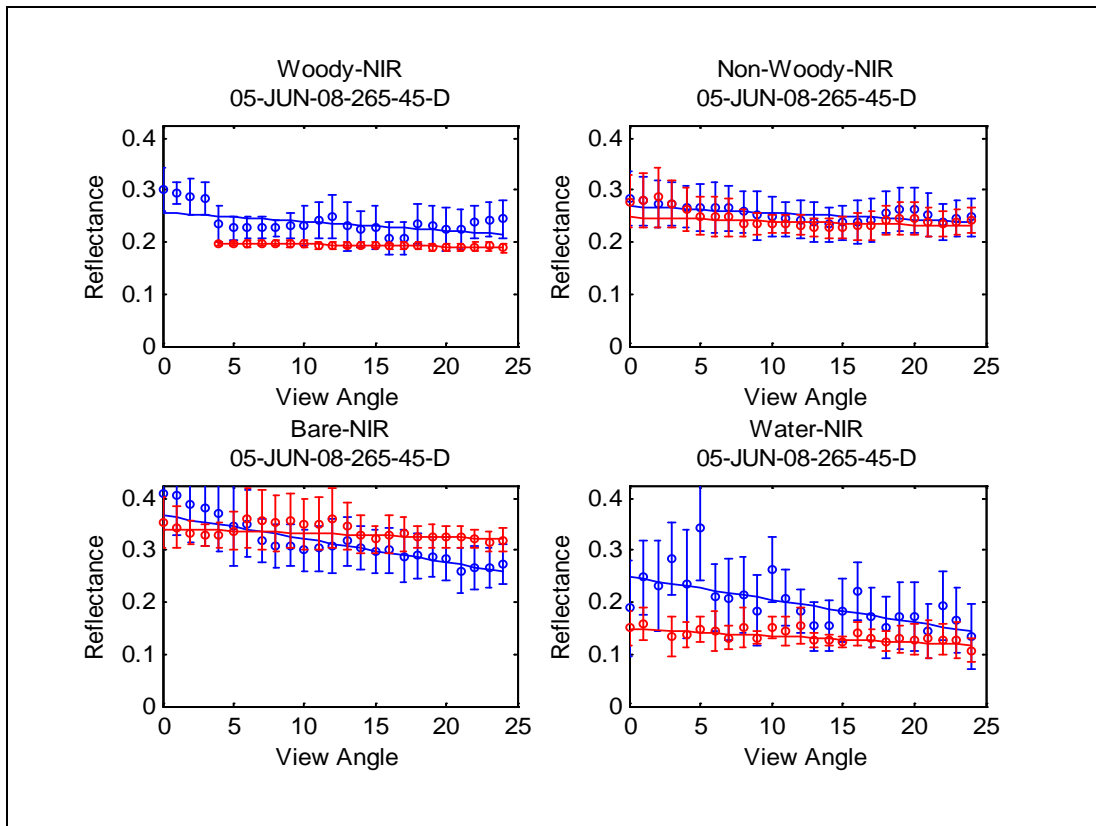


Figure 12. Comparison of the CDL (blue) and Maximum Likelihood (red) classification schemes for AWIFS path 265, row 45, quad D, acquired June 5, 2008

Analyzed change in reflection as a function of view angle

In order to analyze each AWIFS scene to determine BRDF effects, we mapped each pixel to its sensor view angle (sensor zenith) and then plotted the average value of all pixels within a given class for each band at each view angle, from either 0 to ~24 degrees for the AWIFS-B camera module imagery, or 0 to ~24 degrees for the AWIFS-A camera module imagery. To accomplish this, a Matlab script was written which: identified all the pixels of a certain class within a given image; calculated the view angle of each pixel using the row and column coordinates of those pixels and the viewing geometry of the AWIFS system; took a random sample of 10,000 pixels (if the total was larger) at each view angle to limit computation time; and then produced an average reflectance value for that class at that view angle. The slope of such a graph can be related to any BRDF effects present in the image. An example of this assessment, based on a CDL woody vegetation class, is shown in Figure 13. The error bars within the figure represent the variation in reflectance for this broad land cover class.

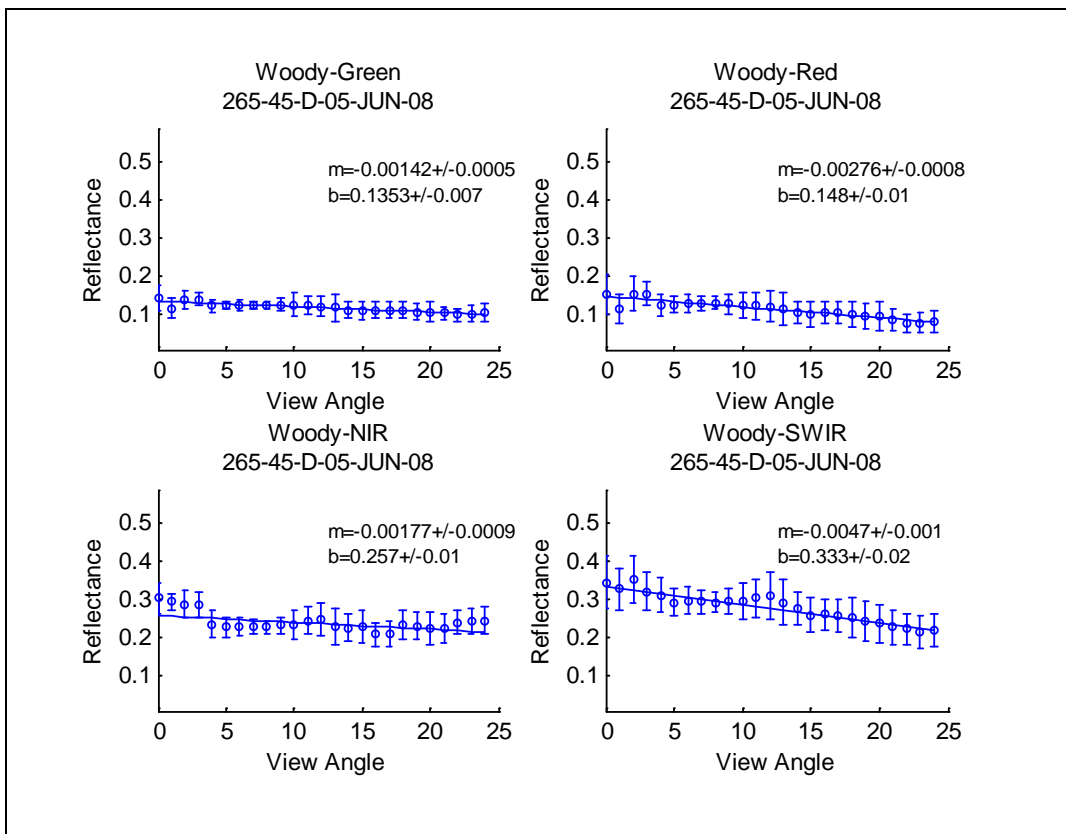


Figure 13. AWIFS reflectance as a function of view angle using the USDA CDL-based classification for the woody vegetation class. Path 265, row 45, quad D, acquired June 5, 2008

In this particular example, imagery was acquired using the AWIFS-B camera module. This camera, which images the eastern side of the overall swath, looks Nadir through ~24 degrees in the forward-scatter direction. The AWIFS-A camera module is arranged in a mirror setting such that it acquires imagery Nadir through ~24 degrees in the back-scatter direction. Since the BRDF induced “hot spot” occurs within the principal plane in the back-scatter direction the forward-scatter results within this figure do not represent the strongest expected BRDF-induced

reflectance differences. All imagery examined during this first year was far away from the principal plane.

This sensor view angle assessment, at a given solar and sensor position, was performed on eleven AWIFS scenes screened for low aerosol optical thickness (AOT) at 550 nm and shown in Table 2. By working with low aerosol optical thickness scenes, we expect TOA planetary reflectance values should be close to surface reflectance values. We expect that the results obtained using planetary reflectance values this first year should be similar to what we anticipate obtaining using surface reflectance values in our second year of study. Also included in the table are mean solar zenith angles, θ_s , sensor zenith angle range, θ_v , mean solar azimuth angles, φ_s , mean sensor azimuth angles, φ_v , and φ , defined as sensor azimuth minus solar azimuth. The assessment was performed with classification maps generated using both the supervised Maximum Likelihood algorithm applied to AWIFS TOA planetary reflectance values and USDA CDL land cover classifications where available. Similar trends as those shown in Figure 13 were observed. Complete results including individual plots and a summary table of slope and y-intercept can be found in Appendix 3.

Table 2. AWIFS Scenes used to Develop Initial BRDF Correction Factors

AWIFS Scene ID	Classification Method	Date Acquired	AOT	θ_s (deg)	θ_v (deg)	Φ_v (deg)	Φ_s (deg)	Φ (deg)
247-36-D	Max. Like (ML)	22-JUN-06	.060	23.4	0 - 24.3	-73.4	149.1	-222.5
255-30-C	Max. Like (ML)	21-JUL-08	.001	34.2	0 - 24.3	104.5	152.8	-48.3
257-30-C	Max. Like (ML)	31-JUL-08	.054	36.4	0 - 24.3	104.5	154.1	-49.6
262-35-A	Max. Like (ML)	01-AUG-08	.001	34.5	0 - 24.3	104.0	151.1	-47.0
263-35-A	Max. Like (ML)	06-AUG-08	.092	35.7	0 - 24.3	104.0	152.1	-48.0
265-45-D	CDL & ML	18-APR-08	.092	26.6	0 - 24.3	-75.1	144.5	-219.6
265-45-D	CDL & ML	05-JUN-08	.090	17.2	0 - 24.3	-75.1	126.3	-201.5
266-45-B	CDL & ML	14-SEP-08	.032	35.8	0 - 24.3	-74.7	157.9	-232.6
266-45-D	CDL & ML	10-JUN-08	.087	17.0	0 - 24.3	-75.1	124.8	-199.9
267-45-B	CDL & ML	19-SEP-08	.110	37.5	0 - 24.3	-74.7	159.6	-234.3
281-48-C	Max. Like (ML)	07-JAN-06	.000	57.3	0 - 24.3	102.5	155.6	-53.1

In general, we found this first assessment to be a reasonable method for verifying the presence of an effect due to view angle but noted it contained relatively large uncertainties due in part to the coarse land cover classes we defined. This method also yields snap shot results for a particular solar geometry and does not systematically address BRDF effects due to variations in solar geometry.

Began developing a statistical BRDF model based on a modified Walthall formulation

To address these noted deficiencies and to develop a more comprehensive assessment of BRDF-induced effects on reflectance, we utilized a modified Walthall statistical BRDF formulation (Walthall et al., 1985, Liang and Strahler 1994, Danaher et al. 2001, Danaher et al. 2002) shown below.

$$\rho(\theta_s, \theta_v, \varphi) = a_0 + a_1 \theta_s + a_2 \theta_v \cos(\varphi) \quad (3)$$

Where: ρ is the BRDF factor, θ_s is the solar zenith, θ_v is the sensor zenith, φ is the relative azimuth, and a_0 , a_1 , and a_2 are constants to be determined. During this first year we developed the framework to determine the values of these constants, tested the framework we put in place and then made some initial estimates.

To test our framework we worked with the eleven low aerosol optical thickness AWiFS scenes shown above in Table 2. For each of these scenes we again utilized the Maximum Likelihood derived classification maps only where CDL values were unavailable and either generated or grouped like classes to generate the four previously discussed land cover classes (woody vegetation, non-woody vegetation, bare Earth and water). Solar azimuth and zenith angles were calculated from the date, time, location, and altitude of each pixel on Earth. Separate assessments were performed for the two AWiFS camera modules. The AWiFS sensor azimuth, which varies minimally within a scene, was considered constant throughout a single scene, while the AWiFS sensor zenith varied from 0 to ~24 degrees across a scene for the AWiFS-A and from 0 to ~24 degrees for the AWiFS-B camera module (east being defined as the positive direction). As can be seen in Table 2, the eleven scenes we worked with had solar zenith angles grouped near four different values: 17, 24, 35 and 57 degrees. More specifically, AWiFS-A data was associated with 2 solar zenith angle groupings (35 and 57 degrees) and AWiFS-B data was associated with 3 solar zenith angle groupings (17, 24 and 35 degrees). To keep the computation time reasonable, and evenly divide the data between solar angle groupings, we limited the data that went into the statistical model by randomly selecting 100,000 points for each class at each sensor view angle and solar zenith angle grouping. We then performed a Least Squares optimization to fit the randomly selected data from the classified land cover maps associated with each AWiFS camera module to the modified Walthall equation. The resulting coefficients are shown in Table 3 (AWiFS-A) and Table 4 (AWiFS-B).

Table 3. Modified Walthall Coefficients for AWiFS-A Camera Module

Reflectance	Band	Class	a0	a1	a2
Planetary	Green	Woody	0.0453	0.0540	-0.0143
Planetary	Red	Woody	0.0068	0.0599	-0.0171
Planetary	NIR	Woody	0.3608	-0.1682	-0.0410
Planetary	SWIR	Woody	0.1296	0.0354	-0.0946
Planetary	Green	Non-Woody	0.0745	0.0454	-0.0007
Planetary	Red	Non-Woody	-0.0083	0.1104	0.0088
Planetary	NIR	Non-Woody	0.5772	-0.3719	-0.0571
Planetary	SWIR	Non-Woody	-0.0708	0.3291	0.0029
Planetary	Green	Bare	0.1134	0.0283	-0.0243
Planetary	Red	Bare	0.1006	0.0313	-0.0395
Planetary	NIR	Bare	0.0968	0.1295	-0.0535
Planetary	SWIR	Bare	0.0639	0.2554	-0.0779
Planetary	Green	Water	0.0626	0.0257	-0.0565
Planetary	Red	Water	0.0442	-0.0026	-0.0449
Planetary	NIR	Water	0.0591	-0.0402	-0.0099
Planetary	SWIR	Water	0.0684	-0.0608	-0.0109

Table 4. Modified Walhall Coefficients for AWIFS-B Camera Module

Reflectance	Band	Class	a0	a1	a2
Planetary	Green	Woody	0.0910	-0.0199	-0.0572
Planetary	Red	Woody	0.1064	-0.0702	0.0002
Planetary	NIR	Woody	0.2003	-0.0408	-0.0893
Planetary	SWIR	Woody	0.2759	-0.1619	0.0507
Planetary	Green	Non-Woody	0.1531	-0.0698	0.0521
Planetary	Red	Non-Woody	0.1910	-0.1430	0.1169
Planetary	NIR	Non-Woody	0.3169	-0.1504	0.0363
Planetary	SWIR	Non-Woody	0.4326	-0.2680	0.2471
Planetary	Green	Bare	0.1854	-0.0721	0.0320
Planetary	Red	Bare	0.2434	-0.1428	0.0661
Planetary	NIR	Bare	0.3393	-0.2087	0.0483
Planetary	SWIR	Bare	0.5395	-0.5000	0.1805
Planetary	Green	Water	0.1907	-0.1579	-0.0542
Planetary	Red	Water	0.2004	-0.2036	-0.0473
Planetary	NIR	Water	0.1582	-0.0747	-0.0740
Planetary	SWIR	Water	0.2056	-0.1734	-0.0169

In order to illustrate the resulting statistical BRDF calculations, BRDF was plotted as a function of sensor view angle θ_v for a typical sensor-solar geometry. Figure 14 shows a set of correction factors for the AWIFS-A camera module where the solar view angle was set to 37 degrees and the sensor-solar azimuth angle difference was set to 108 degrees, while Figure 15 depicts a set of correction factors for the AWIFS-B camera module where the solar view angle was set to 37 degrees and the sensor-solar azimuth angle difference was set to -49 degrees. In general, our early results show reflectance values and trends consistent with that found in the general literature (Danaher et al. 2002).

We then compared our statistical BRDF result, based on eleven scenes, with reflectance values obtained as a function of sensor view angle across a single scene for a specific land cover class as was described in the previous section. These results are shown in Figure 16 for the woody class within an AWIFS-A image, and in Figure 17 for the woody class within an AWIFS-B image. In both cases the statistical BRDF results using a modified Walhall formulation agree well with that determined using a single scene. This result gives confidence that the Least Squares fit to the modified Walhall formulation can reasonably describe the variation in reflectance found within a typical AWIFS scene.

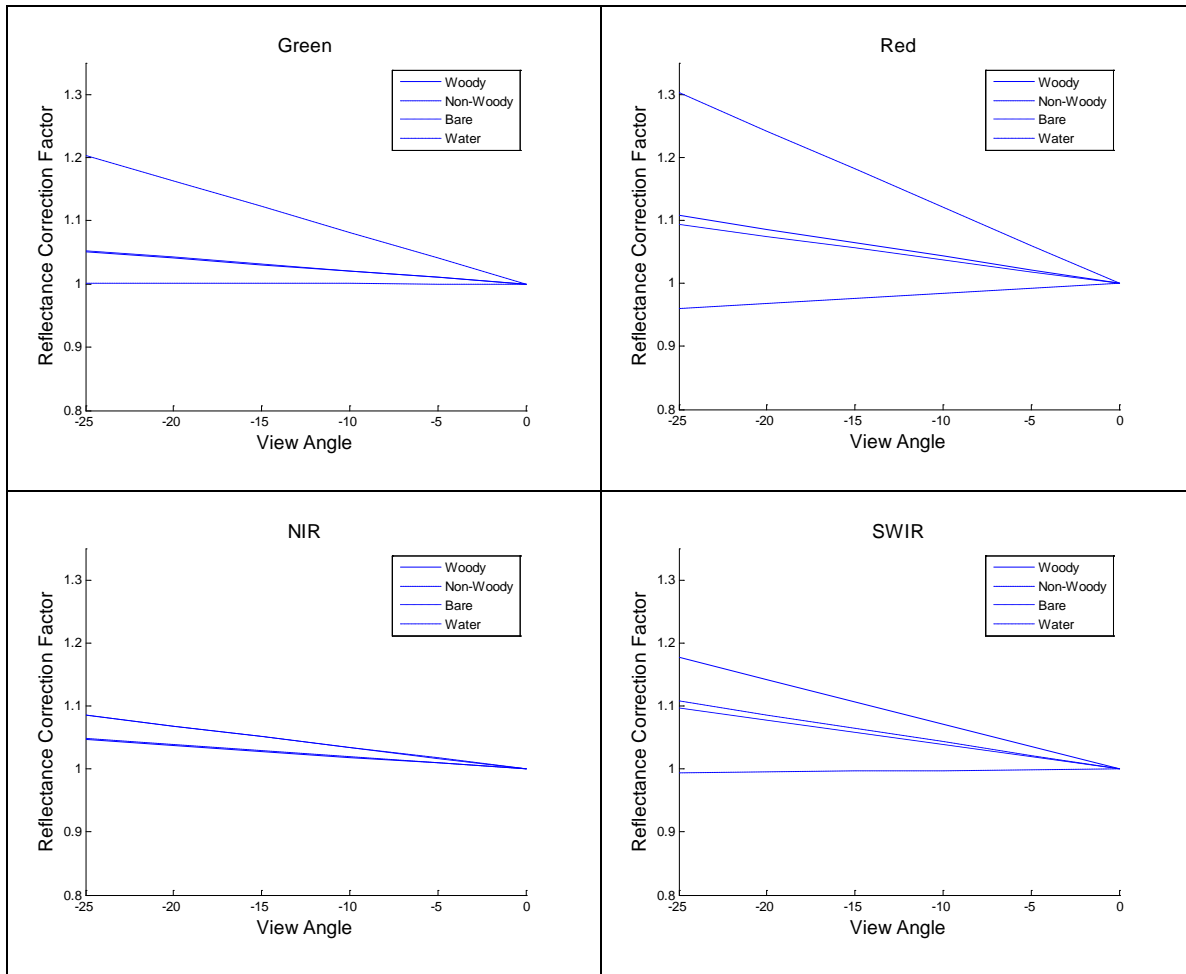


Figure 14. Modified Walthall fit results with $\theta_s = 37$ deg .and $\varphi = 108$ deg for AWIFS-A.

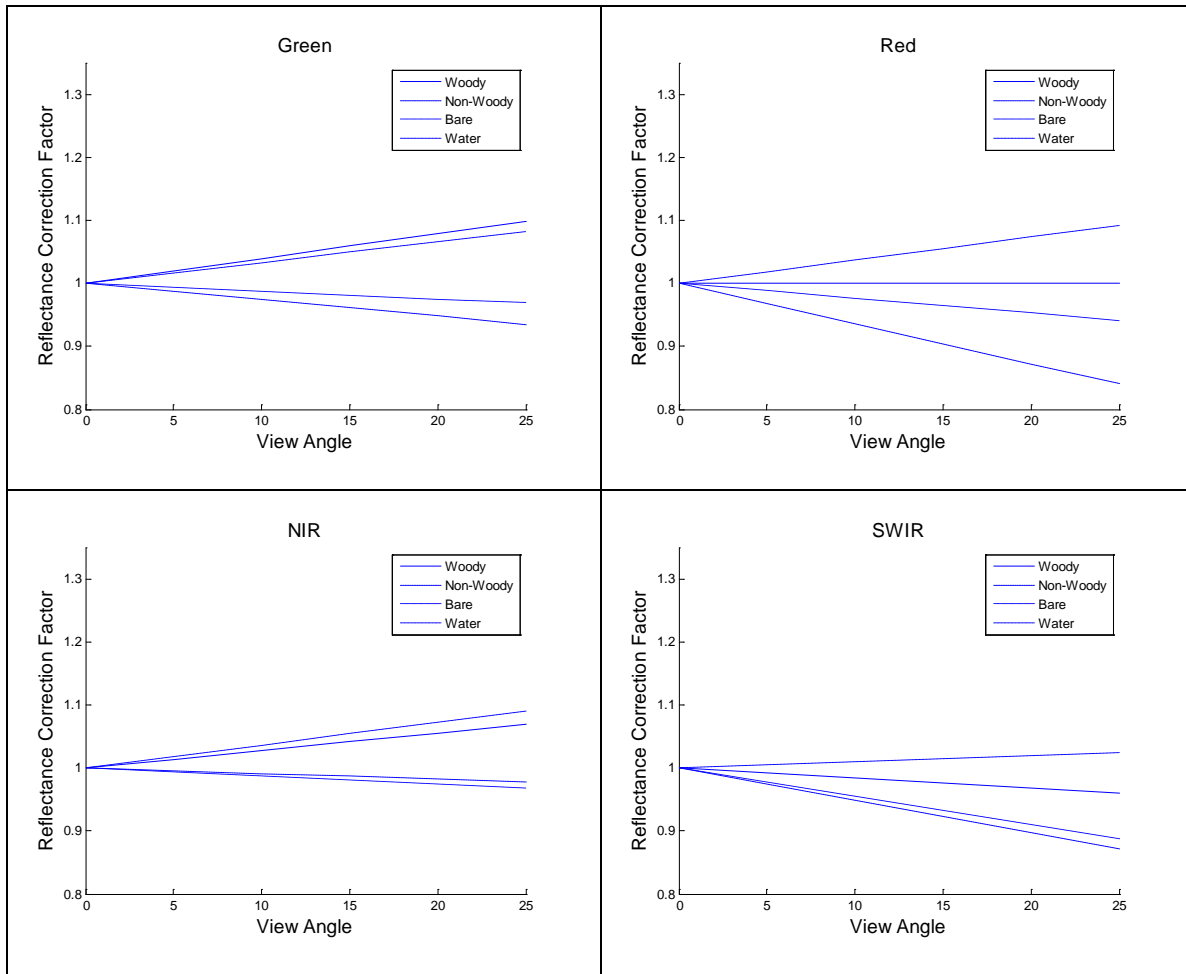


Figure 15. Modified Walthall fit results, with $\theta_s = 37$ deg .and $\varphi = -49$ deg for AWIFS-B.

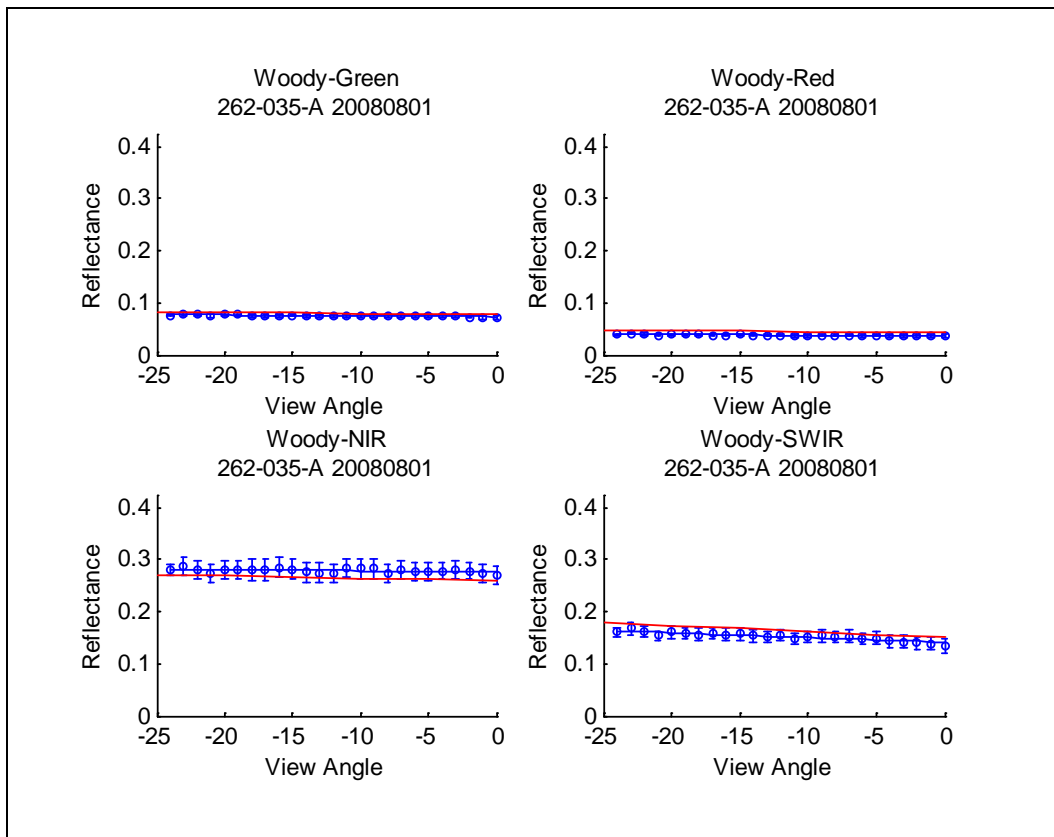


Figure 16. Reflectance variation using a modified Walthall formulation (red) as compared to that determined using a single scene (blue) for AWIFS-A, path 262, row 35, quad A, acquired August 1, 2008.

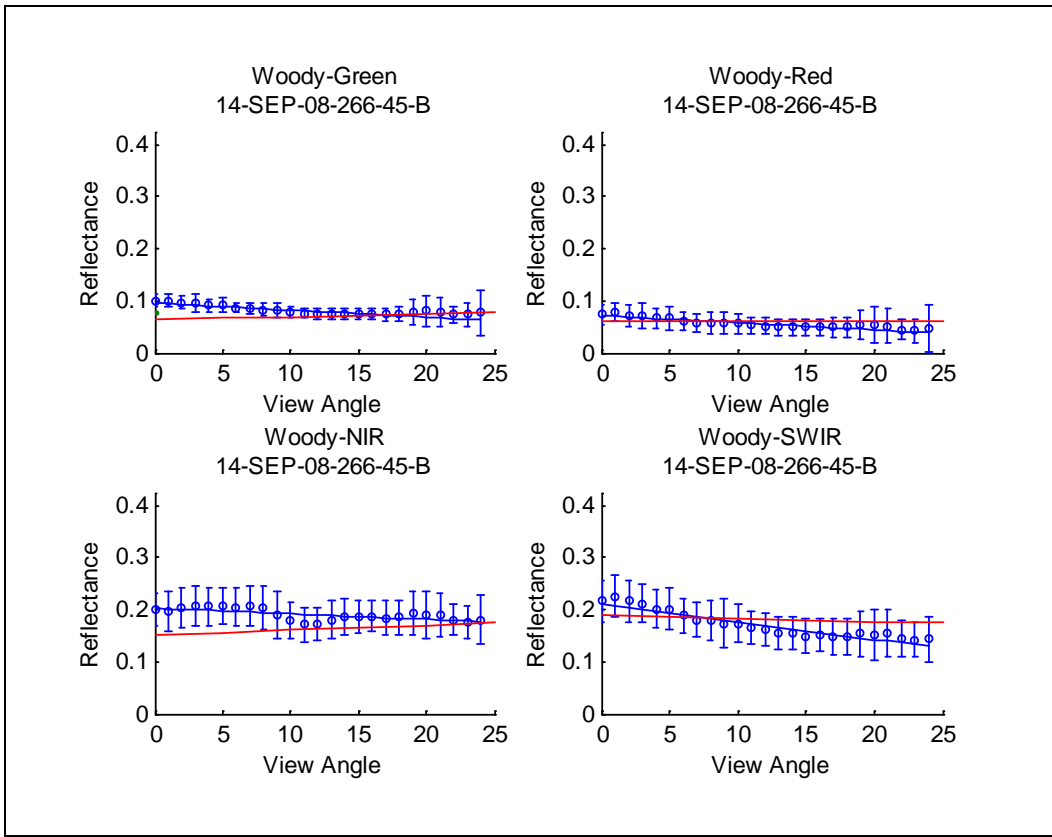


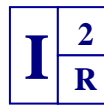
Figure 17. Reflectance variation using a modified Walthall formulation (red) as compared to that determined using a single scene (blue) for AWIFS-B, path 266, row 45, quad B, acquired September 14, 2008.

Year 2 Plan/Objectives

In the second year of this project we will acquire additional AWIFS imagery from the USDA archive. Since the majority of our AWIFS imagery was acquired with the AWIFS-B camera module, emphasis will be on quad A and quad C imagery from the AWIFS-A camera module. As with the AWIFS imagery acquired in the first year, we will screen the imagery using the MODIS MOD04 aerosol optical thickness product to ensure we can atmospherically correct the imagery.

As with the AWIFS data that we have previously acquired, we will generate TOA planetary reflectance maps for all newly acquired imagery. We plan to complete the AWIFS atmospheric look-up table algorithm and associated MODTRAN calculations, and atmospherically correct all of our AWIFS holdings where we have MODIS data.

We plan to generate classification maps using the same broad classes we established in the first year of this study. We will generate classification maps using a supervised Maximum Likelihood approach for both TOA planetary reflectance maps and atmospherically corrected surface reflectance maps. We will evaluate different probability percentages and different training techniques when performing the supervised classifications to improve classification



accuracy. We also plan to download and make use of the USDA CDL classification maps where available.

After generating the classification maps we believe we will have several million classified pixels over a wider range of sensor-solar geometries within each of our broad classes. We then plan to fit this larger data set to the modified Walhall equation discussed above and determine the constants a_0 , a_1 and a_2 . From this we plan to determine the effect of sensor zenith angle, θ_v , solar zenith angle, θ_s , and sensor-solar azimuthal angle difference, φ , on reflectance. We plan to estimate the constants using both surface reflectance and TOA reflectance values within the modified Walhall equation to understand the importance of atmospheric correction, beyond planetary reflectance, when evaluating influences due to solar and viewing geometries. We plan to estimate the constants grouped by land cover determined by grouping classes using the USDA CDL, Maximum Likelihood supervised classification method and others as necessary, to understand the effect the classification scheme has on results. We plan to evaluate other non-linear modified Walhall models that include reciprocity and are capable of modeling additional features such as hot spots in the principal plane. We will include an uncertainty assessment of our results in the second year.

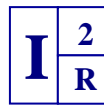
In addition to our final report, we plan to collaborate with Dr. Sam Goward and his research team at the University of Maryland, Mr. Gynesch Chander at the USGS EDC, and Mr. Robert Tetrault at the USDA FAS to publish a peer review paper on the potential of the IRS AWIFS to augment Landsat data in land analysis. An outline of this paper has been developed in conjunction with the other collaborators.

Summary

The Advanced Wide Field Sensor (AWIFS) on-board the IRS-P6 RESOURCESAT-1 satellite is being considered as a candidate to augment, or potentially, in the case of a data gap, partially fill the Landsat archive. While generally similar, the AWIFS remote sensing system differs significantly from Landsat in that it has coarser spatial resolution, reduced number of spectral bands, multiple cameras and larger off-axis viewing geometry, all of which may impact NASA LCLUC research.

In research studies relying on multiple sources of data, such as those requiring very short revisit times, it becomes important to merge results from one remote sensing system with those from another. In this context, our project addresses some of the assessments that would be necessary to augment Landsat data products with data products generated from AWIFS. In a larger sense this project can be cast as one that is developing the framework to perform some of the assessments necessary to augment Landsat data with other remote sensing data sets found and available worldwide. In this way, AWIFS can be seen as a surrogate to other international and commercially available data that may be used to augment Landsat.

The goal of this two year project is to evaluate the effect the larger off-axis viewing geometry has on reflectance products and land cover classifications. This project is in collaboration with related LCLUC Program funded projects at the University of Maryland and the USGS EROS Data Center (EDC). The three funded projects are working closely with the USDA Foreign Agriculture Service (FAS), who currently maintain the largest US government AWIFS archive.



During the first year of this project we defined an overall approach based on a modified Walthall statistical BRDF formulation. We then acquired over 80 AWIFS scenes, mostly from the USDA FAS Satellite Imagery Archive. We have and continue to collaborate with the USGS EDC to support understanding the absolute and relative radiometric performance of the AWIFS system. Continued radiometric performance monitoring is important as it will impact BRDF assessments. We developed methodology to atmospherically correct AWIFS imagery using near-coincident NASA acquired data sets and atmospheric look-up tables. We produced top-of-atmosphere (TOA) planetary reflectance maps and have initiated generating surface reflectance maps based on our new methodology. New methods were required since the AWIFS band combination cannot be used with existing Landsat atmospheric correction algorithms. A subset of these atmospherically corrected products was provided to the UMD. We next generated land cover maps based on TOA planetary reflectance maps and compared several land cover classification schemes, both supervised and unsupervised, for several AWIFS images. We developed methodology to evaluate surface reflectance and TOA reflectance values as a function of solar zenith and azimuth angles, and sensor viewing zenith and azimuth angles for a single land cover class and began developing a statistical BRDF model based on a modified Walthall formulation. In general, our early results show reflectance values and trends consistent with that found in the general literature.

In the second year of our project we plan to acquire additional AWIFS scenes predominantly from the AWIFS-A camera module so that the analyses we have developed can be performed more extensively on imagery from both camera modules. We plan to refine our atmospheric correction algorithm and apply it to all AWIFS imagery and we plan to produce land cover classification maps for each reflectance map we generate. Once we have all of our imagery classified we plan to evaluate reflectance values as a function of solar geometry (azimuth and zenith angle) and sensor viewing geometry (azimuth and zenith angle) using additional modified Walthall model formulations.

We plan to collaborate with our research partners to develop a peer reviewed journal article on the merits of the AWIFS to augment Landsat data.

References

- Berk, A., G.P. Anderson, P.K. Acharya, J.H. Chetwynd, L.S. Bernstein, E.P. Shettle, M.W. Matthew, S.M. Adler-Golden, 1999. MODTRAN4 User's Manual.
- Blonski, S., K. Holekamp, M. Pagnutti, K. Ross, R.E. Ryan, K. Thome, N. Leisso, J. Buchanan, T. Stanley, 2005. AWIFS image product characterization for 2005, October 2005.
- Chander, G., D.L. Helder, J.R. Irons, T.R. Loveland, B.L. Markham, G.L. Stensaas, Evaluation and comparison of the IRS-P6 AWIFS and the Landsat sensors, NASA LCLUC Science Team Meeting, April 20-22, 2010.
- Danaher, T. J., 2002. An empirical BRDF correction for Landsat TM and ETM+ imagery. Proceedings of the 11th Australasian Remote Sensing and Photogrammetry Conference, pp. 966-977.

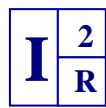
- Danaher, T.J., W. Xiolaing, and N.A. Campbell, 2001. Bi-directional reflectance distribution function approaches to radiometric calibration of Landsat ETM+ imagery. *IEEE 2001 International Geoscience and Remote Sensing Symposium*, pp. 3654-3657.
- Gutman, G., 1998. Monitoring global vegetation using AVHRR. *IEEE International Geoscience and Remote Sensing Symposium*, July, 1998, Seattle, WA, 5:509–2511.
- Gutman, G., D. Tarpley, A. Ignatov, and S. Olson, 1995. The enhanced NOAA global land dataset from the Advanced Very High Resolution Radiometer. *Bulletin of the American Meteorological Society* 76(7):1141–1156.
- Liang, S. and A.H. Strahler, 1994. Retrieval of surface BRDF from multiangle remotely sensed data. *Remote Sensing of Environment*, 50: 18-30.
- Los, S.O., P.R.J. North, W.M.F. Grey, and M.J. Barnsley, 2005. A method to convert AVHRR normalized difference vegetation index time series to a standard viewing and illumination geometry. *Remote Sensing of Environment*, 99: 400–411.
- Pagnutti, M, K. Holekamp, R.E. Ryan, R.D. Vaughan, Jr., J.A. Russell, D. Prados, and T. Stanley, 2005. Atmospheric correction of high spatial resolution commercial satellite imagery products using MODIS atmospheric products., *Third International Workshop on the Analysis of Multi-Temporal Remote Sensing Images*, Roger L. King and Nicholas H. Younan, eds. Beau Rivage Resort and Casino, Biloxi, MS, May 16–18, 2005. New York City: IEEE, pp. 115–119.
- Tanre, D. M. Herman, P. Deschamps, and A. Leffe, 1979. Atmospheric modeling for space measurements of ground reflectances, including bidirectional properties. *Applied Optics*, 18: 3587-3594.
- Thuillier, G, M. Herse, D. Labs, T. Foujols, W. Peetersmans, D. Gillotay, P.C. Simon, H. Mandel, 2003. The solar spectral irradiance from 200 to 2400 nm as measured by the solspec spectrometer from the atlas and eureka missions. *Solar Physics*, 214: 1-22.
- Walshall, G. L., Norman, J. M., Welles, J. M., Campbell, G. and Blad, B. L. 1985. Simple equation to approximate the bi-directional reflectance from vegetative canopies and bare soil surfaces. *Applied Optics*, 24: 383-387.

Appendices

Appendix 1. List of Acquired AWIFS scenes

Path	Row	Quad	Date
247	36	D	6/22/2006
254	40	A	8/28/2009
254	40	B	8/28/2009
254	40	C	8/28/2009
254	40	D	8/28/2009
255	30	C	7/21/2008
257	30	C	7/31/2008
257	47	A	6/29/2005
257	47	B	6/29/2005
257	47	C	6/29/2005
257	47	D	6/29/2005
261	40	D	4/22/2008
262	35	A	8/1/2008
262	40	B	9/18/2008
262	40	D	4/27/2008
263	35	A	8/6/2008
263	40	B	9/23/2008
263	45	B	9/23/2008
263	45	B	4/8/2008
263	45	D	6/19/2008
264	40	D	4/13/2008
264	45	B	4/13/2008
264	45	B	9/28/2008
264	45	D	4/13/2008
264	45	D	6/24/2008
265	40	D	4/18/2008
265	45	B	4/18/2008
265	45	D	6/5/2008
265	45	D	4/18/2008
266	45	B	9/14/2008
266	45	D	6/10/2008
267	40	B	9/19/2008
267	45	B	9/19/2008
267	45	D	6/15/2008

Path	Row	Quad	Date
268	40	A	8/2/2009
268	40	B	9/24/2008
268	40	B	8/2/2009
268	40	C	8/2/2009
268	40	D	8/2/2009
268	45	D	6/20/2008
269	45	B	10/23/2008
269	45	B	4/14/2008
269	45	B	6/25/2008
269	45	D	10/23/2008
270	45	B	4/19/2008
270	45	B	10/28/2008
270	45	B	6/30/2008
270	45	D	10/28/2008
271	39	C	9/26/2006
273	40	A	7/15/2008
273	40	C	7/15/2008
274	40	B	4/15/2008
274	39	C	7/31/2006
274	40	C	7/20/2008
274	45	A	7/20/2008
274	45	B	9/30/2008
274	45	D	4/15/2008
275	40	B	7/1/2008
275	40	B	4/20/2008
275	40	D	7/1/2008
275	40	D	10/5/2008
275	45	B	10/5/2008
275	45	D	4/20/2008
275	45	D	7/1/2008
275	47	D	1/25/2006
276	40	B	7/6/2008
276	40	D	7/6/2008
276	40	D	10/10/2008

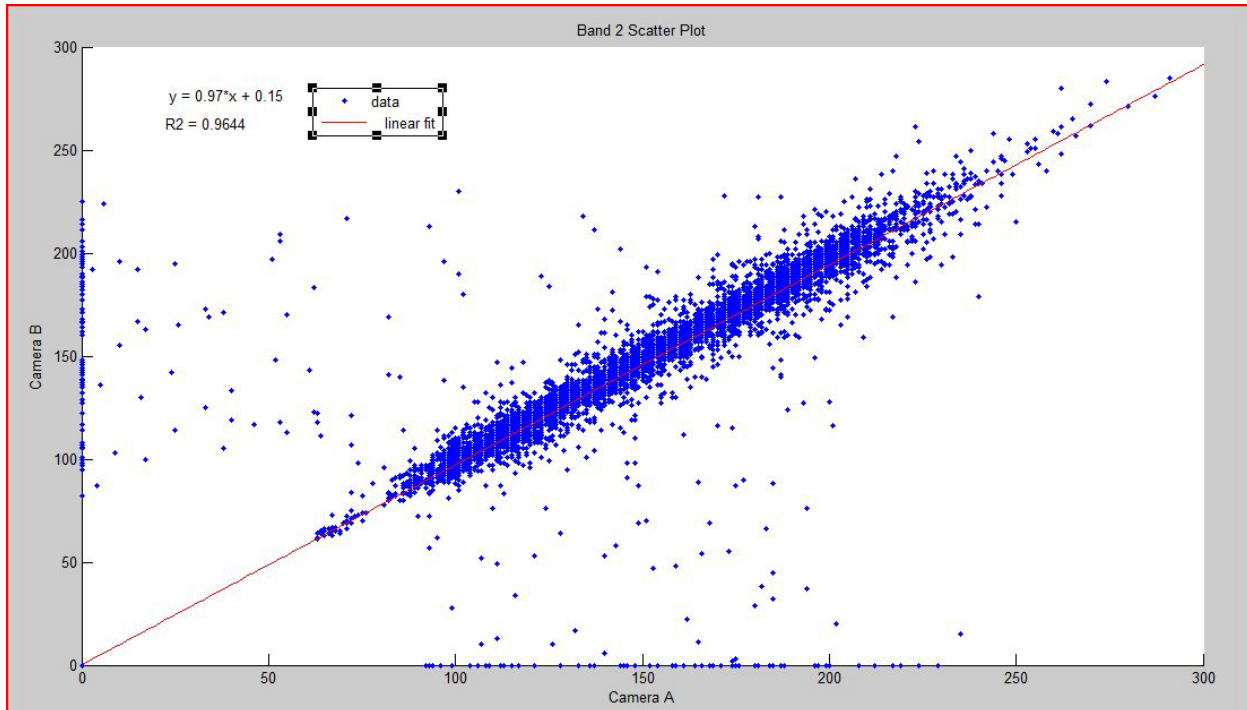


Path	Row	Quad	Date
276	45	B	10/10/2008
276	45	D	4/25/2008
276	45	D	7/6/2008
276	47	D	3/24/2005
277	45	D	4/30/2008
278	45	A	7/16/2008
278	47	D	4/27/2005
279	40	B	4/16/2008
279	45	A	7/21/2008
279	45	B	4/16/2008
280	40	B	4/21/2008
280	45	B	4/21/2008
280	49	C	3/15/2006
281	48	C	1/7/2006
328	93	C	12/23/2007
328	93	C	3/4/2008

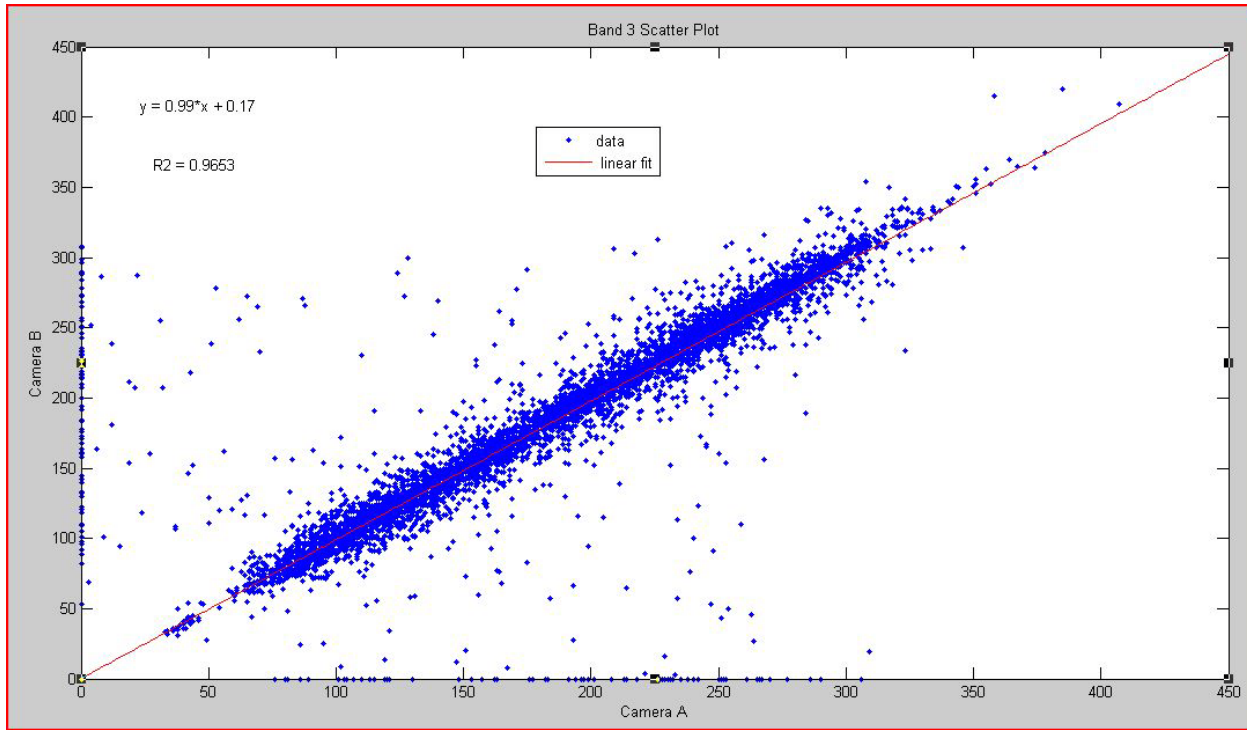
Appendix 2. Relative Radiometry Results

AWiFS Scene	Quads Compared	Method	Band	Slope	Y-intercept	R ²
257/47 June 29, 2005	A-B	Pixel-to-pixel	2	0.97	0.15	0.96
			3	0.99	0.17	0.97
			4	0.98	0.27	0.97
			5	0.98	0.44	0.96
	C-D	Pixel-to-pixel	2	0.98	0.10	0.99
			3	0.99	0.13	0.99
			4	0.98	0.16	0.99
			5	0.99	0.31	0.99
254/40 Aug 28, 2009	A-B	Pixel-to-pixel	2	0.96	6.2	0.94
			3	1.00	-5.2	0.96
			4	1.00	2.3	0.92
			5	0.91	26	0.75
	C-D	Pixel-to-pixel	2	0.96	5.6	0.97
			3	0.99	-4.7	0.99
			4	1.00	2.5	0.95
			5	1.00	1.6	0.94
268/40 Aug 2, 2009	A-B	Pixel-to-pixel	2	0.98	3.2	0.89
			3	1.00	-5.8	0.89
			4	1.00	-4.7	0.92
			5	0.73	65	0.47
	C-D	Pixel-to-pixel	2	0.98	3.9	0.91
			3	1.00	-5.7	0.96
			4	1.00	3.6	0.90
			5	0.91	27	0.74
	A-B	50 pixel avg.	2	0.97	4.7	0.91
			3	0.98	-4.2	0.91
			4	0.99	8.5	0.96
			5	0.98	5.2	0.89

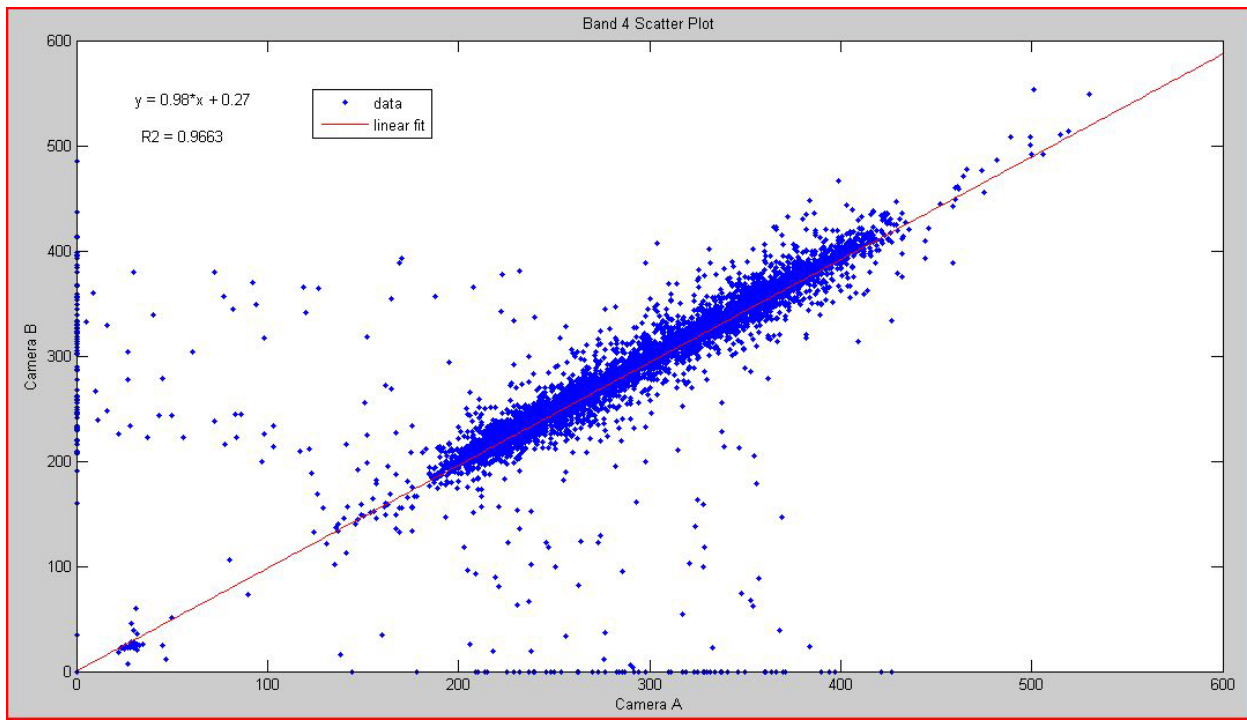
AWiFS Path/Row 257-47 - Acquired June 29, 2005
Pixel-to-Pixel Comparison



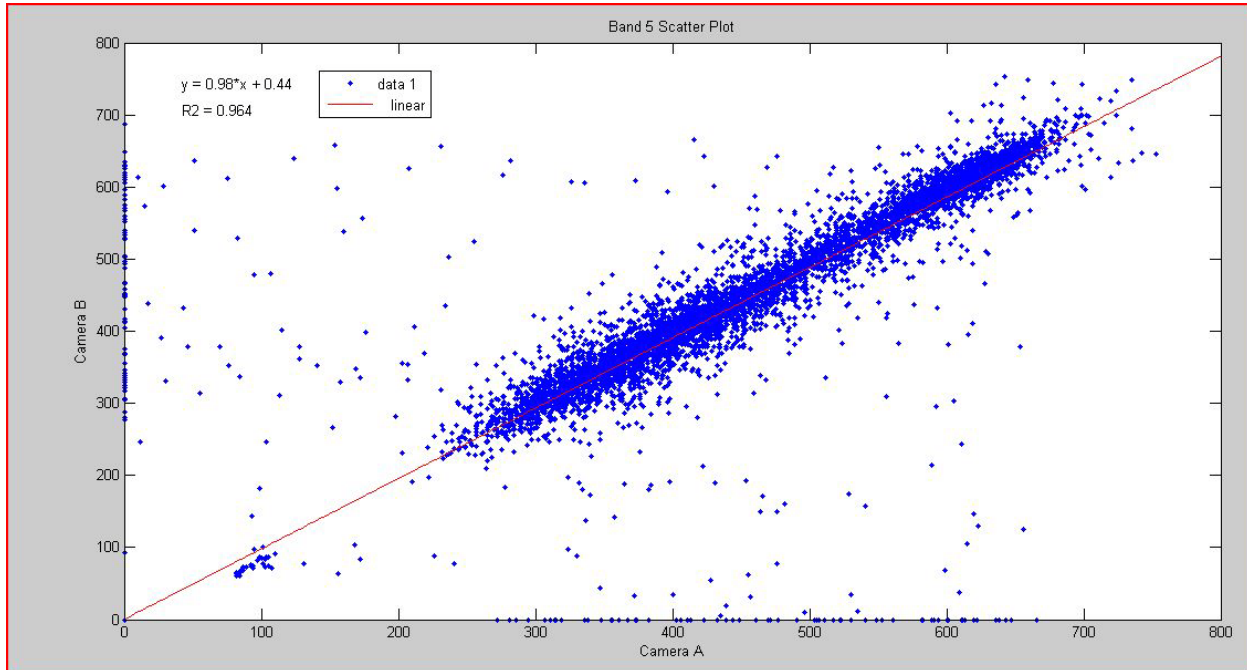
AWiFS Band 2 Quad A vs. Quad B



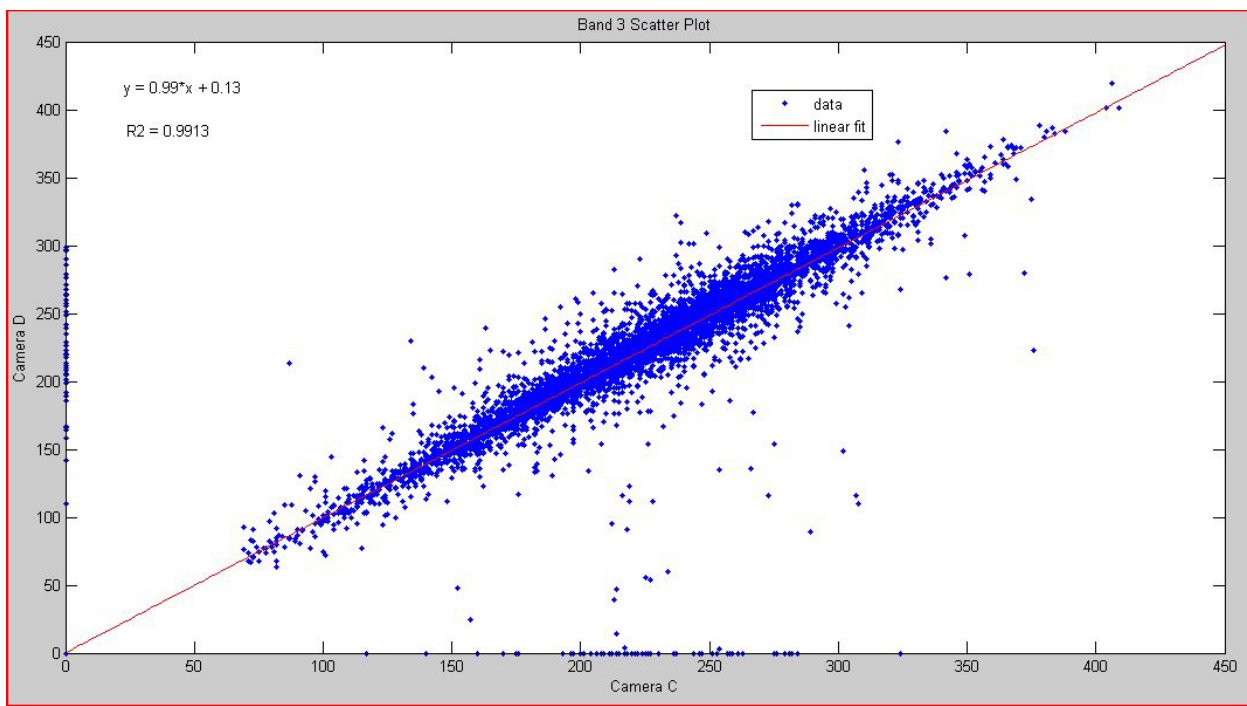
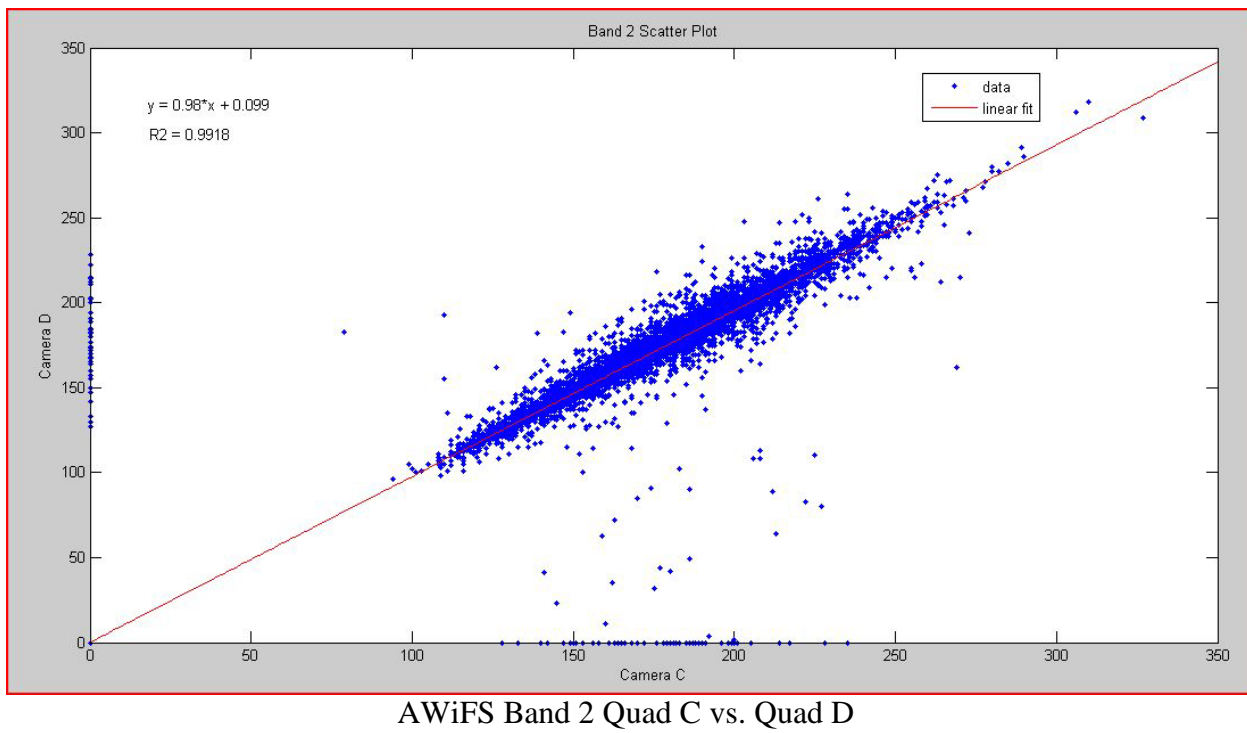
AWiFS Band 3 Quad A vs. Quad B

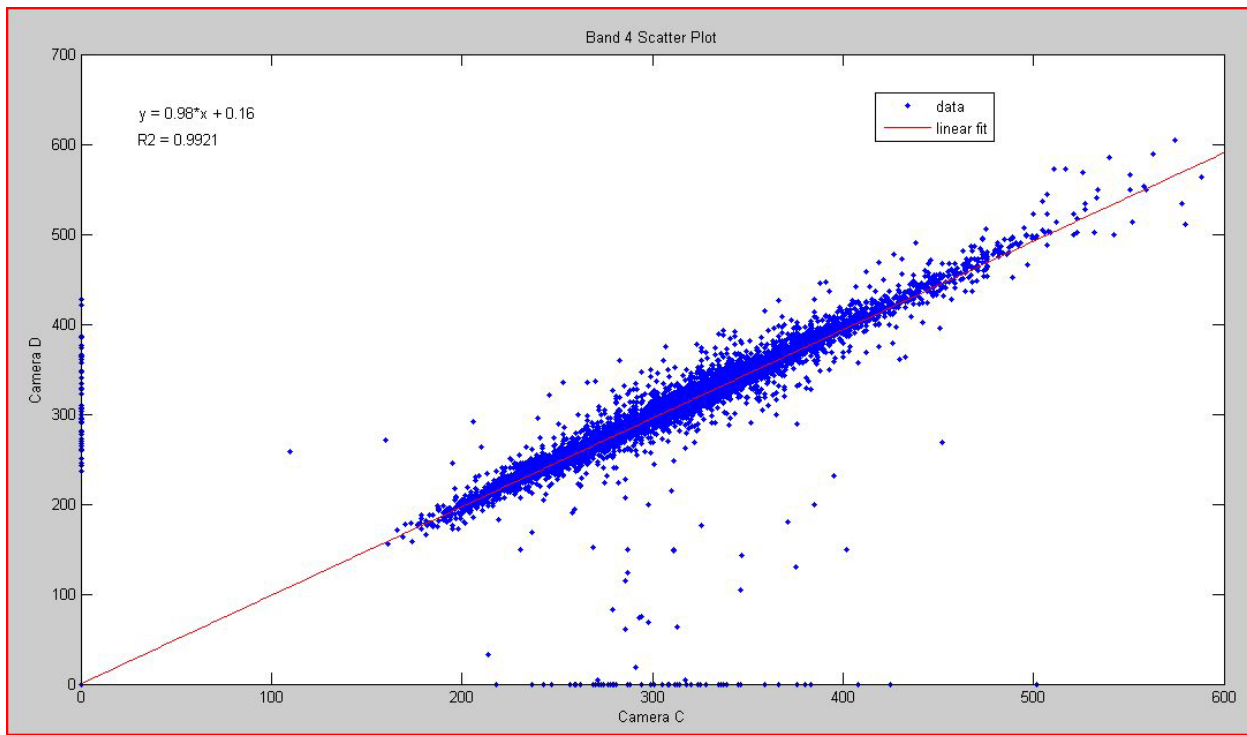


AWiFS Band 4 Quad A vs. Quad B

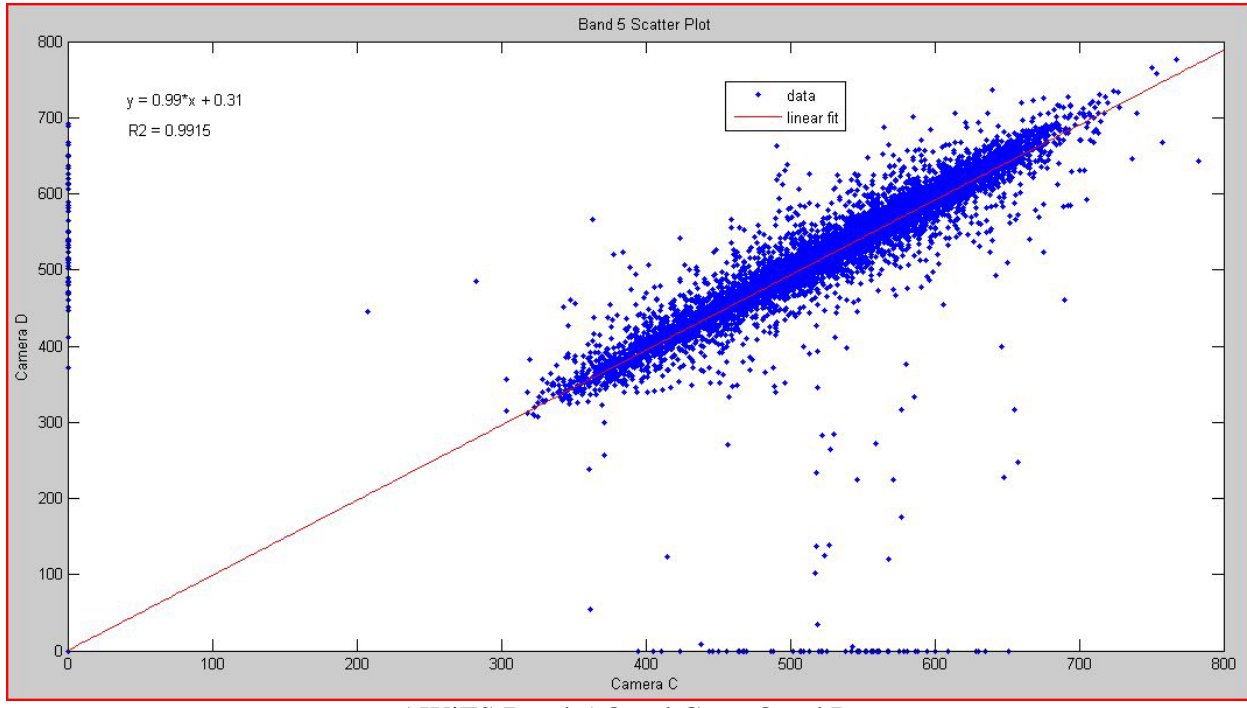


AWiFS Band 5 Quad A vs. Quad B



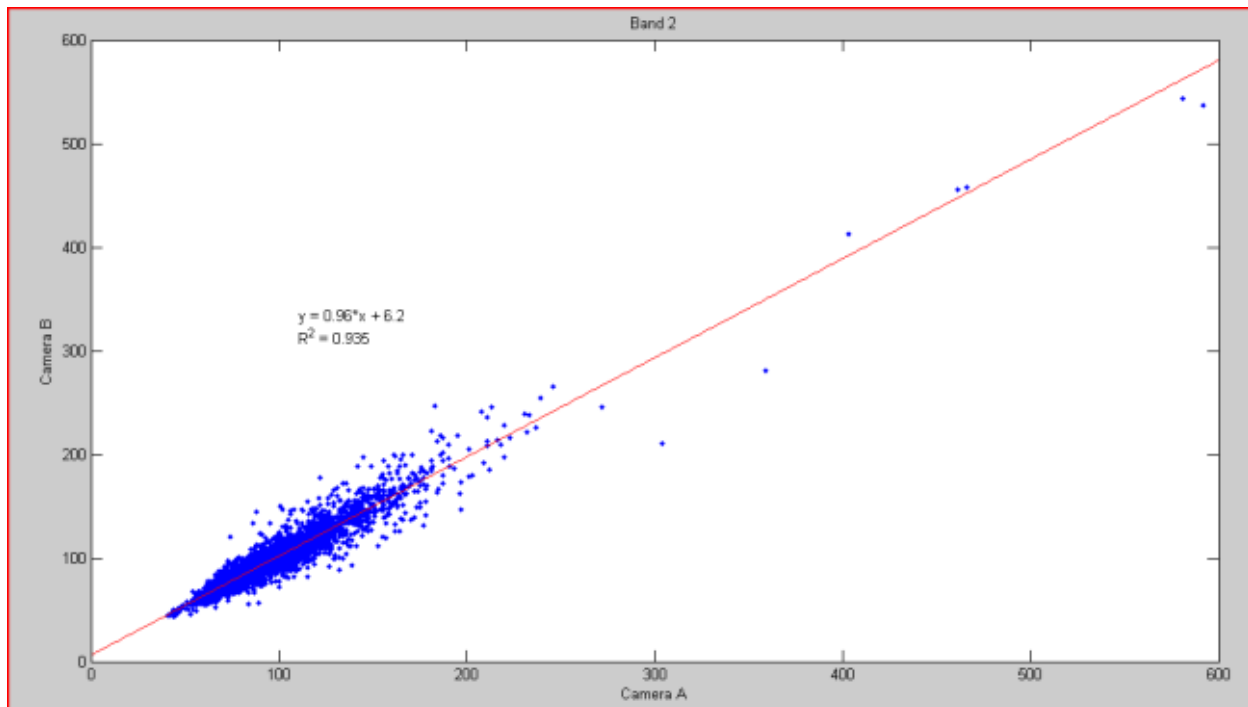


AWiFS Band 4 Quad C vs. Quad D

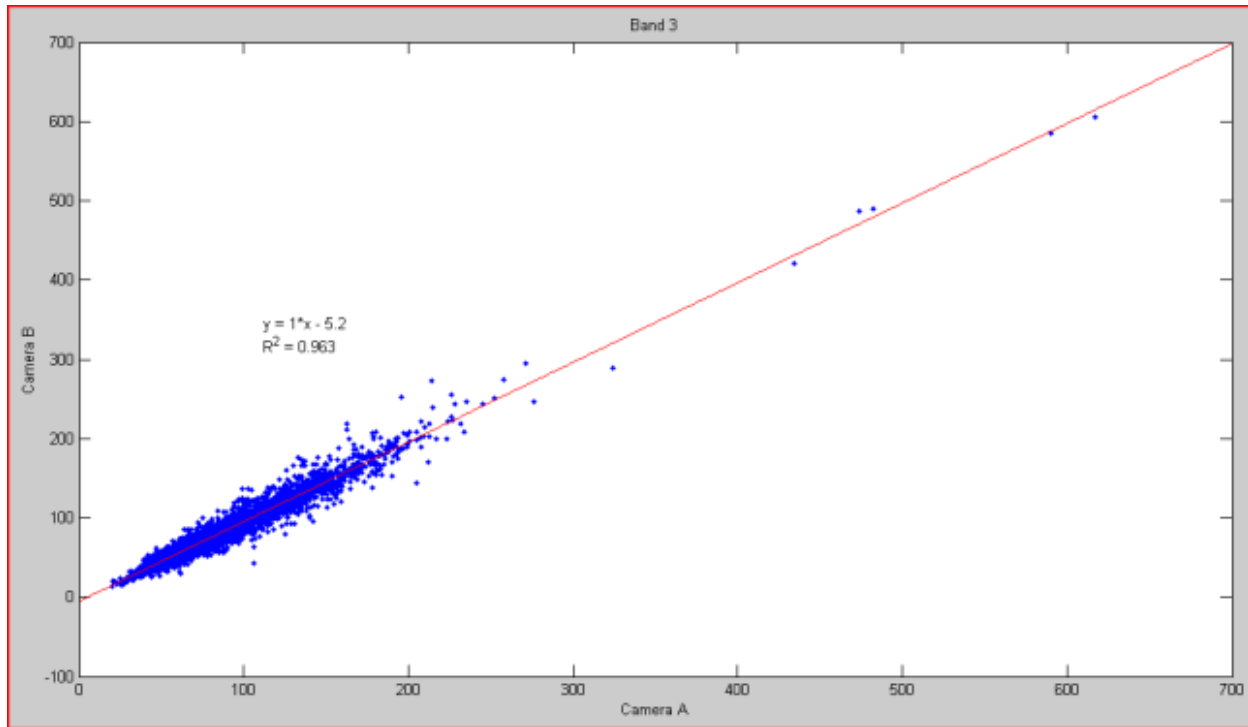


AWiFS Band 5 Quad C vs. Quad D

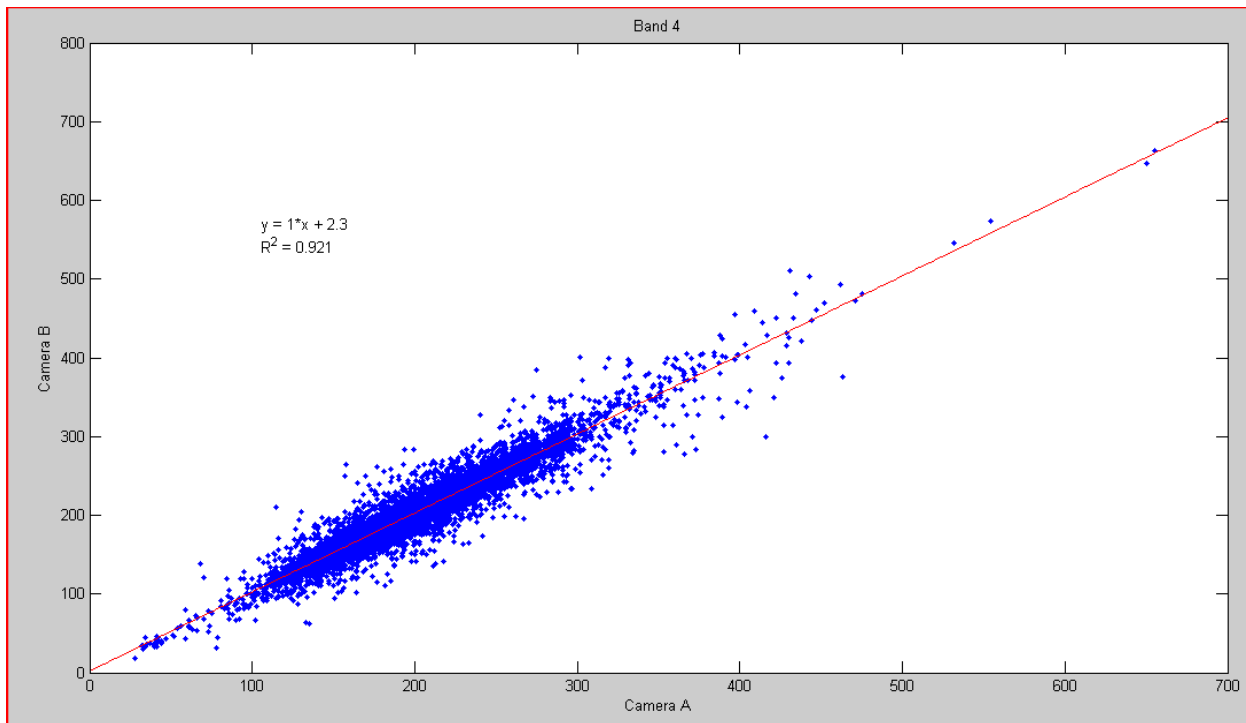
AWiFS Path/Row 254-40 - Acquired August 28, 2009
 Pixel-to-Pixel Comparison



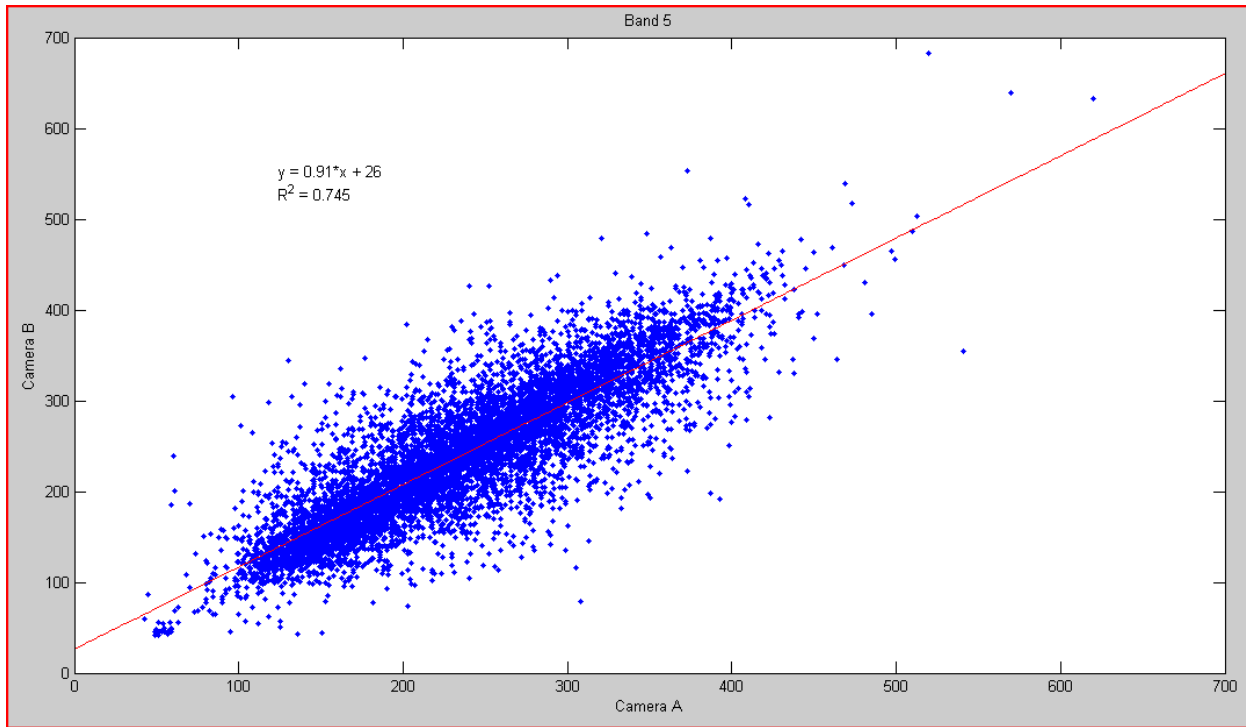
AWiFS Band 2 Quad A vs. Quad B



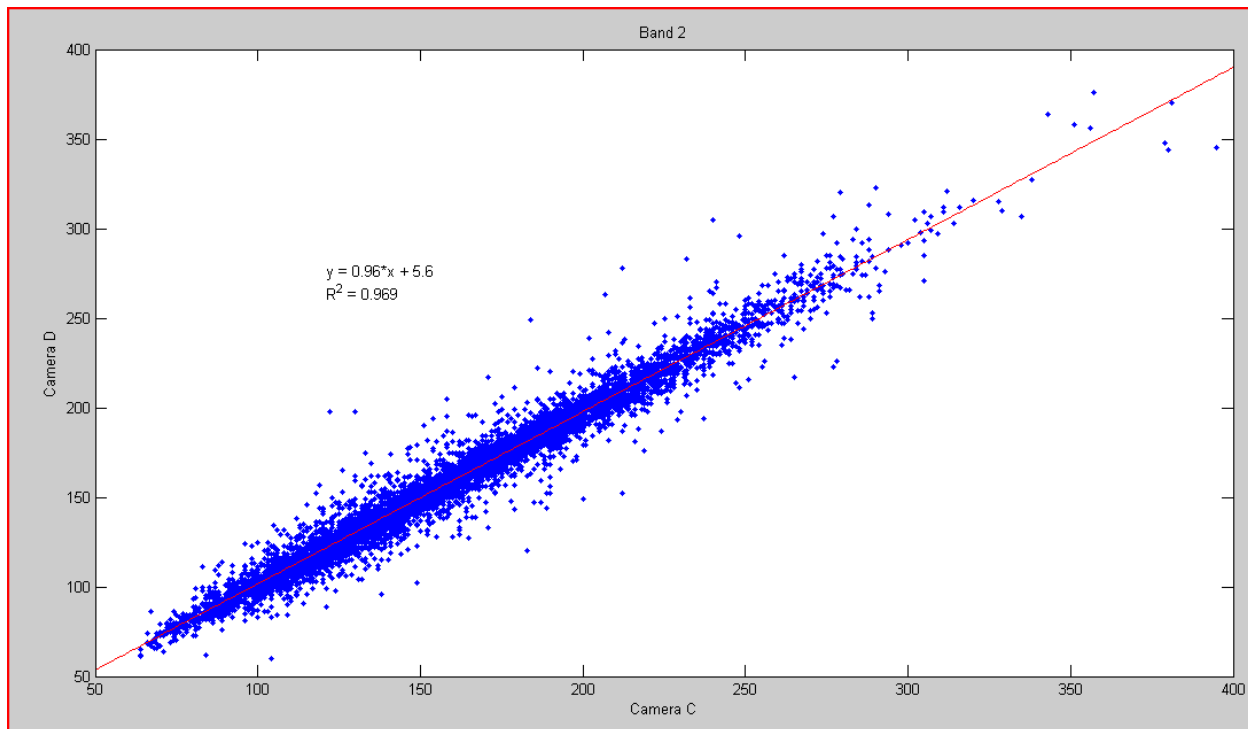
AWiFS Band 3 Quad A vs. Quad B



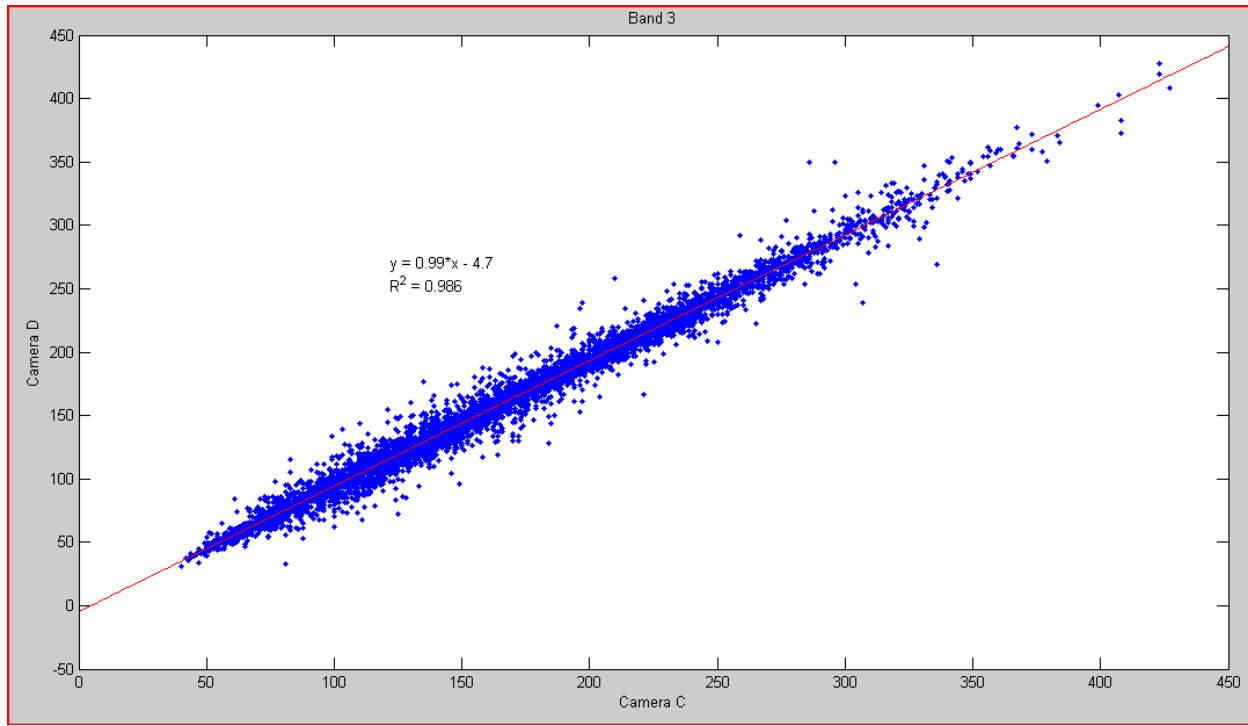
AWiFS Band 4 Quad A vs. Quad B



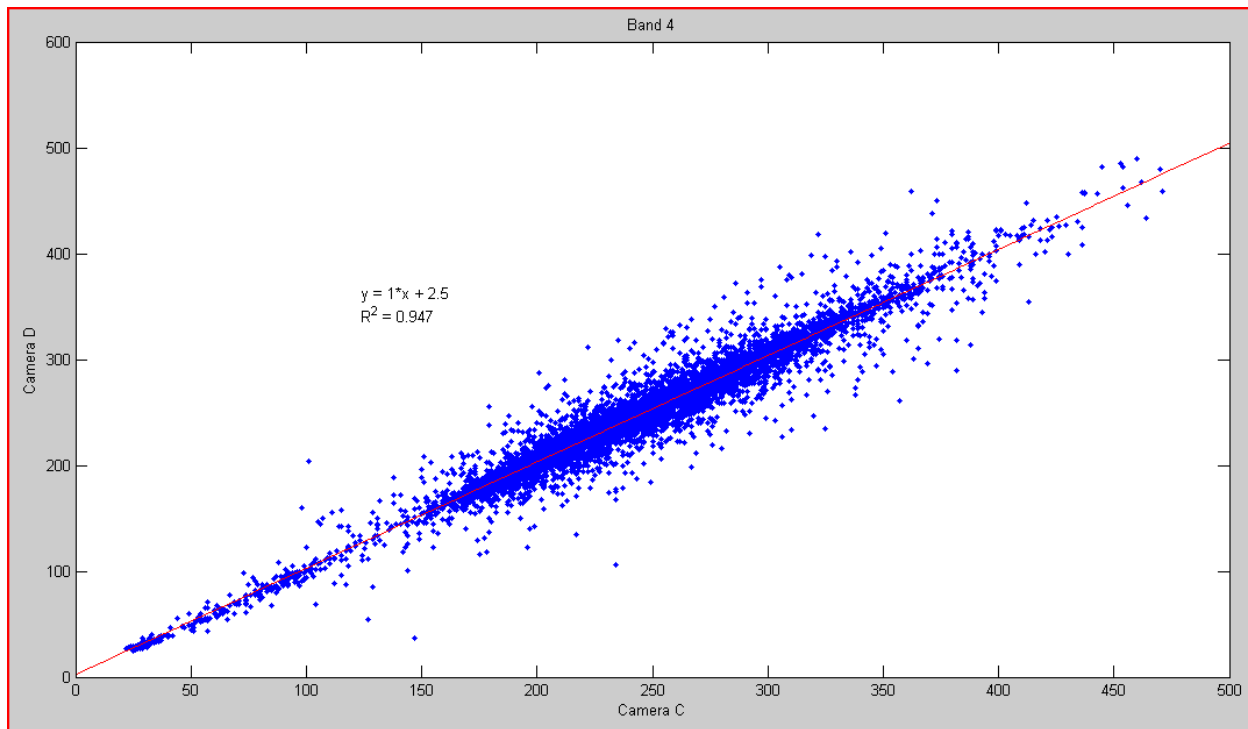
AWiFS Band 5 Quad A vs. Quad B



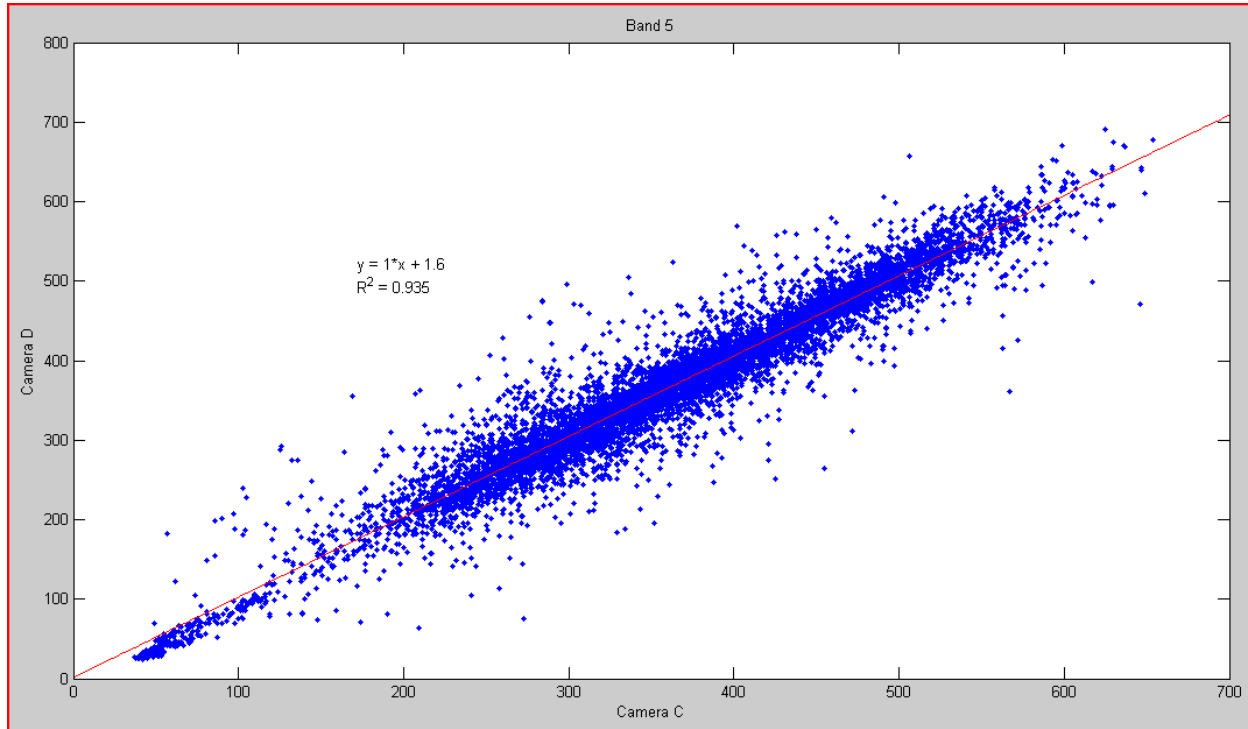
AWiFS Band 2 Quad C vs. Quad D



AWiFS Band 3 Quad C vs. Quad D

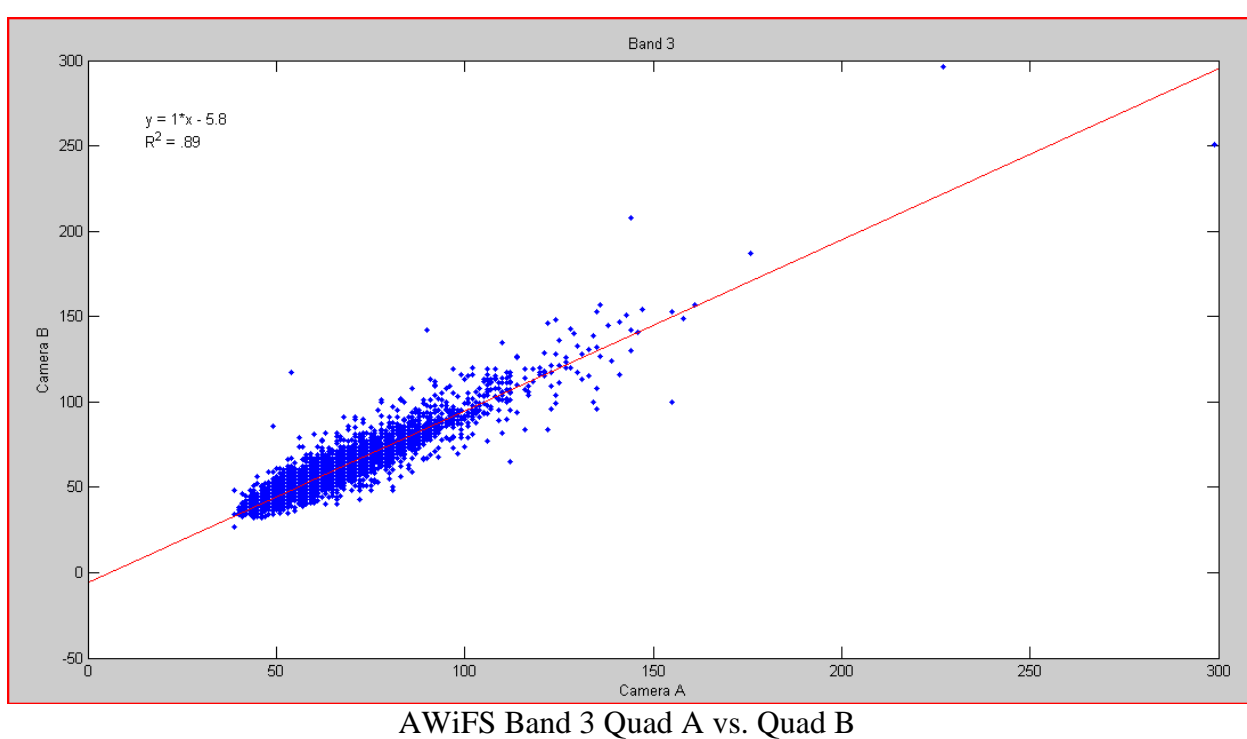
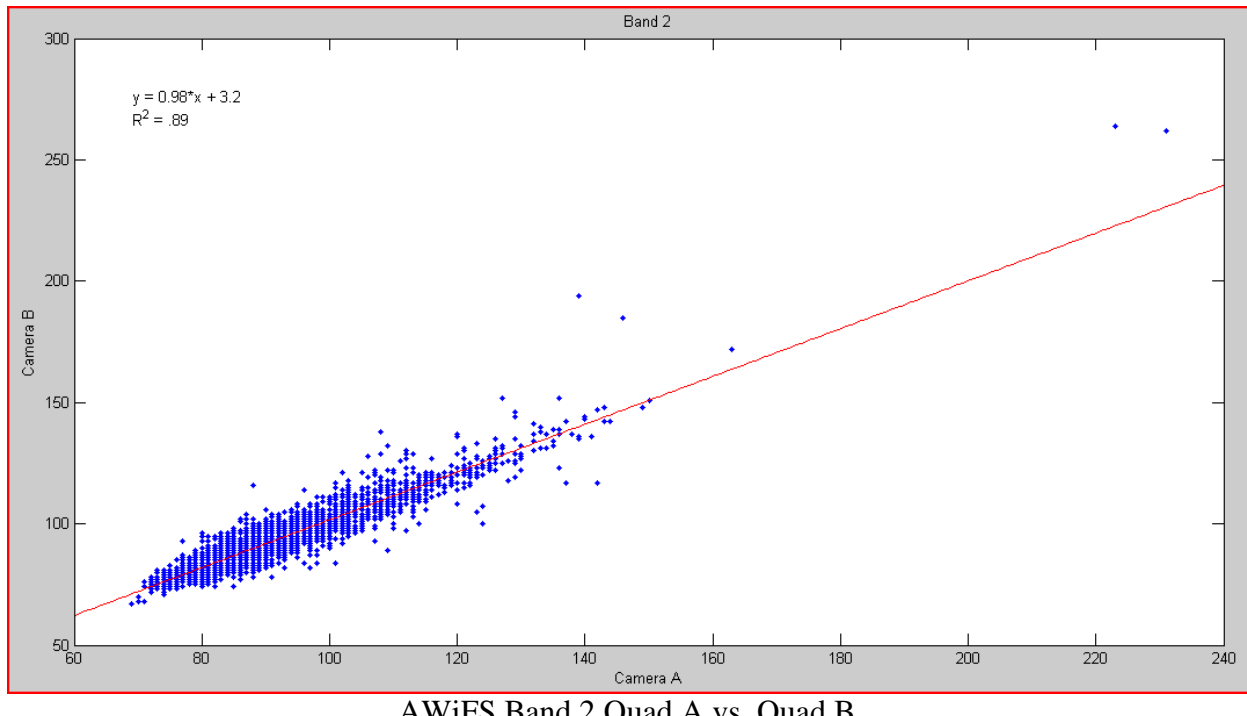


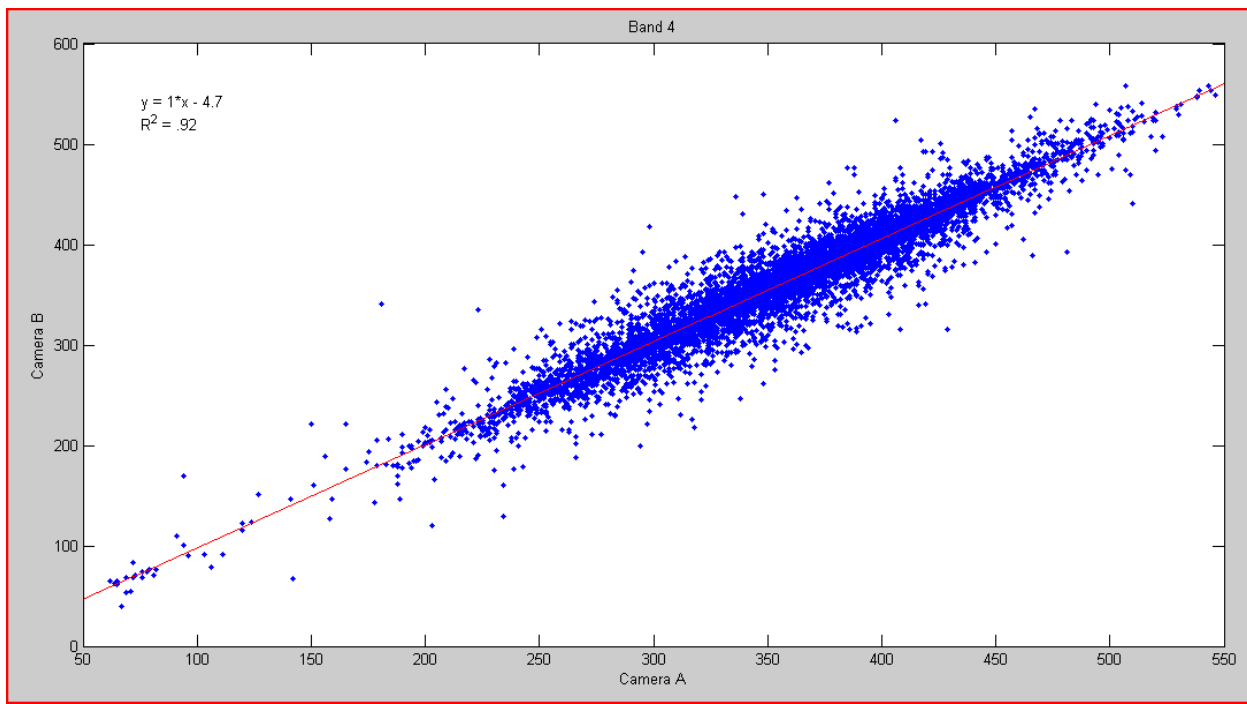
AWiFS Band 4 Quad C vs. Quad D



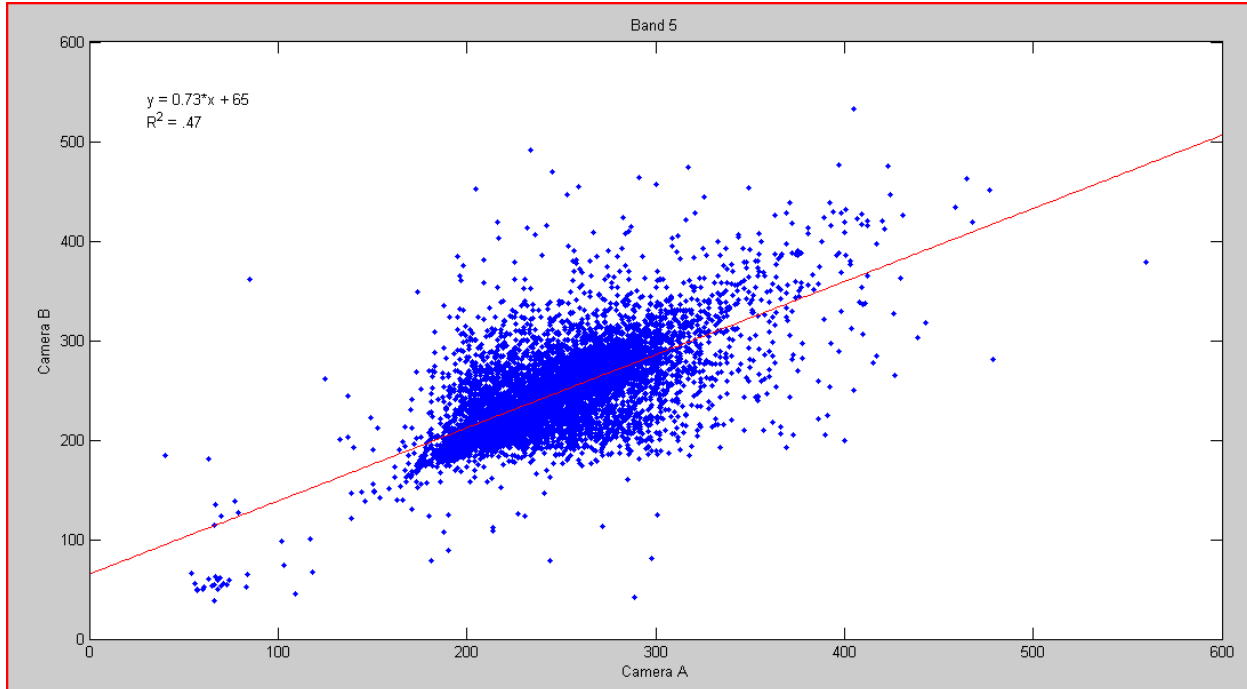
AWiFS Band 5 Quad C vs. Quad D

AWiFS Path/Row 268-40 - Acquired August 2, 2009
 Pixel-to-Pixel Comparison

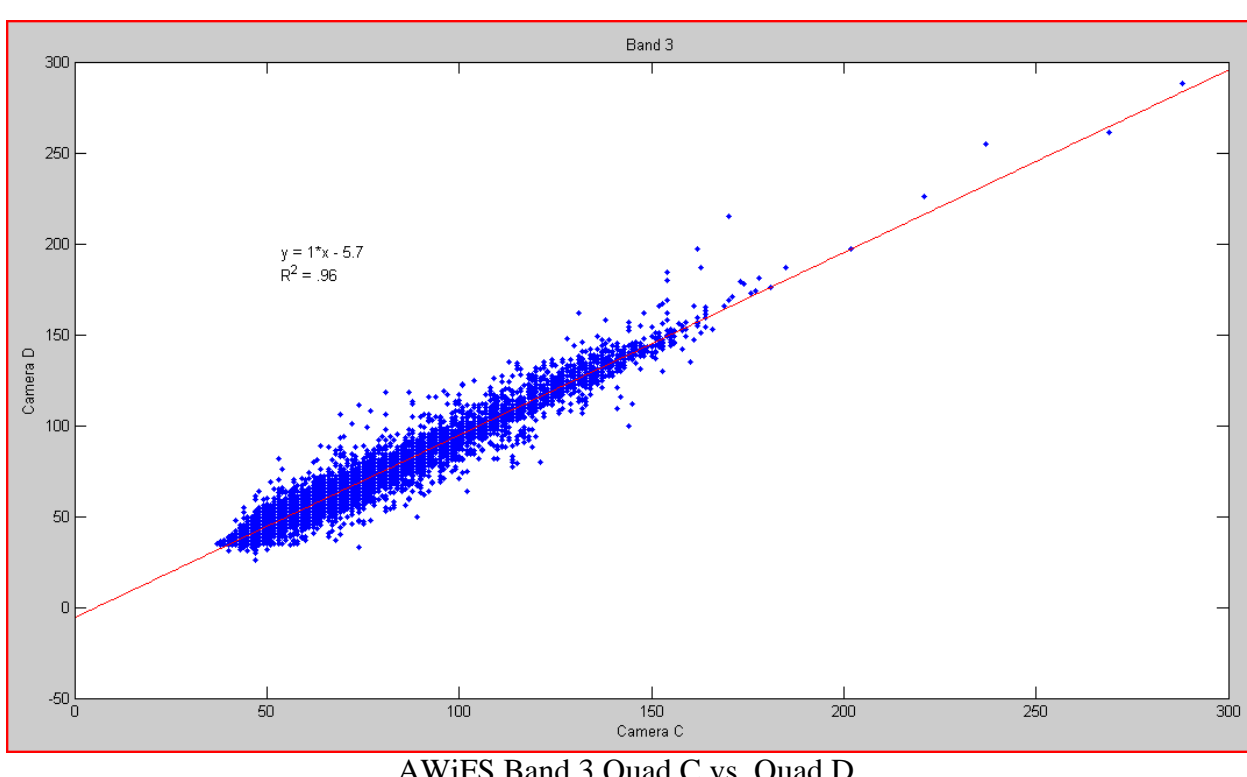
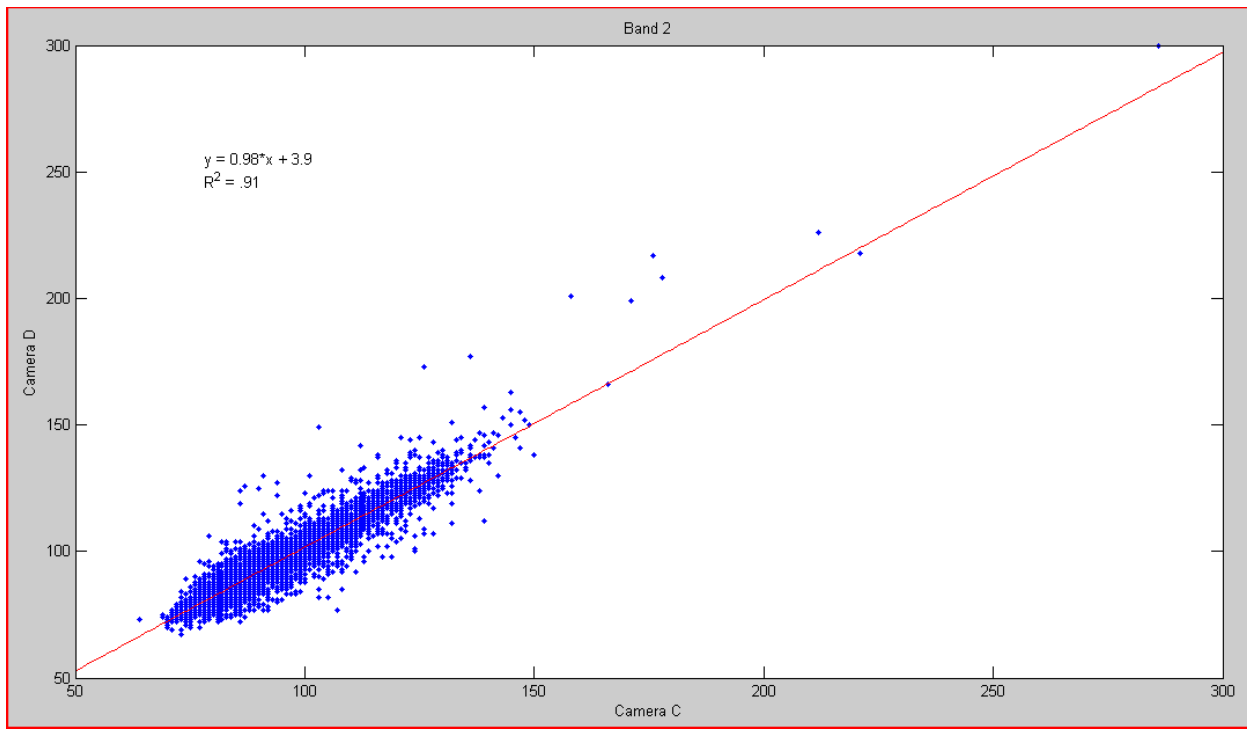


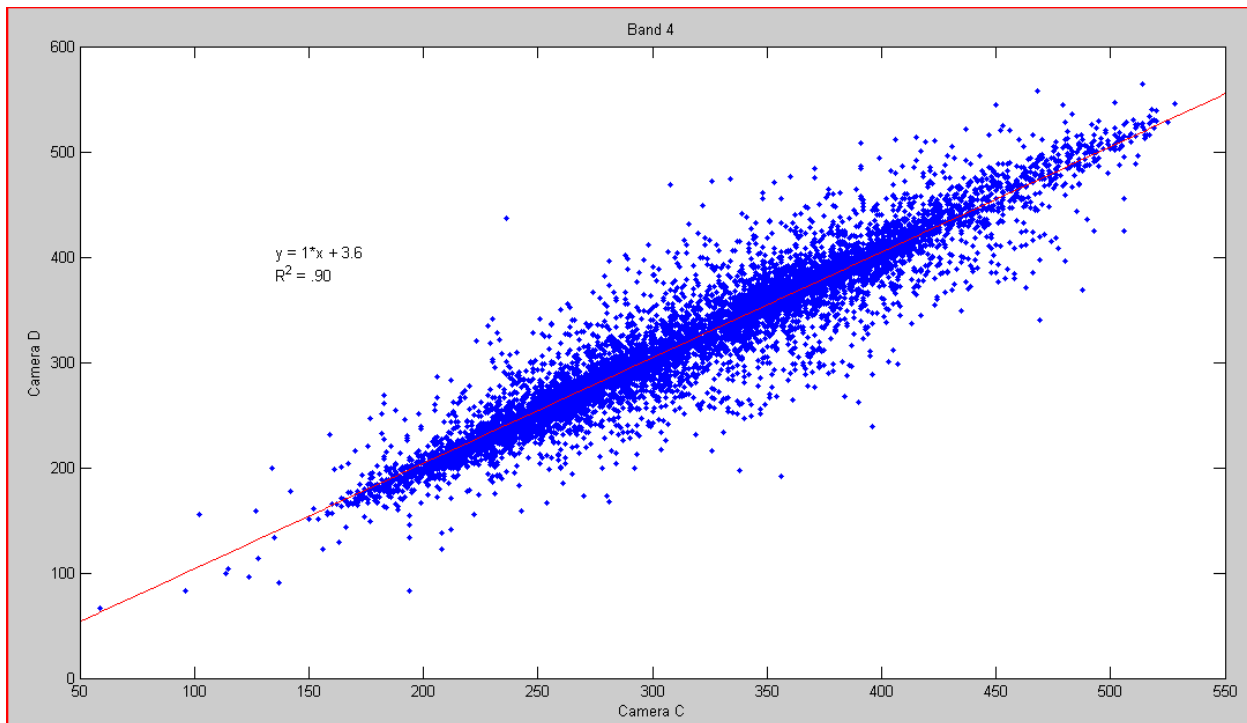


AWiFS Band 4 Quad A vs. Quad B

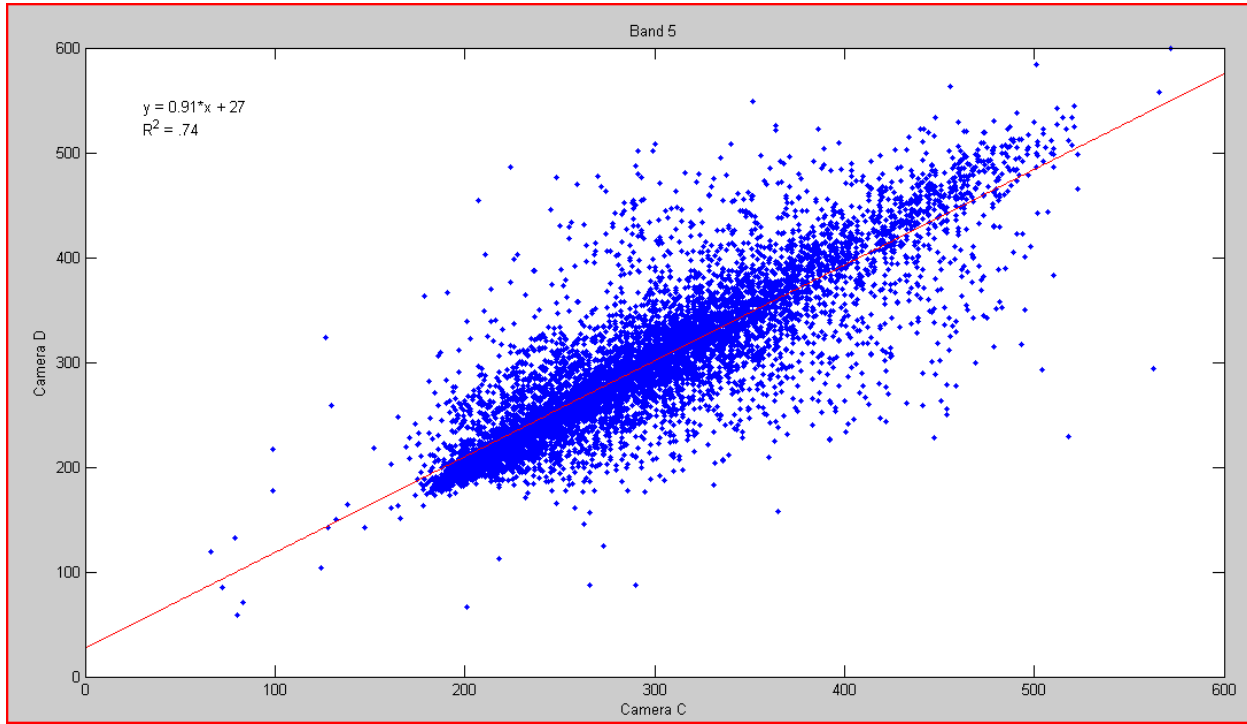


AWiFS Band 5 Quad A vs. Quad B



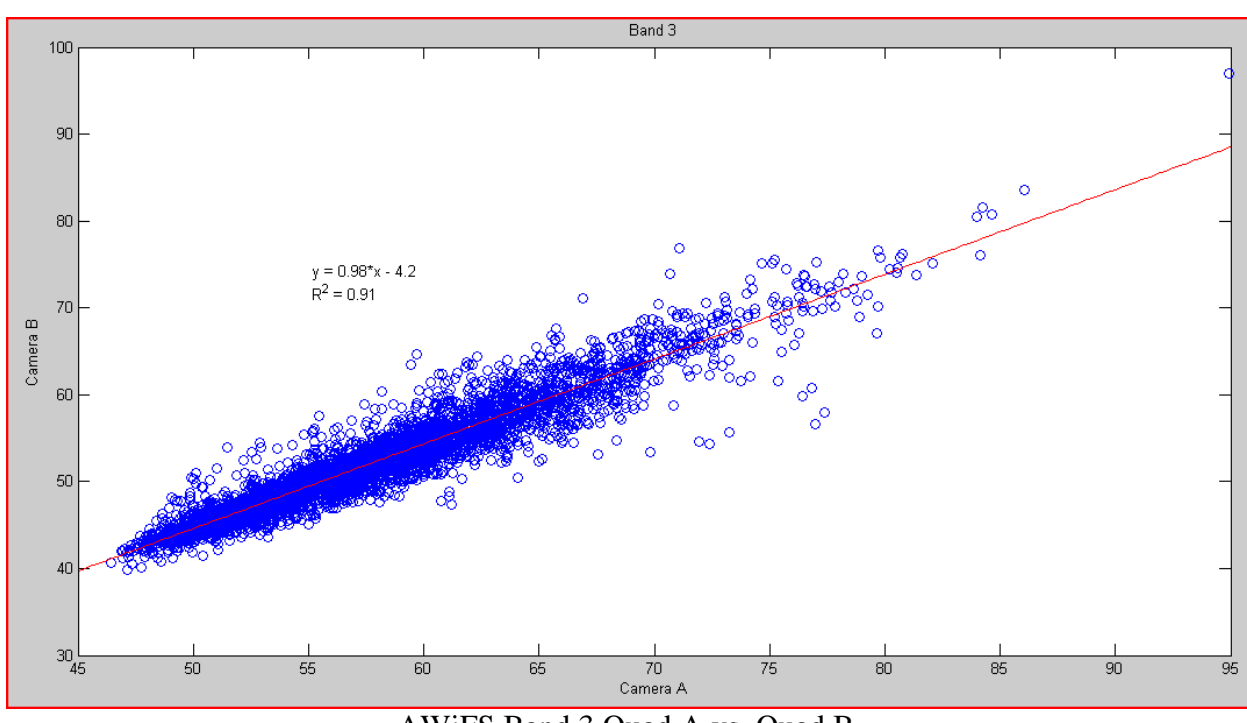
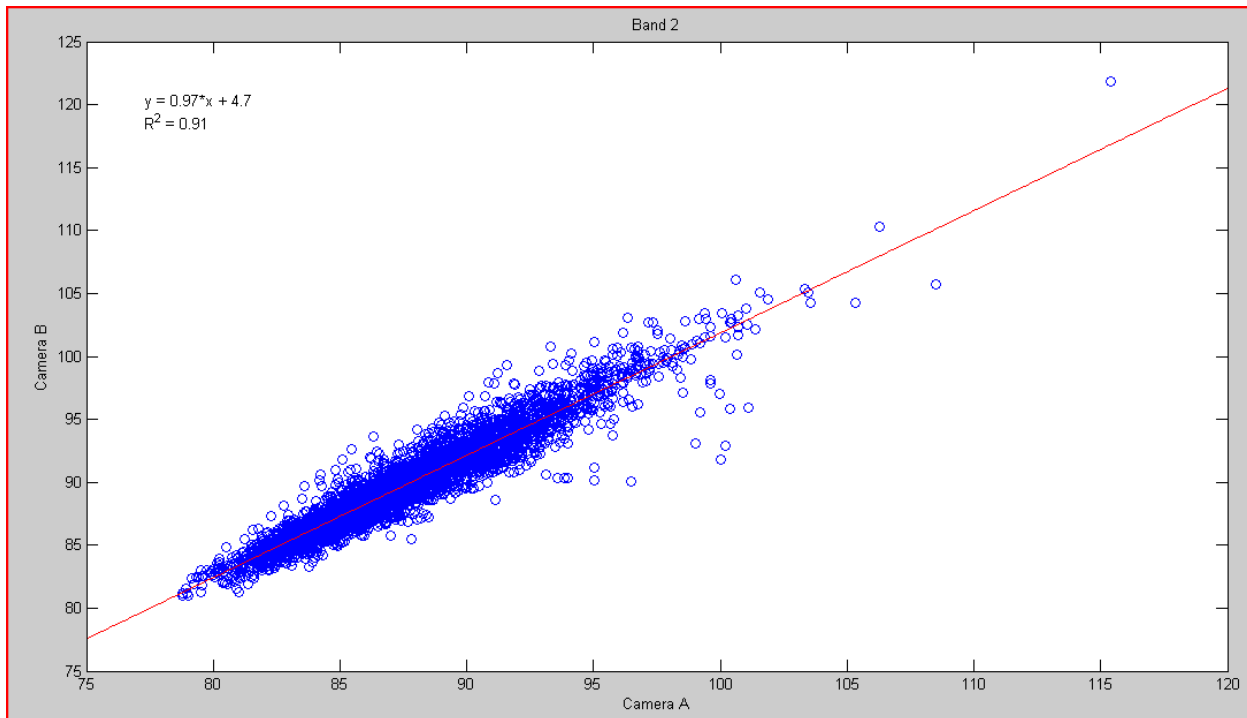


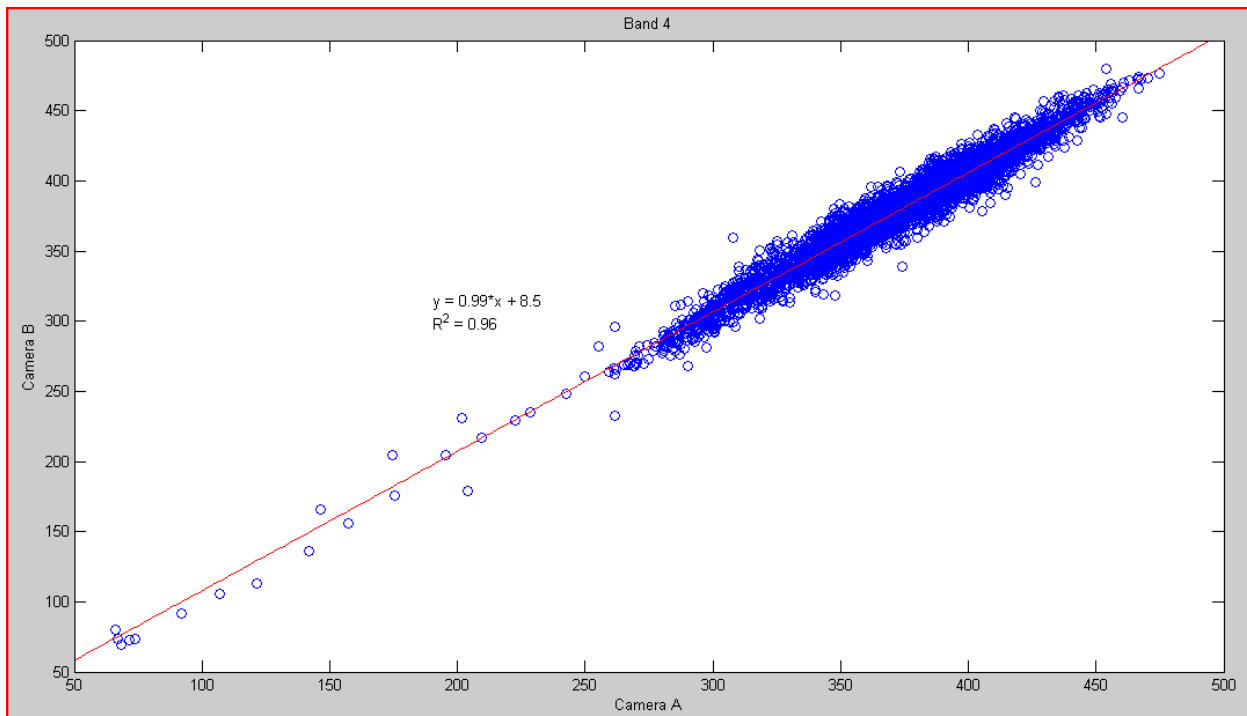
AWiFS Band 4 Quad C vs. Quad D



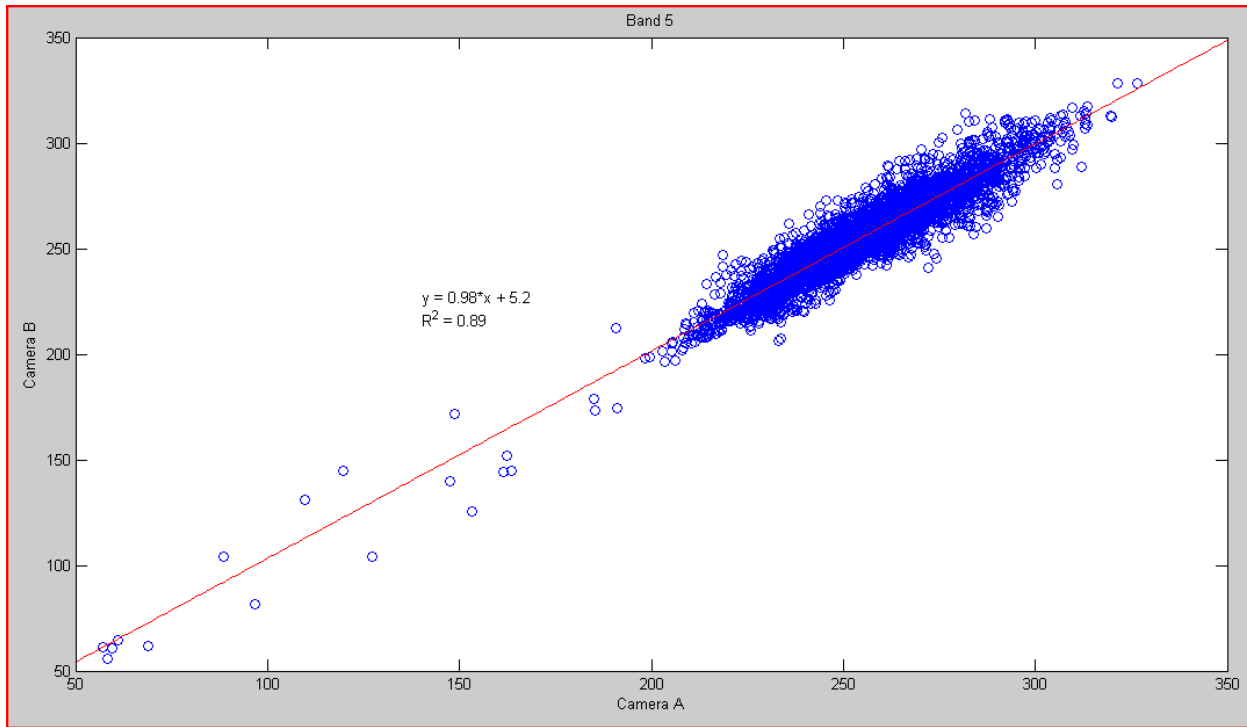
AWiFS Band 5 Quad C vs. Quad D

AWiFS Path/Row 268-40 - Acquired August 2, 2005
50 Pixel Average Comparison





AWiFS Band 4 Quad A vs. Quad B



AWiFS Band 5 Quad A vs. Quad B

Appendix 3. Reflectance Variation as a Function of Sensor View Angle

Summary of Single Scene Slope and Y-Intercept Calculated From Sensor View Angle Plots

Scene	Date	Reflect.	Classifi- cation	Band	Class	m	Sigma- m	b	Sigma- b
247-36-D	22-Jun-06	Planetary	MaxLike	Green	Woody	-0.0004	0.0002	0.0726	0.0020
247-36-D	22-Jun-06	Planetary	MaxLike	Red	Woody	0.0000	0.0002	0.0438	0.0030
247-36-D	22-Jun-06	Planetary	MaxLike	NIR	Woody	-0.0027	0.0010	0.2070	0.0200
247-36-D	22-Jun-06	Planetary	MaxLike	SWIR	Woody	-0.0003	0.0008	0.1330	0.0100
247-36-D	22-Jun-06	Planetary	MaxLike	Green	Non-Woody	-0.0003	0.0001	0.0855	0.0020
247-36-D	22-Jun-06	Planetary	MaxLike	Red	Non-Woody	-0.0001	0.0002	0.0560	0.0030
247-36-D	22-Jun-06	Planetary	MaxLike	NIR	Non-Woody	0.0014	0.0020	0.2990	0.0300
247-36-D	22-Jun-06	Planetary	MaxLike	SWIR	Non-Woody	-0.0001	0.0003	0.1744	0.0050
247-36-D	22-Jun-06	Planetary	MaxLike	Green	Bare	-0.0002	0.0006	0.1097	0.0050
247-36-D	22-Jun-06	Planetary	MaxLike	Red	Bare	0.0000	0.0007	0.1063	0.0070
247-36-D	22-Jun-06	Planetary	MaxLike	NIR	Bare	0.0000	0.0006	0.1760	0.0070
247-36-D	22-Jun-06	Planetary	MaxLike	SWIR	Bare	-0.0003	0.0006	0.2325	0.0080
247-36-D	22-Jun-06	Planetary	MaxLike	Green	Water	0.0008	0.0005	0.0792	0.0060
247-36-D	22-Jun-06	Planetary	MaxLike	Red	Water	0.0012	0.0006	0.0524	0.0070
247-36-D	22-Jun-06	Planetary	MaxLike	NIR	Water	0.0021	0.0008	0.0470	0.0100
247-36-D	22-Jun-06	Planetary	MaxLike	SWIR	Water	0.0022	0.0007	0.0508	0.0090
255-30-C	21-Jul-08	Planetary	MaxLike	Green	Woody	-0.0003	0.0002	0.0917	0.0030
255-30-C	21-Jul-08	Planetary	MaxLike	Red	Woody	-0.0004	0.0004	0.0625	0.0050
255-30-C	21-Jul-08	Planetary	MaxLike	NIR	Woody	0.0001	0.0007	0.2220	0.0100
255-30-C	21-Jul-08	Planetary	MaxLike	SWIR	Woody	-0.0017	0.0009	0.1890	0.0100
255-30-C	21-Jul-08	Planetary	MaxLike	Green	Non-Woody	0.0001	0.0005	0.1111	0.0070
255-30-C	21-Jul-08	Planetary	MaxLike	Red	Non-Woody	0.0002	0.0005	0.0678	0.0070
255-30-C	21-Jul-08	Planetary	MaxLike	NIR	Non-Woody	-0.0005	0.0010	0.3810	0.0100
255-30-C	21-Jul-08	Planetary	MaxLike	SWIR	Non-Woody	-0.0005	0.0003	0.1366	0.0040
255-30-C	21-Jul-08	Planetary	MaxLike	Green	Bare	0.0003	0.0005	0.1670	0.0070
255-30-C	21-Jul-08	Planetary	MaxLike	Red	Bare	0.0001	0.0006	0.1472	0.0080
255-30-C	21-Jul-08	Planetary	MaxLike	NIR	Bare	0.0003	0.0007	0.1600	0.0100
255-30-C	21-Jul-08	Planetary	MaxLike	SWIR	Bare	0.0001	0.0010	0.0580	0.0100
255-30-C	21-Jul-08	Planetary	MaxLike	Green	Water	0.0006	0.0002	0.0843	0.0030
255-30-C	21-Jul-08	Planetary	MaxLike	Red	Water	0.0007	0.0002	0.0486	0.0020
255-30-C	21-Jul-08	Planetary	MaxLike	NIR	Water	0.0002	0.0001	0.0368	0.0010
255-30-C	21-Jul-08	Planetary	MaxLike	SWIR	Water	0.0004	0.0001	0.0389	0.0020

Scene	Date	Reflect.	Classifi-	Band	Class	m	Sigma-m	b	Sigma-b
257-30-C	31-Jul-08	Planetary	MaxLike	Red	Woody	-0.0001	0.0001	0.0373	0.0008
257-30-C	31-Jul-08	Planetary	MaxLike	NIR	Woody	-0.0008	0.0004	0.2690	0.0060
257-30-C	31-Jul-08	Planetary	MaxLike	SWIR	Woody	-0.0007	0.0003	0.1363	0.0040
257-30-C	31-Jul-08	Planetary	MaxLike	Green	Non-Woody	-0.0001	0.0003	0.0956	0.0050
257-30-C	31-Jul-08	Planetary	MaxLike	Red	Non-Woody	-0.0001	0.0002	0.0510	0.0030
257-30-C	31-Jul-08	Planetary	MaxLike	NIR	Non-Woody	-0.0005	0.0010	0.3500	0.0200
257-30-C	31-Jul-08	Planetary	MaxLike	SWIR	Non-Woody	-0.0009	0.0004	0.1141	0.0060
257-30-C	31-Jul-08	Planetary	MaxLike	Green	Bare	-0.0007	0.0003	0.1026	0.0040
257-30-C	31-Jul-08	Planetary	MaxLike	Red	Bare	-0.0010	0.0005	0.0870	0.0060
257-30-C	31-Jul-08	Planetary	MaxLike	NIR	Bare	-0.0007	0.0004	0.1744	0.0050
257-30-C	31-Jul-08	Planetary	MaxLike	SWIR	Bare	-0.0017	0.0007	0.2487	0.0090
257-30-C	31-Jul-08	Planetary	MaxLike	Green	Water	-0.0003	0.0003	0.0702	0.0040
257-30-C	31-Jul-08	Planetary	MaxLike	Red	Water	-0.0002	0.0003	0.0377	0.0030
257-30-C	31-Jul-08	Planetary	MaxLike	NIR	Water	-0.0001	0.0003	0.0426	0.0040
257-30-C	31-Jul-08	Planetary	MaxLike	SWIR	Water	-0.0001	0.0002	0.0346	0.0030
262-35-A	1-Aug-08	Planetary	MaxLike	Green	Woody	-0.0002	0.0001	0.0730	0.0010
262-35-A	1-Aug-08	Planetary	MaxLike	Red	Woody	-0.0001	0.0001	0.0364	0.0009
262-35-A	1-Aug-08	Planetary	MaxLike	NIR	Woody	-0.0003	0.0004	0.2760	0.0070
262-35-A	1-Aug-08	Planetary	MaxLike	SWIR	Woody	-0.0009	0.0003	0.1413	0.0050
262-35-A	1-Aug-08	Planetary	MaxLike	Green	Non-Woody	-0.0002	0.0003	0.0904	0.0040
262-35-A	1-Aug-08	Planetary	MaxLike	Red	Non-Woody	-0.0001	0.0002	0.0533	0.0030
262-35-A	1-Aug-08	Planetary	MaxLike	NIR	Non-Woody	-0.0014	0.0010	0.2860	0.0200
262-35-A	1-Aug-08	Planetary	MaxLike	SWIR	Non-Woody	0.0001	0.0003	0.1498	0.0050
262-35-A	1-Aug-08	Planetary	MaxLike	Green	Bare	-0.0007	0.0003	0.1078	0.0030
262-35-A	1-Aug-08	Planetary	MaxLike	Red	Bare	-0.0007	0.0004	0.0976	0.0040
262-35-A	1-Aug-08	Planetary	MaxLike	NIR	Bare	-0.0007	0.0004	0.1720	0.0050
262-35-A	1-Aug-08	Planetary	MaxLike	SWIR	Bare	-0.0010	0.0005	0.2763	0.0060
262-35-A	1-Aug-08	Planetary	MaxLike	Green	Water	0.0005	0.0001	0.0817	0.0020
262-35-A	1-Aug-08	Planetary	MaxLike	Red	Water	0.0005	0.0001	0.0437	0.0020
262-35-A	1-Aug-08	Planetary	MaxLike	NIR	Water	0.0001	0.0001	0.0316	0.0010
262-35-A	1-Aug-08	Planetary	MaxLike	SWIR	Water	-0.0001	0.0001	0.0345	0.0010

Scene	Date	Reflect.	Classifi- cation	Band	Class	m	Sigma- m	b	Sigma- b
263-35-A	6-Aug-08	Planetary	MaxLike	Green	Woody	-0.0001	0.0001	0.0759	0.0009
263-35-A	6-Aug-08	Planetary	MaxLike	Red	Woody	-0.0001	0.0001	0.0384	0.0008
263-35-A	6-Aug-08	Planetary	MaxLike	NIR	Woody	0.0001	0.0004	0.2723	0.0050
263-35-A	6-Aug-08	Planetary	MaxLike	SWIR	Woody	-0.0004	0.0002	0.1386	0.0030
263-35-A	6-Aug-08	Planetary	MaxLike	Green	Non-Woody	-0.0002	0.0001	0.1103	0.0020
263-35-A	6-Aug-08	Planetary	MaxLike	Red	Non-Woody	-0.0004	0.0002	0.0582	0.0020
263-35-A	6-Aug-08	Planetary	MaxLike	NIR	Non-Woody	0.0009	0.0007	0.3860	0.0100
263-35-A	6-Aug-08	Planetary	MaxLike	SWIR	Non-Woody	-0.0010	0.0004	0.1037	0.0060
263-35-A	6-Aug-08	Planetary	MaxLike	Green	Bare	0.0002	0.0005	0.1423	0.0080
263-35-A	6-Aug-08	Planetary	MaxLike	Red	Bare	0.0003	0.0006	0.1520	0.0100
263-35-A	6-Aug-08	Planetary	MaxLike	NIR	Bare	0.0001	0.0007	0.2210	0.0100
263-35-A	6-Aug-08	Planetary	MaxLike	SWIR	Bare	-0.0006	0.0007	0.3020	0.0100
263-35-A	6-Aug-08	Planetary	MaxLike	Green	Water	-0.0009	0.0002	0.0806	0.0020
263-35-A	6-Aug-08	Planetary	MaxLike	Red	Water	-0.0003	0.0002	0.0481	0.0020
263-35-A	6-Aug-08	Planetary	MaxLike	NIR	Water	0.0003	0.0001	0.0367	0.0020
263-35-A	6-Aug-08	Planetary	MaxLike	SWIR	Water	-0.0007	0.0001	0.0254	0.0010
281-48-C	7-Jan-06	Planetary	MaxLike	Green	Woody	-0.0001	0.0001	0.1005	0.0020
281-48-C	7-Jan-06	Planetary	MaxLike	Red	Woody	0.0000	0.0002	0.0697	0.0030
281-48-C	7-Jan-06	Planetary	MaxLike	NIR	Woody	-0.0009	0.0005	0.1843	0.0070
281-48-C	7-Jan-06	Planetary	MaxLike	SWIR	Woody	-0.0006	0.0007	0.1720	0.0100
281-48-C	7-Jan-06	Planetary	MaxLike	Green	Non-Woody	0.0000	0.0003	0.1210	0.0040
281-48-C	7-Jan-06	Planetary	MaxLike	Red	Non-Woody	0.0002	0.0005	0.1055	0.0070
281-48-C	7-Jan-06	Planetary	MaxLike	NIR	Non-Woody	-0.0005	0.0007	0.2030	0.0100
281-48-C	7-Jan-06	Planetary	MaxLike	SWIR	Non-Woody	0.0004	0.0010	0.2670	0.0100
281-48-C	7-Jan-06	Planetary	MaxLike	Green	Bare	-0.0001	0.0003	0.1440	0.0040
281-48-C	7-Jan-06	Planetary	MaxLike	Red	Bare	0.0000	0.0005	0.1380	0.0060
281-48-C	7-Jan-06	Planetary	MaxLike	NIR	Bare	-0.0007	0.0006	0.2264	0.0090
281-48-C	7-Jan-06	Planetary	MaxLike	SWIR	Bare	-0.0009	0.0009	0.3210	0.0100
281-48-C	7-Jan-06	Planetary	MaxLike	Green	Water	-0.0013	0.0002	0.0814	0.0020
281-48-C	7-Jan-06	Planetary	MaxLike	Red	Water	-0.0009	0.0002	0.0369	0.0020
281-48-C	7-Jan-06	Planetary	MaxLike	NIR	Water	-0.0002	0.0002	0.0187	0.0020
281-48-C	7-Jan-06	Planetary	MaxLike	SWIR	Water	0.0001	0.0002	0.0098	0.0020

Scene	Date	Reflect.	Classifi- cation	Band	Class	m	Sigma- m	b	Sigma- b
265-45-D	18-Apr-08	Planetary	CDL	Green	Woody	-0.0013	0.0004	0.1273	0.0060
265-45-D	18-Apr-08	Planetary	CDL	Red	Woody	-0.0013	0.0004	0.1272	0.0060
265-45-D	18-Apr-08	Planetary	CDL	NIR	Woody	-0.0013	0.0004	0.1273	0.0060
265-45-D	18-Apr-08	Planetary	CDL	SWIR	Woody	-0.0013	0.0004	0.1273	0.0060
265-45-D	18-Apr-08	Planetary	CDL	Green	Non-woody	-0.0018	0.0005	0.1514	0.0070
265-45-D	18-Apr-08	Planetary	CDL	Red	Non-woody	-0.0018	0.0005	0.1515	0.0070
265-45-D	18-Apr-08	Planetary	CDL	NIR	Non-woody	-0.0018	0.0005	0.1513	0.0070
265-45-D	18-Apr-08	Planetary	CDL	SWIR	Non-woody	-0.0018	0.0005	0.1513	0.0070
265-45-D	18-Apr-08	Planetary	CDL	Green	Bare	-0.0028	-0.0010	0.2090	0.0200
265-45-D	18-Apr-08	Planetary	CDL	Red	Bare	-0.0028	-0.0010	0.2090	0.0200
265-45-D	18-Apr-08	Planetary	CDL	NIR	Bare	-0.0029	-0.0010	0.2090	0.0200
265-45-D	18-Apr-08	Planetary	CDL	SWIR	Bare	-0.0028	-0.0010	0.2090	0.0200
265-45-D	18-Apr-08	Planetary	CDL	Green	Water	-0.0006	0.0010	0.1350	0.0200
265-45-D	18-Apr-08	Planetary	CDL	Red	Water	-0.0006	0.0010	0.1350	0.0200
265-45-D	18-Apr-08	Planetary	CDL	NIR	Water	-0.0006	0.0010	0.1350	0.0200
265-45-D	18-Apr-08	Planetary	CDL	SWIR	Water	-0.0006	0.0010	0.1350	0.0200
265-45-D	18-Apr-08	Planetary	MaxLike	Green	Woody	-0.0002	0.0002	0.1018	0.0030
265-45-D	18-Apr-08	Planetary	MaxLike	Red	Woody	-0.0002	0.0002	0.1018	0.0030
265-45-D	18-Apr-08	Planetary	MaxLike	NIR	Woody	-0.0002	0.0002	0.1018	0.0030
265-45-D	18-Apr-08	Planetary	MaxLike	SWIR	Woody	-0.0002	0.0002	0.1018	0.0030
265-45-D	18-Apr-08	Planetary	MaxLike	Green	Non-woody	-0.0001	0.0002	0.0881	0.0020
265-45-D	18-Apr-08	Planetary	MaxLike	Red	Non-woody	-0.0001	0.0002	0.0881	0.0020
265-45-D	18-Apr-08	Planetary	MaxLike	NIR	Non-woody	-0.0001	0.0002	0.0881	0.0020
265-45-D	18-Apr-08	Planetary	MaxLike	SWIR	Non-woody	-0.0001	0.0002	0.0881	0.0020
265-45-D	18-Apr-08	Planetary	MaxLike	Green	Bare	0.0002	0.0005	0.1572	0.0070
265-45-D	18-Apr-08	Planetary	MaxLike	Red	Bare	0.0002	0.0005	0.1572	0.0070
265-45-D	18-Apr-08	Planetary	MaxLike	NIR	Bare	0.0002	0.0005	0.1572	0.0070
265-45-D	18-Apr-08	Planetary	MaxLike	SWIR	Bare	0.0002	0.0005	0.1573	0.0070
265-45-D	18-Apr-08	Planetary	MaxLike	Green	Water	0.0011	0.0006	0.1063	0.0070
265-45-D	18-Apr-08	Planetary	MaxLike	Red	Water	0.0011	0.0006	0.1063	0.0070
265-45-D	18-Apr-08	Planetary	MaxLike	NIR	Water	0.0011	0.0006	0.1063	0.0070
265-45-D	18-Apr-08	Planetary	MaxLike	SWIR	Water	0.0011	0.0006	0.1063	0.0070

Scene	Date	Reflect.	Classifi- cation	Band	Class	m	Sigma- m	b	Sigma- b
265-45-D	5-Jun-08	Planetary	CDL	Green	Woody	-0.0014	0.0005	0.1354	0.0070
265-45-D	5-Jun-08	Planetary	CDL	Red	Woody	-0.0014	0.0005	0.1353	0.0070
265-45-D	5-Jun-08	Planetary	CDL	NIR	Woody	-0.0014	0.0005	0.1353	0.0070
265-45-D	5-Jun-08	Planetary	CDL	SWIR	Woody	-0.0014	0.0005	0.1354	0.0090
265-45-D	5-Jun-08	Planetary	CDL	Green	Non-woody	-0.0017	0.0006	0.1592	0.0090
265-45-D	5-Jun-08	Planetary	CDL	Red	Non-woody	-0.0017	0.0006	0.1594	0.0090
265-45-D	5-Jun-08	Planetary	CDL	NIR	Non-woody	-0.0017	0.0006	0.1594	0.0090
265-45-D	5-Jun-08	Planetary	CDL	SWIR	Non-woody	-0.0017	0.0006	0.1592	0.0200
265-45-D	5-Jun-08	Planetary	CDL	Green	Bare	-0.0032	0.0010	0.2290	0.0200
265-45-D	5-Jun-08	Planetary	CDL	Red	Bare	-0.0032	0.0010	0.2290	0.0200
265-45-D	5-Jun-08	Planetary	CDL	NIR	Bare	-0.0032	0.0010	0.2290	0.0200
265-45-D	5-Jun-08	Planetary	CDL	SWIR	Bare	-0.0032	0.0010	0.2290	0.0200
265-45-D	5-Jun-08	Planetary	CDL	Green	Water	-0.0017	0.0010	0.1890	0.0200
265-45-D	5-Jun-08	Planetary	CDL	Red	Water	-0.0017	0.0010	0.1890	0.0200
265-45-D	5-Jun-08	Planetary	CDL	NIR	Water	-0.0017	0.0010	0.1890	0.0200
265-45-D	5-Jun-08	Planetary	CDL	SWIR	Water	-0.0017	0.0010	0.1890	0.0030
265-45-D	5-Jun-08	Planetary	MaxLike	Green	Woody	-0.0005	0.0002	0.1150	0.0030
265-45-D	5-Jun-08	Planetary	MaxLike	Red	Woody	-0.0005	0.0002	0.1150	0.0030
265-45-D	5-Jun-08	Planetary	MaxLike	NIR	Woody	-0.0005	0.0002	0.1150	0.0030
265-45-D	5-Jun-08	Planetary	MaxLike	SWIR	Woody	-0.0005	0.0002	0.1150	0.0030
265-45-D	5-Jun-08	Planetary	MaxLike	Green	Non-woody	-0.0006	0.0002	0.1298	0.0030
265-45-D	5-Jun-08	Planetary	MaxLike	Red	Non-woody	-0.0006	0.0002	0.1298	0.0030
265-45-D	5-Jun-08	Planetary	MaxLike	NIR	Non-woody	-0.0006	0.0002	0.1298	0.0030
265-45-D	5-Jun-08	Planetary	MaxLike	SWIR	Non-woody	-0.0006	0.0002	0.1298	0.0100
265-45-D	5-Jun-08	Planetary	MaxLike	Green	Bare	-0.0004	0.0008	0.1870	0.0100
265-45-D	5-Jun-08	Planetary	MaxLike	Red	Bare	-0.0004	0.0008	0.1870	0.0100
265-45-D	5-Jun-08	Planetary	MaxLike	NIR	Bare	-0.0004	0.0008	0.1870	0.0100
265-45-D	5-Jun-08	Planetary	MaxLike	SWIR	Bare	-0.0004	0.0008	0.1870	0.0050
265-45-D	5-Jun-08	Planetary	MaxLike	Green	Water	0.0007	0.0004	0.1447	0.0050
265-45-D	5-Jun-08	Planetary	MaxLike	Red	Water	0.0007	0.0004	0.1447	0.0050
265-45-D	5-Jun-08	Planetary	MaxLike	NIR	Water	0.0007	0.0004	0.1447	0.0050
265-45-D	5-Jun-08	Planetary	MaxLike	SWIR	Water	0.0007	0.0004	0.1447	0.0070

Scene	Date	Reflect.	Classifi- cation	Band	Class	m	Sigma- m	b	Sigma- b
266-45-B	14-Sep-08	Planetary	CDL	Green	Woody	-0.0014	0.0004	0.0958	0.0050
266-45-B	14-Sep-08	Planetary	CDL	Red	Woody	-0.0014	0.0004	0.0958	0.0050
266-45-B	14-Sep-08	Planetary	CDL	NIR	Woody	-0.0014	0.0004	0.0960	0.0050
266-45-B	14-Sep-08	Planetary	CDL	SWIR	Woody	-0.0014	0.0004	0.0960	0.0050
266-45-B	14-Sep-08	Planetary	CDL	Green	Non-woody	-0.0010	0.0006	0.1030	0.0070
266-45-B	14-Sep-08	Planetary	CDL	Red	Non-woody	-0.0010	0.0006	0.1028	0.0070
266-45-B	14-Sep-08	Planetary	CDL	NIR	Non-woody	-0.0010	0.0006	0.1028	0.0070
266-45-B	14-Sep-08	Planetary	CDL	SWIR	Non-woody	-0.0010	0.0006	0.1031	0.0070
266-45-B	14-Sep-08	Planetary	CDL	Green	Bare	-0.0013	0.0010	0.1410	0.0200
266-45-B	14-Sep-08	Planetary	CDL	Red	Bare	-0.0013	0.0010	0.1410	0.0200
266-45-B	14-Sep-08	Planetary	CDL	NIR	Bare	-0.0013	0.0010	0.1410	0.0200
266-45-B	14-Sep-08	Planetary	CDL	SWIR	Bare	-0.0013	0.0010	0.1410	0.0200
266-45-B	14-Sep-08	Planetary	CDL	Green	Water	-0.0006	0.0005	0.1003	0.0060
266-45-B	14-Sep-08	Planetary	CDL	Red	Water	-0.0006	0.0005	0.1004	0.0060
266-45-B	14-Sep-08	Planetary	CDL	NIR	Water	-0.0006	0.0005	0.1004	0.0060
266-45-B	14-Sep-08	Planetary	CDL	SWIR	Water	-0.0006	0.0005	0.1003	0.0060
266-45-B	14-Sep-08	Planetary	MaxLike	Green	Woody	-0.0003	0.0001	0.0784	0.0010
266-45-B	14-Sep-08	Planetary	MaxLike	Red	Woody	-0.0003	0.0001	0.0784	0.0010
266-45-B	14-Sep-08	Planetary	MaxLike	NIR	Woody	-0.0003	0.0001	0.0784	0.0010
266-45-B	14-Sep-08	Planetary	MaxLike	SWIR	Woody	-0.0003	0.0001	0.0784	0.0010
266-45-B	14-Sep-08	Planetary	MaxLike	Green	Non-woody	-0.0002	0.0001	0.0800	0.0009
266-45-B	14-Sep-08	Planetary	MaxLike	Red	Non-woody	-0.0002	0.0001	0.0800	0.0009
266-45-B	14-Sep-08	Planetary	MaxLike	NIR	Non-woody	-0.0002	0.0001	0.0800	0.0009
266-45-B	14-Sep-08	Planetary	MaxLike	SWIR	Non-woody	-0.0002	0.0001	0.0800	0.0009
266-45-B	14-Sep-08	Planetary	MaxLike	Green	Bare	-0.0004	0.0002	0.0945	0.0030
266-45-B	14-Sep-08	Planetary	MaxLike	Red	Bare	-0.0004	0.0002	0.0946	0.0030
266-45-B	14-Sep-08	Planetary	MaxLike	NIR	Bare	-0.0004	0.0002	0.0946	0.0030
266-45-B	14-Sep-08	Planetary	MaxLike	SWIR	Bare	-0.0004	0.0002	0.0946	0.0030
266-45-B	14-Sep-08	Planetary	MaxLike	Green	Water	-0.0001	0.0003	0.1046	0.0040
266-45-B	14-Sep-08	Planetary	MaxLike	Red	Water	-0.0001	0.0003	0.1046	0.0040
266-45-B	14-Sep-08	Planetary	MaxLike	NIR	Water	-0.0001	0.0003	0.1045	0.0040
266-45-B	14-Sep-08	Planetary	MaxLike	SWIR	Water	-0.0001	0.0003	0.1045	0.0040

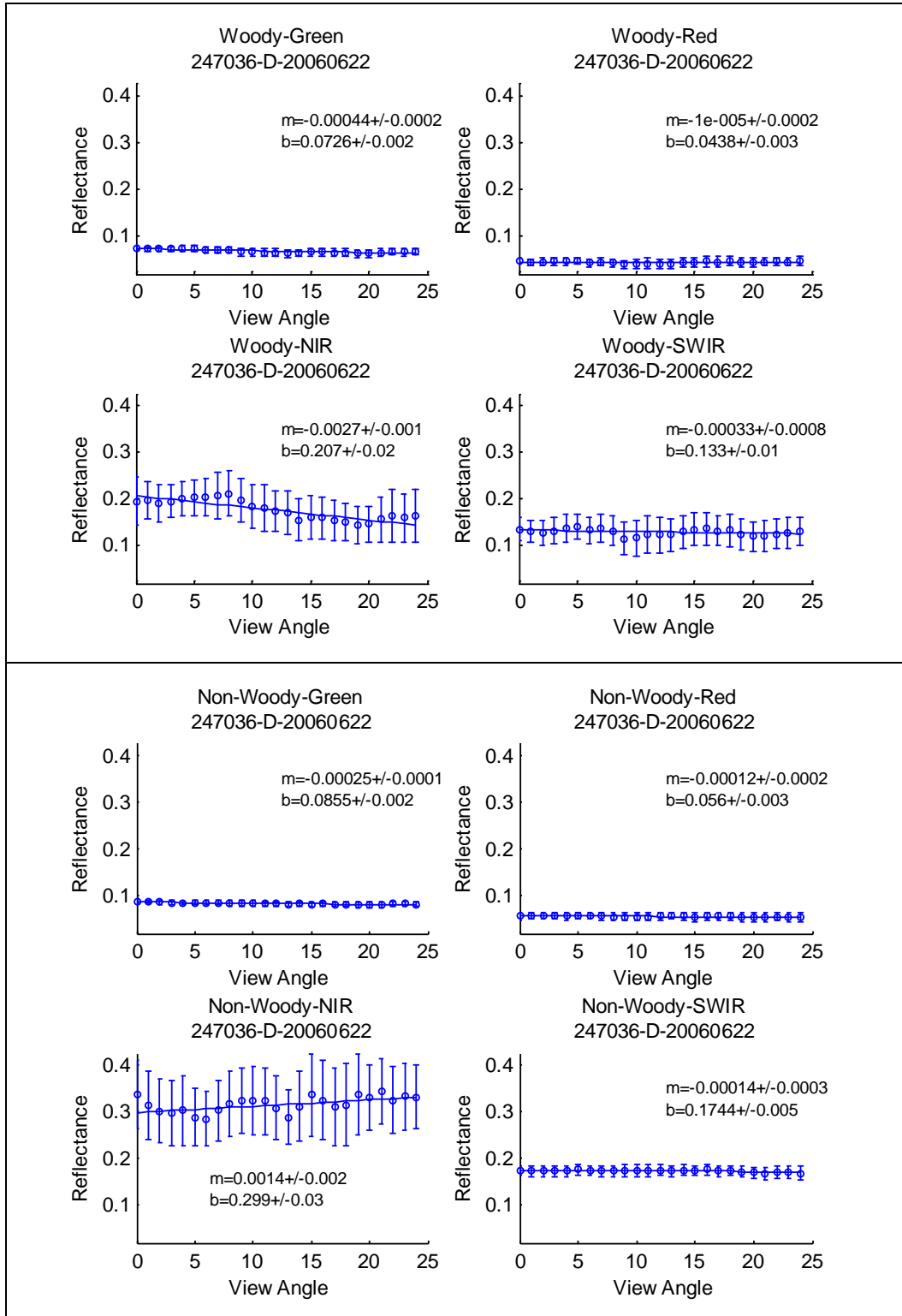
Scene	Date	Reflect.	Classifi- cation	Band	Class	m	Sigma- m	b	Sigma- b
266-45-D	10-Jun-08	Planetary	CDL	Green	Woody	-0.0013	0.0006	0.1169	0.0050
266-45-D	10-Jun-08	Planetary	CDL	Red	Woody	-0.0013	0.0006	0.1170	0.0050
266-45-D	10-Jun-08	Planetary	CDL	NIR	Woody	-0.0013	0.0006	0.1168	0.0050
266-45-D	10-Jun-08	Planetary	CDL	SWIR	Woody	-0.0013	0.0006	0.1169	0.0050
266-45-D	10-Jun-08	Planetary	CDL	Green	Non-woody	-0.0014	0.0006	0.1324	0.0060
266-45-D	10-Jun-08	Planetary	CDL	Red	Non-woody	-0.0014	0.0006	0.1325	0.0060
266-45-D	10-Jun-08	Planetary	CDL	NIR	Non-woody	-0.0014	0.0006	0.1325	0.0060
266-45-D	10-Jun-08	Planetary	CDL	SWIR	Non-woody	-0.0014	0.0006	0.1323	0.0060
266-45-D	10-Jun-08	Planetary	CDL	Green	Bare	-0.0006	0.0010	0.1570	0.0100
266-45-D	10-Jun-08	Planetary	CDL	Red	Bare	-0.0006	0.0010	0.1570	0.0100
266-45-D	10-Jun-08	Planetary	CDL	NIR	Bare	-0.0006	0.0010	0.1570	0.0100
266-45-D	10-Jun-08	Planetary	CDL	SWIR	Bare	-0.0006	0.0010	0.1570	0.0100
266-45-D	10-Jun-08	Planetary	CDL	Green	Water	0.0017	0.0010	0.1440	0.0100
266-45-D	10-Jun-08	Planetary	CDL	Red	Water	0.0017	0.0010	0.1440	0.0100
266-45-D	10-Jun-08	Planetary	CDL	NIR	Water	0.0018	0.0010	0.1440	0.0100
266-45-D	10-Jun-08	Planetary	CDL	SWIR	Water	0.0017	0.0010	0.1440	0.0100
266-45-D	10-Jun-08	Planetary	MaxLike	Green	Woody	0.0005	0.0002	0.1220	0.0020
266-45-D	10-Jun-08	Planetary	MaxLike	Red	Woody	0.0005	0.0002	0.1220	0.0020
266-45-D	10-Jun-08	Planetary	MaxLike	NIR	Woody	0.0005	0.0002	0.1220	0.0030
266-45-D	10-Jun-08	Planetary	MaxLike	SWIR	Woody	0.0005	0.0002	0.1220	0.0020
266-45-D	10-Jun-08	Planetary	MaxLike	Green	Non-woody	-0.0006	0.0002	0.1122	0.0020
266-45-D	10-Jun-08	Planetary	MaxLike	Red	Non-woody	-0.0006	0.0002	0.1122	0.0020
266-45-D	10-Jun-08	Planetary	MaxLike	NIR	Non-woody	-0.0006	0.0002	0.1122	0.0020
266-45-D	10-Jun-08	Planetary	MaxLike	SWIR	Non-woody	-0.0006	0.0002	0.1122	0.0020
266-45-D	10-Jun-08	Planetary	MaxLike	Green	Bare	0.0004	0.0007	0.1570	0.0080
266-45-D	10-Jun-08	Planetary	MaxLike	Red	Bare	0.0004	0.0007	0.1570	0.0080
266-45-D	10-Jun-08	Planetary	MaxLike	NIR	Bare	0.0004	0.0007	0.1570	0.0080
266-45-D	10-Jun-08	Planetary	MaxLike	SWIR	Bare	0.0004	0.0007	0.1570	0.0080
266-45-D	10-Jun-08	Planetary	MaxLike	Green	Water	0.0030	0.0006	0.1438	0.0060
266-45-D	10-Jun-08	Planetary	MaxLike	Red	Water	0.0030	0.0006	0.1438	0.0060
266-45-D	10-Jun-08	Planetary	MaxLike	NIR	Water	0.0030	0.0006	0.1438	0.0060
266-45-D	10-Jun-08	Planetary	MaxLike	SWIR	Water	0.0030	0.0006	0.1438	0.0060

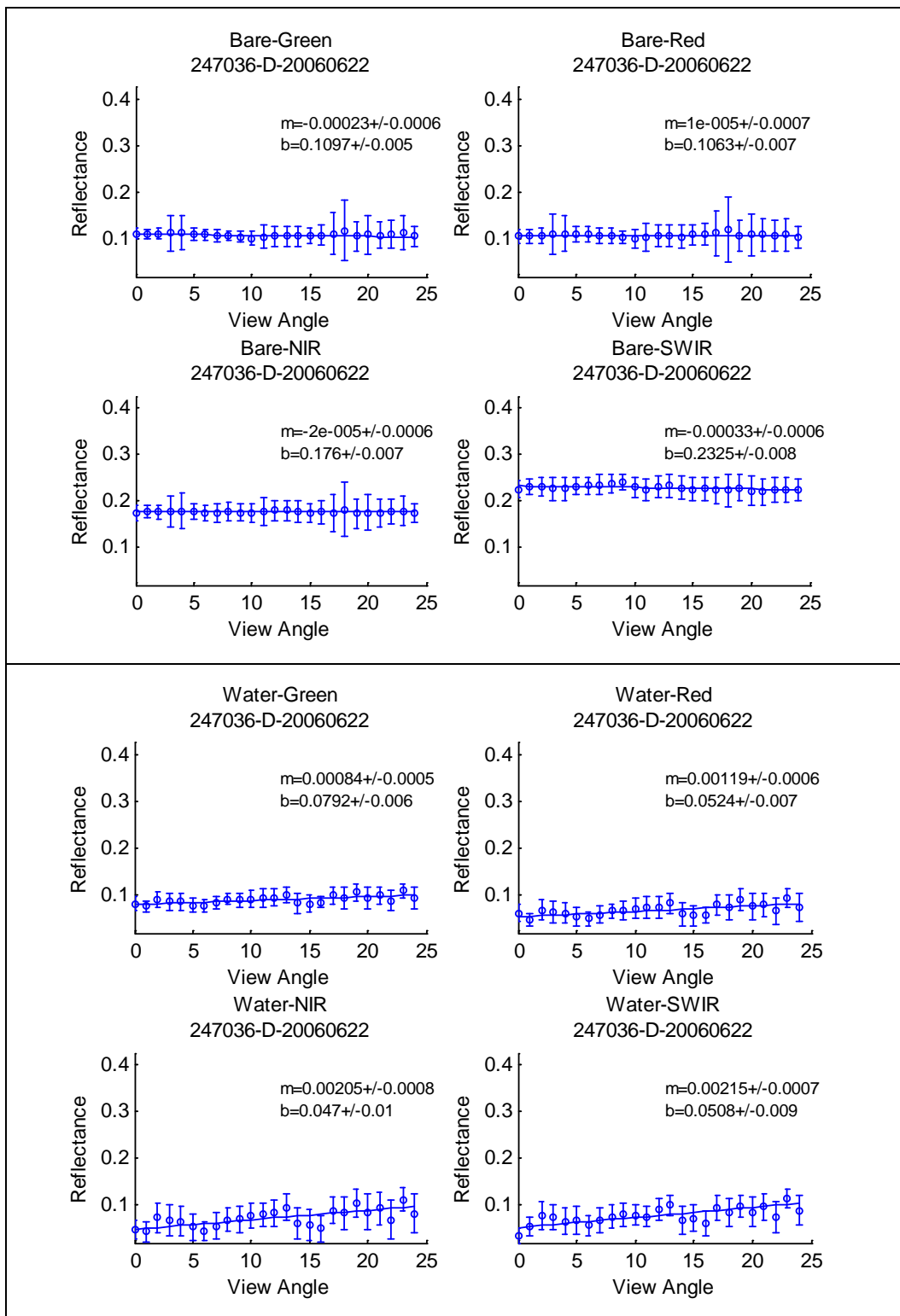
Scene	Date	Reflect.	Classifi- cation	Band	Class	m	Sigma- m	b	Sigma- b
267-45-B	19-Sep-08	Planetary	CDL	Green	Woody	0.0003	0.0008	0.0901	0.0070
267-45-B	19-Sep-08	Planetary	CDL	Red	Woody	0.0003	0.0008	0.0901	0.0070
267-45-B	19-Sep-08	Planetary	CDL	NIR	Woody	0.0003	0.0008	0.0902	0.0070
267-45-B	19-Sep-08	Planetary	CDL	SWIR	Woody	0.0003	0.0008	0.0903	0.0070
267-45-B	19-Sep-08	Planetary	CDL	Green	Non-woody	0.0007	0.0009	0.1033	0.0090
267-45-B	19-Sep-08	Planetary	CDL	Red	Non-woody	0.0007	0.0009	0.1033	0.0090
267-45-B	19-Sep-08	Planetary	CDL	NIR	Non-woody	0.0007	0.0009	0.1035	0.0090
267-45-B	19-Sep-08	Planetary	CDL	SWIR	Non-woody	0.0007	0.0009	0.1033	0.0090
267-45-B	19-Sep-08	Planetary	CDL	Green	Bare	0.0002	0.0010	0.1400	0.0100
267-45-B	19-Sep-08	Planetary	CDL	Red	Bare	0.0002	0.0010	0.1400	0.0100
267-45-B	19-Sep-08	Planetary	CDL	NIR	Bare	0.0002	0.0010	0.1400	0.0100
267-45-B	19-Sep-08	Planetary	CDL	SWIR	Bare	0.0002	0.0010	0.1400	0.0100
267-45-B	19-Sep-08	Planetary	CDL	Green	Water	0.0007	0.0007	0.0958	0.0070
267-45-B	19-Sep-08	Planetary	CDL	Red	Water	0.0007	0.0007	0.0956	0.0070
267-45-B	19-Sep-08	Planetary	CDL	NIR	Water	0.0007	0.0007	0.0953	0.0070
267-45-B	19-Sep-08	Planetary	CDL	SWIR	Water	0.0007	0.0007	0.0954	0.0070
267-45-B	19-Sep-08	Planetary	MaxLike	Green	Woody	-0.0003	0.0002	0.0975	0.0030
267-45-B	19-Sep-08	Planetary	MaxLike	Red	Woody	-0.0003	0.0002	0.0975	0.0030
267-45-B	19-Sep-08	Planetary	MaxLike	NIR	Woody	-0.0003	0.0002	0.0975	0.0030
267-45-B	19-Sep-08	Planetary	MaxLike	SWIR	Woody	-0.0003	0.0002	0.0975	0.0030
267-45-B	19-Sep-08	Planetary	MaxLike	Green	Non-woody	0.0000	0.0001	0.0961	0.0010
267-45-B	19-Sep-08	Planetary	MaxLike	Red	Non-woody	0.0000	0.0001	0.0960	0.0010
267-45-B	19-Sep-08	Planetary	MaxLike	NIR	Non-woody	0.0000	0.0001	0.0960	0.0010
267-45-B	19-Sep-08	Planetary	MaxLike	SWIR	Non-woody	0.0000	0.0001	0.0961	0.0010
267-45-B	19-Sep-08	Planetary	MaxLike	Green	Bare	-0.0008	0.0003	0.1775	0.0040
267-45-B	19-Sep-08	Planetary	MaxLike	Red	Bare	-0.0008	0.0003	0.1775	0.0040
267-45-B	19-Sep-08	Planetary	MaxLike	NIR	Bare	-0.0008	0.0003	0.1775	0.0040
267-45-B	19-Sep-08	Planetary	MaxLike	SWIR	Bare	-0.0008	0.0003	0.1775	0.0040
267-45-B	19-Sep-08	Planetary	MaxLike	Green	Water	0.0000	0.0001	0.1085	0.0010
267-45-B	19-Sep-08	Planetary	MaxLike	Red	Water	0.0000	0.0001	0.1085	0.0010
267-45-B	19-Sep-08	Planetary	MaxLike	NIR	Water	0.0000	0.0001	0.1085	0.0010
267-45-B	19-Sep-08	Planetary	MaxLike	SWIR	Water	0.0000	0.0001	0.1085	0.0010

Single Scene Sensor View Angle Plots

AWiFS Path/Row 247-36 Quad D - Acquired June 22, 2006

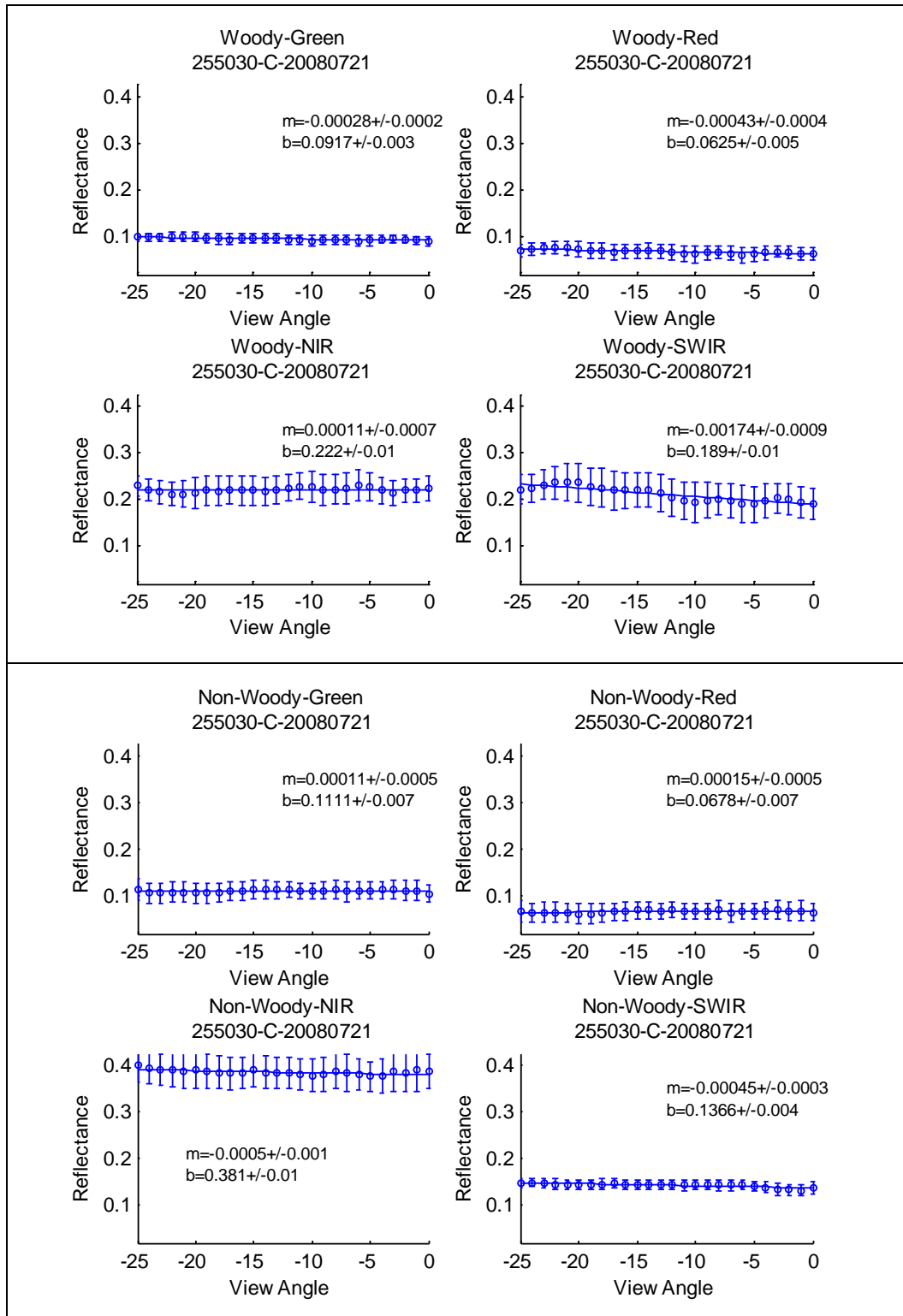
Reflectance as a function of Sensor View Angle based on Maximum Likelihood Classification

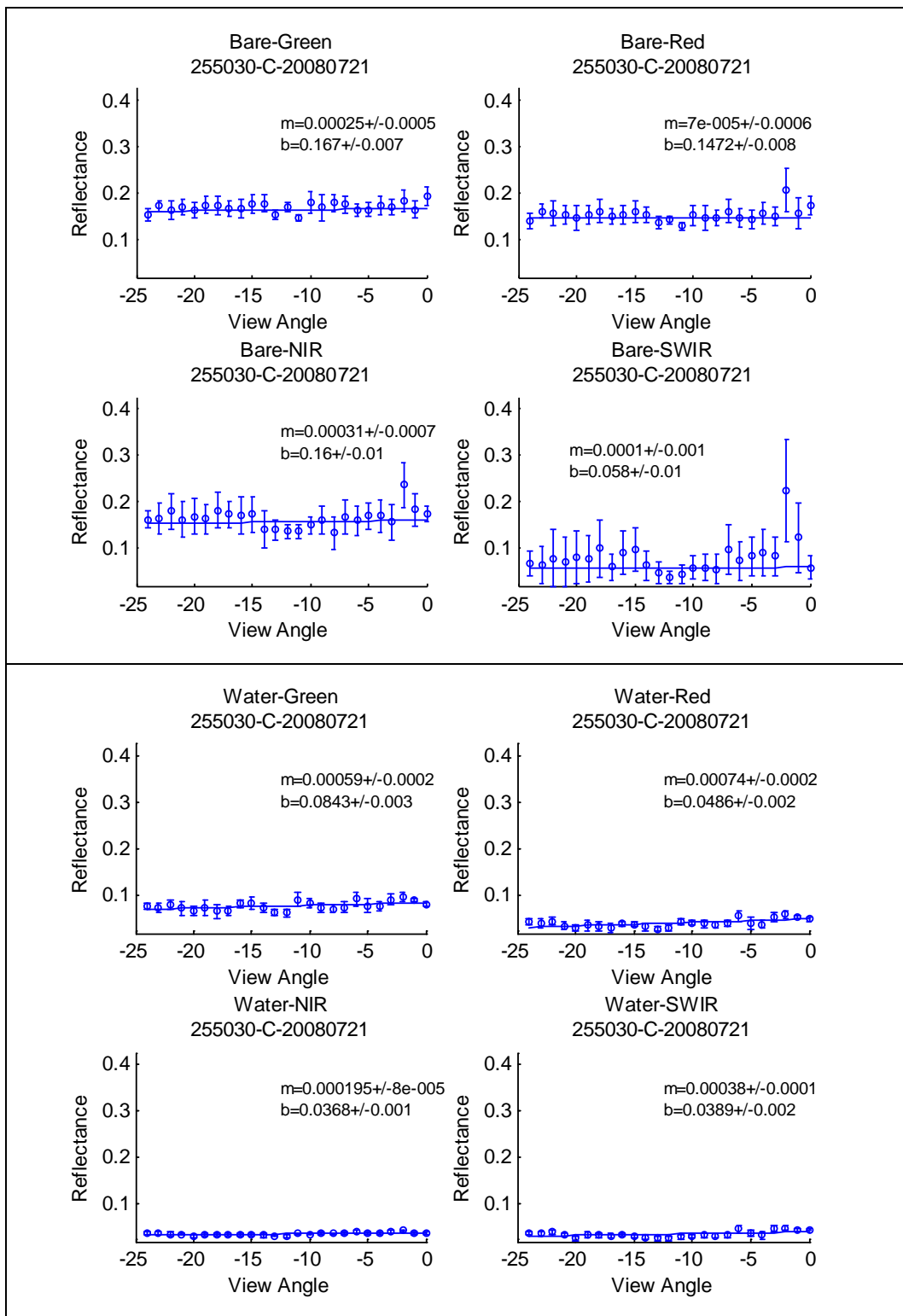




AWiFS Path/Row 255-30 Quad C - Acquired July 21, 2008

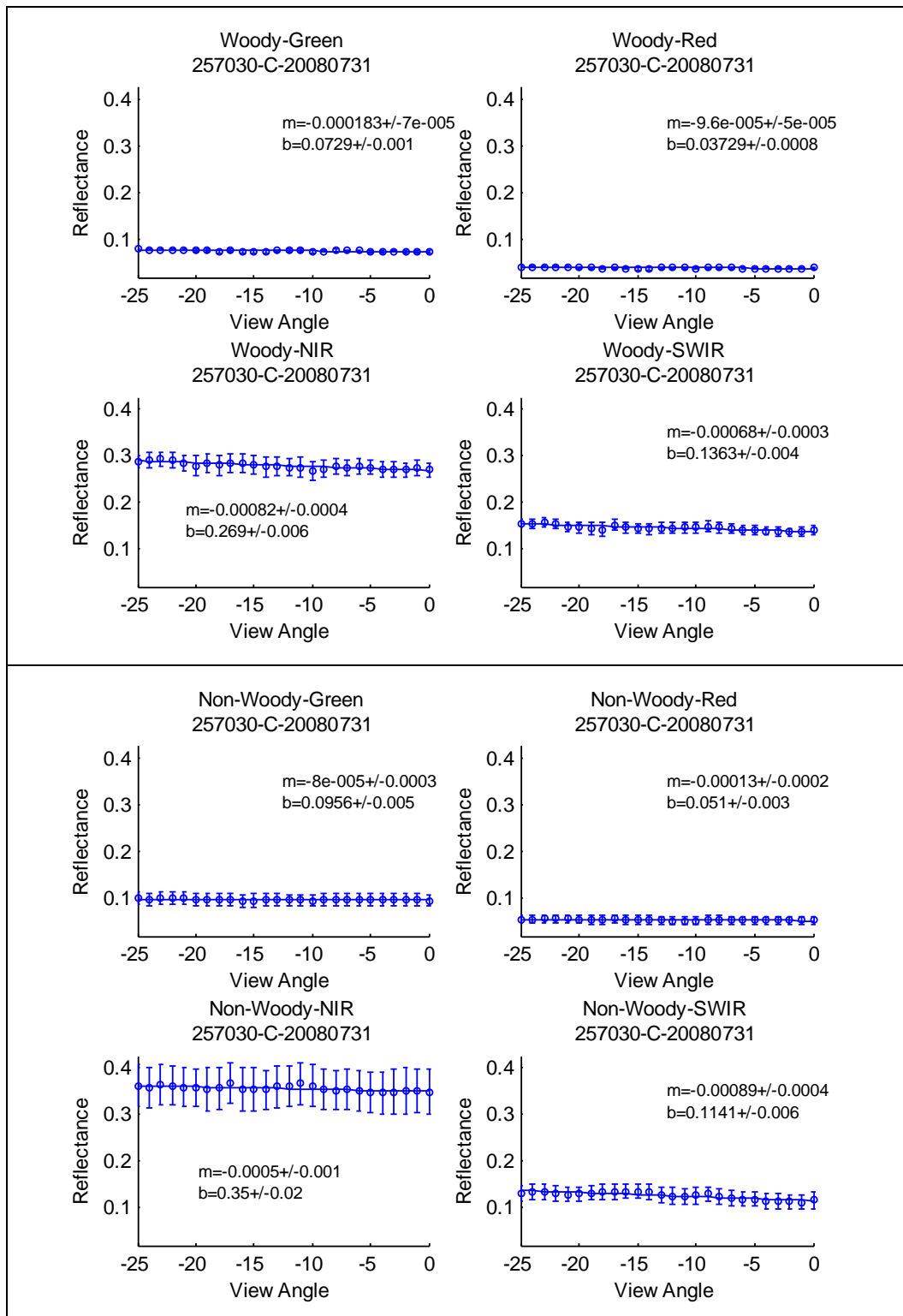
Reflectance as a function of Sensor View Angle based on Maximum Likelihood Classification

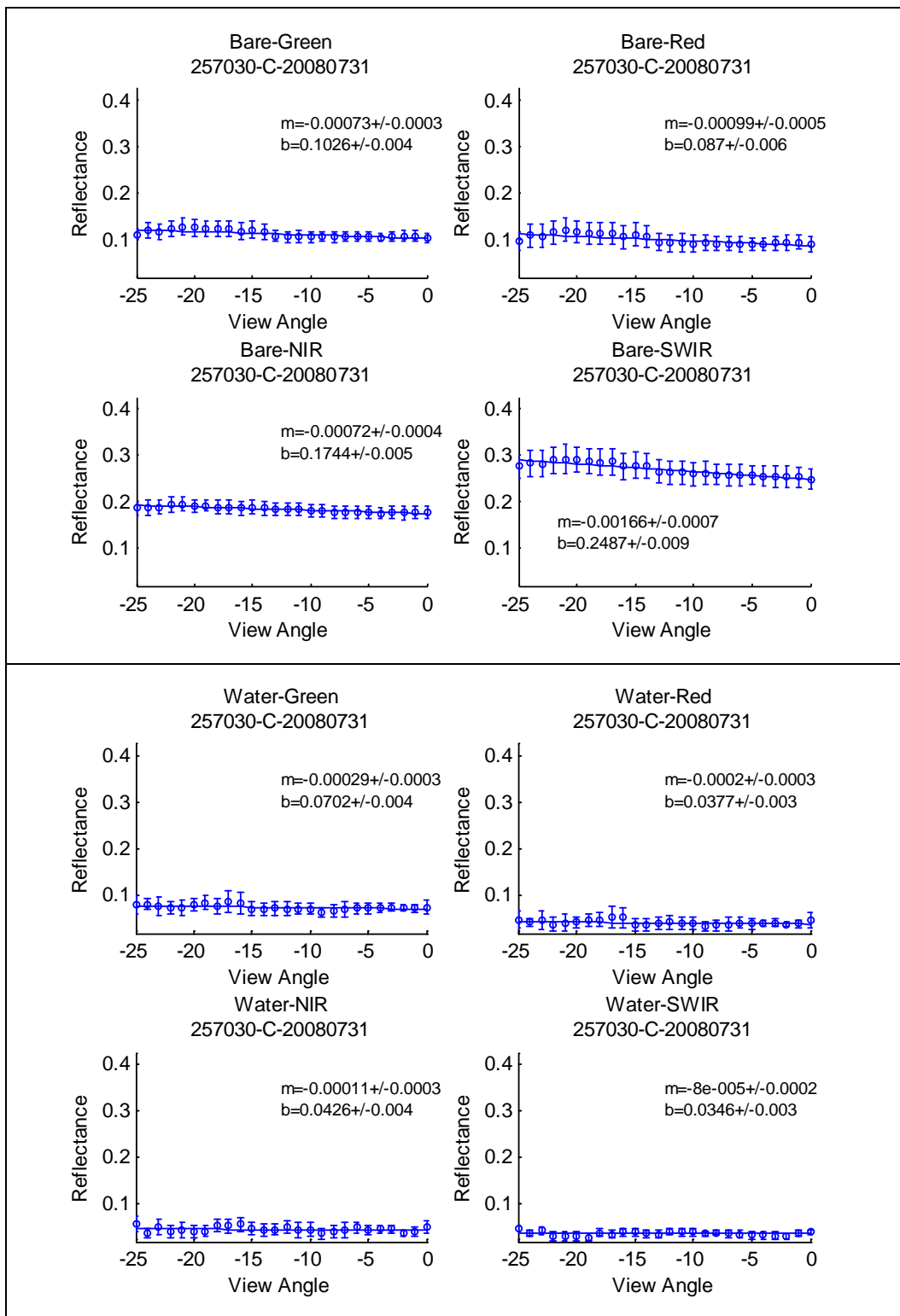




AWiFS Path/Row 257-30 Quad C - Acquired July 31, 2008

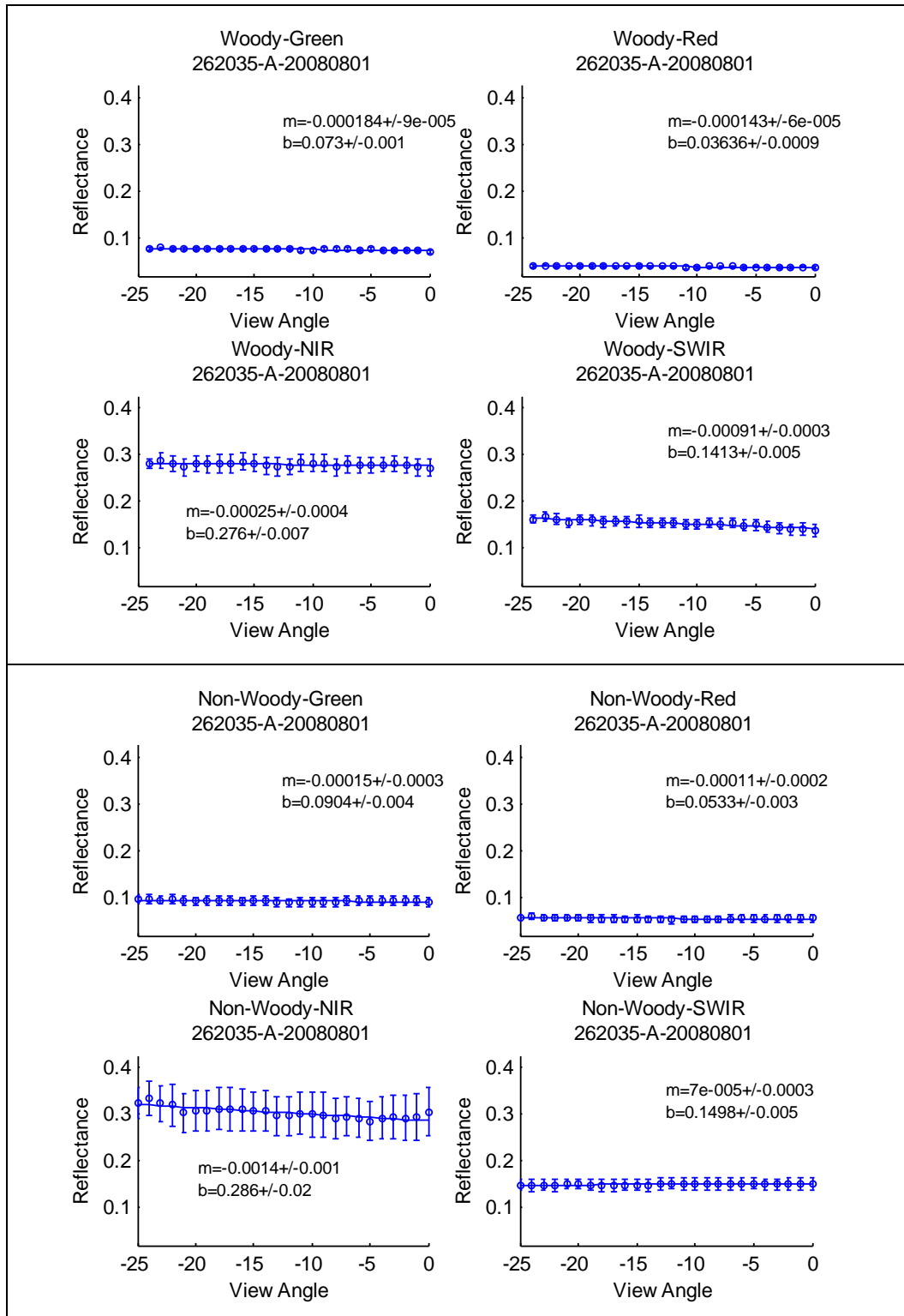
Reflectance as a function of Sensor View Angle based on Maximum Likelihood Classification

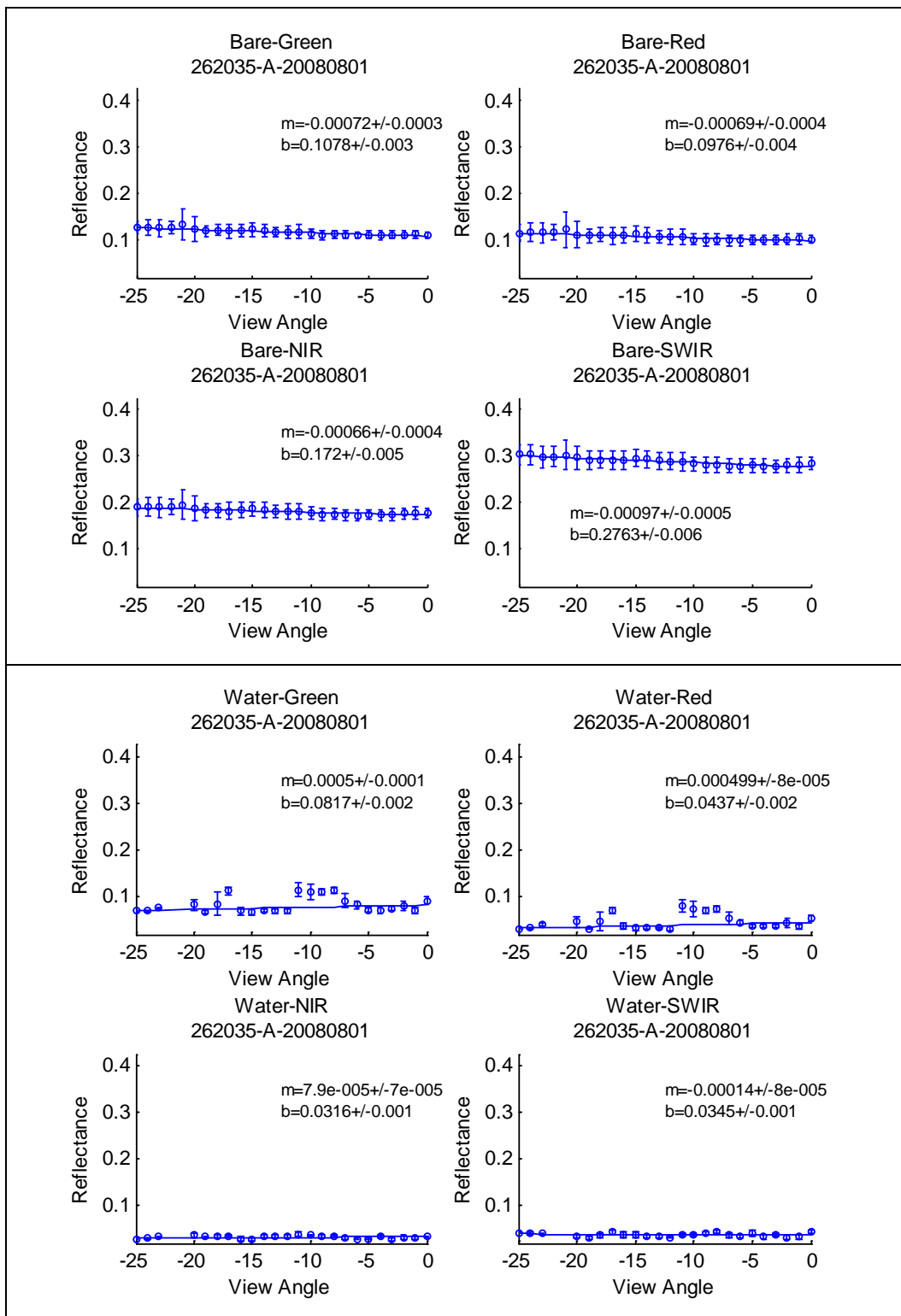




AWiFS Path/Row 262-35 Quad A - Acquired August 1, 2008

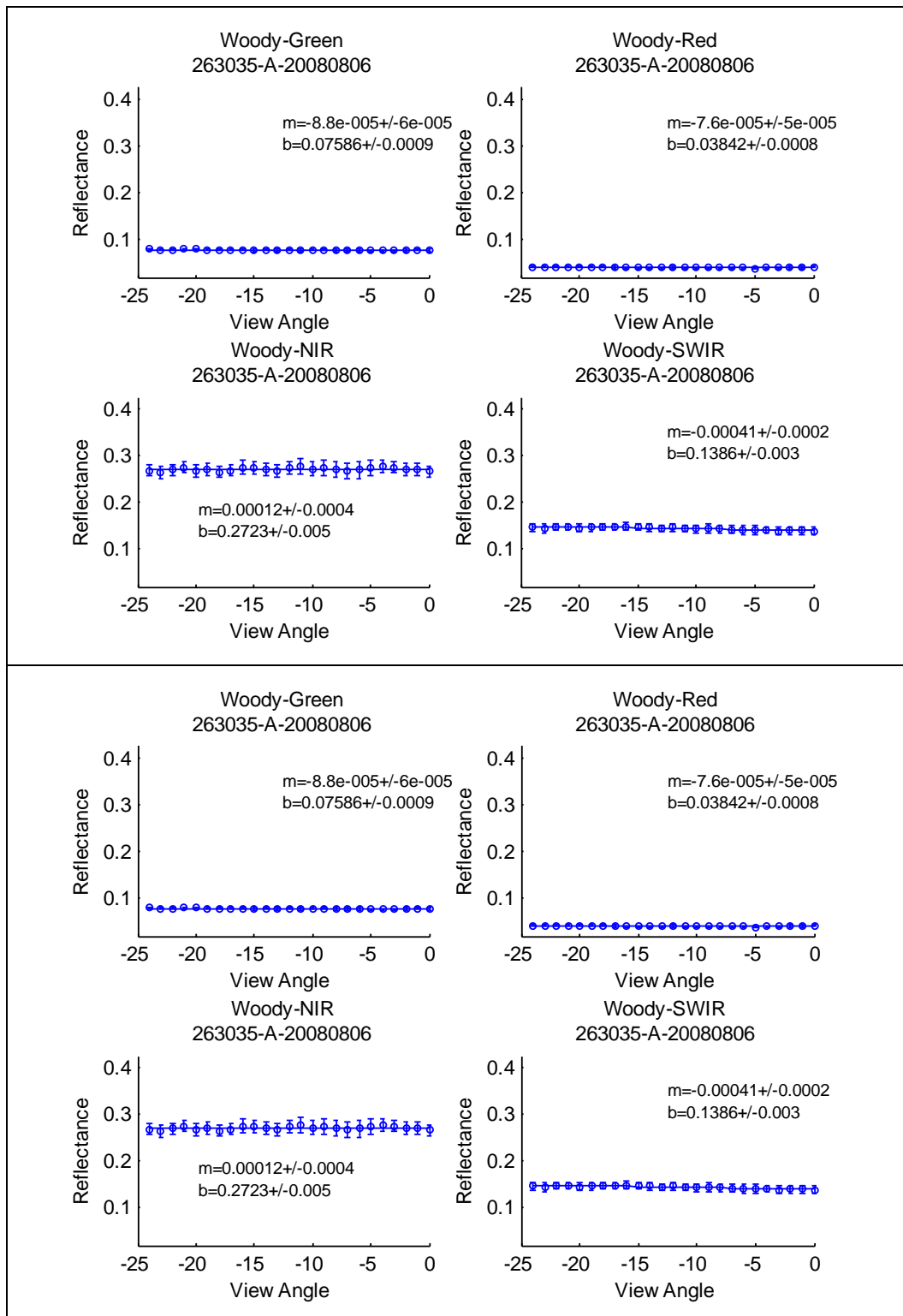
Reflectance as a function of Sensor View Angle based on Maximum Likelihood Classification

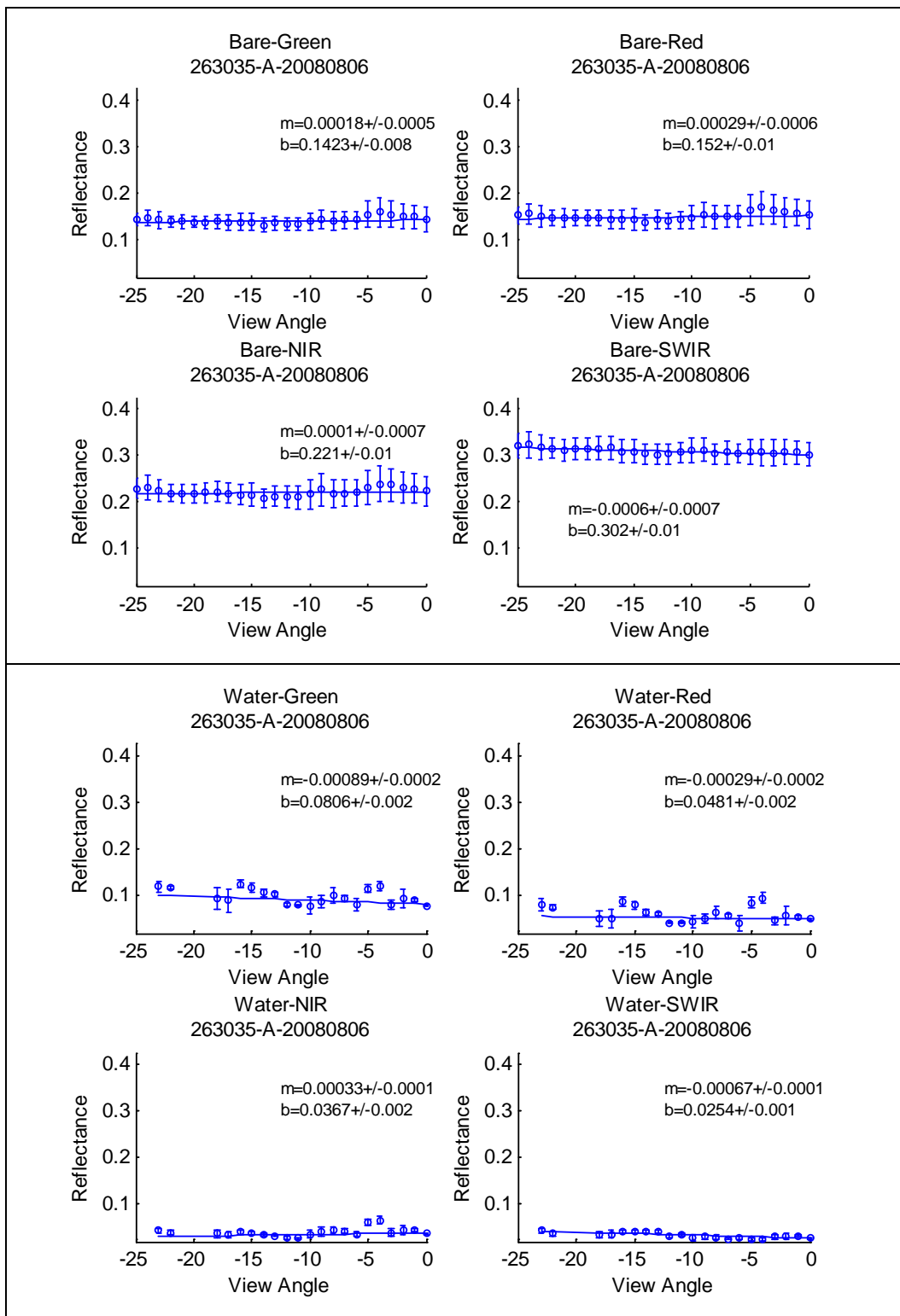




AWiFS Path/Row 263-35 Quad A - Acquired August 6, 2008

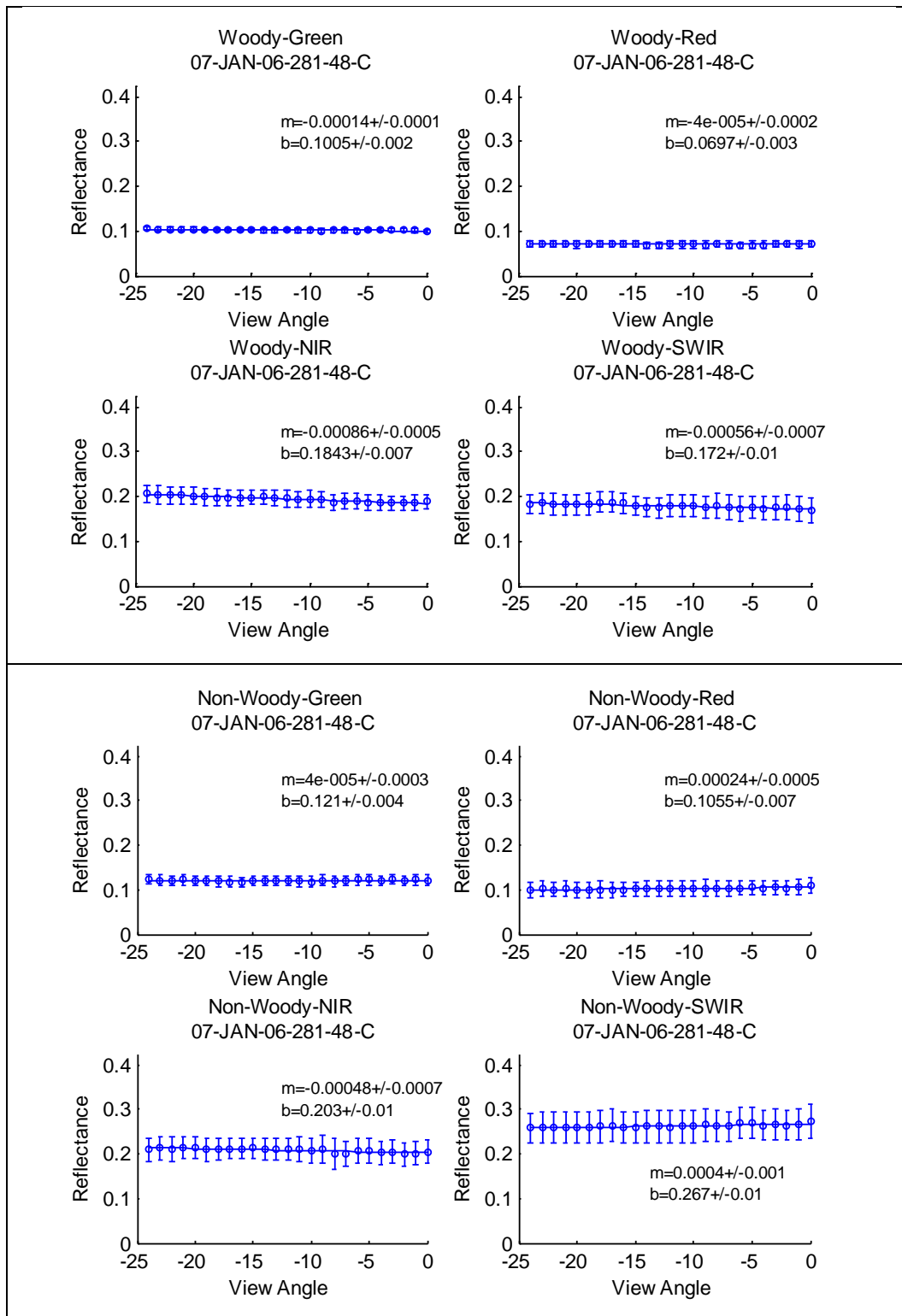
Reflectance as a function of Sensor View Angle based on Maximum Likelihood Classification

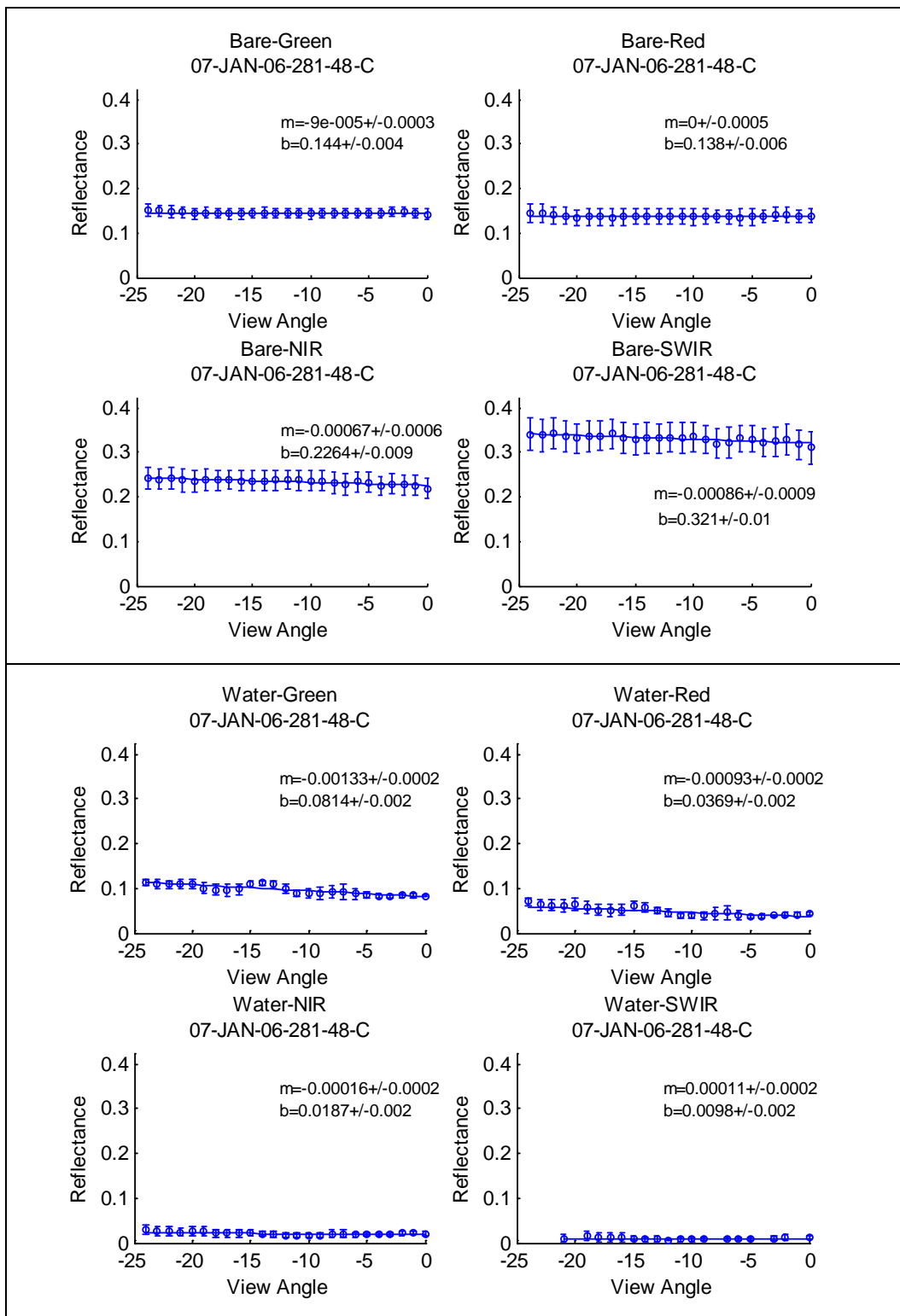




AWiFS Path/Row 281-48 Quad C - Acquired January 7, 2006

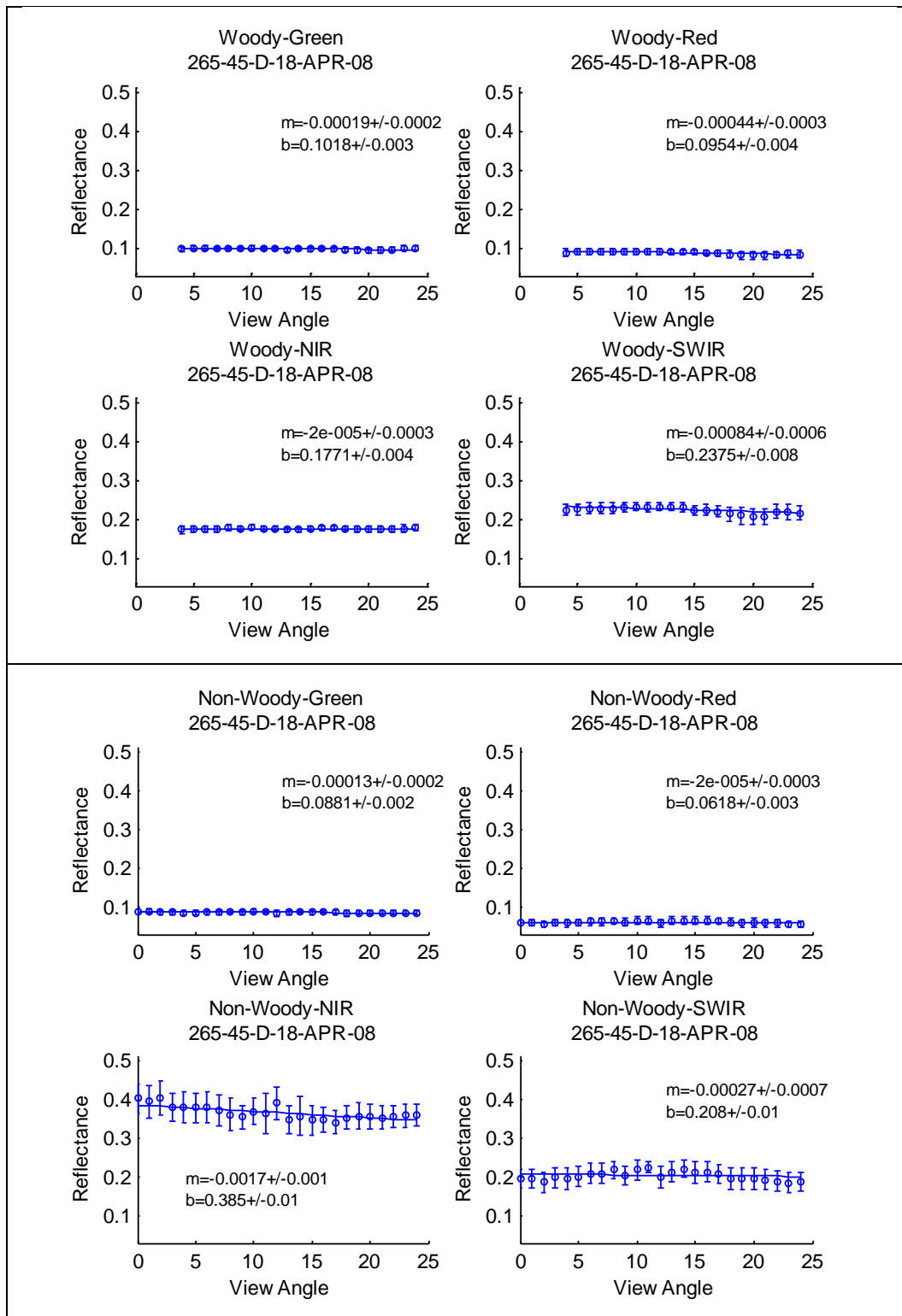
Reflectance as a function of Sensor View Angle based on Maximum Likelihood Classification

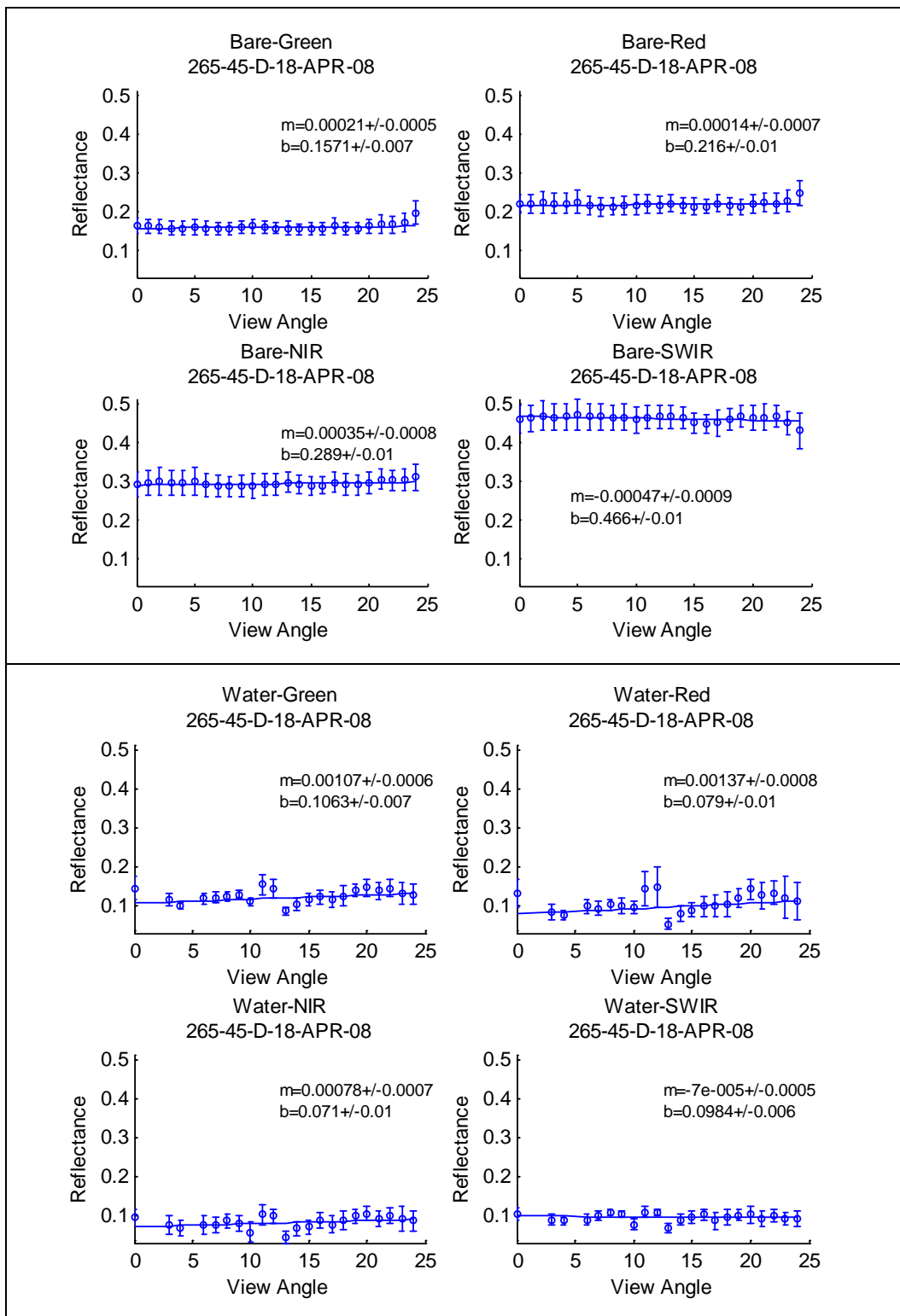




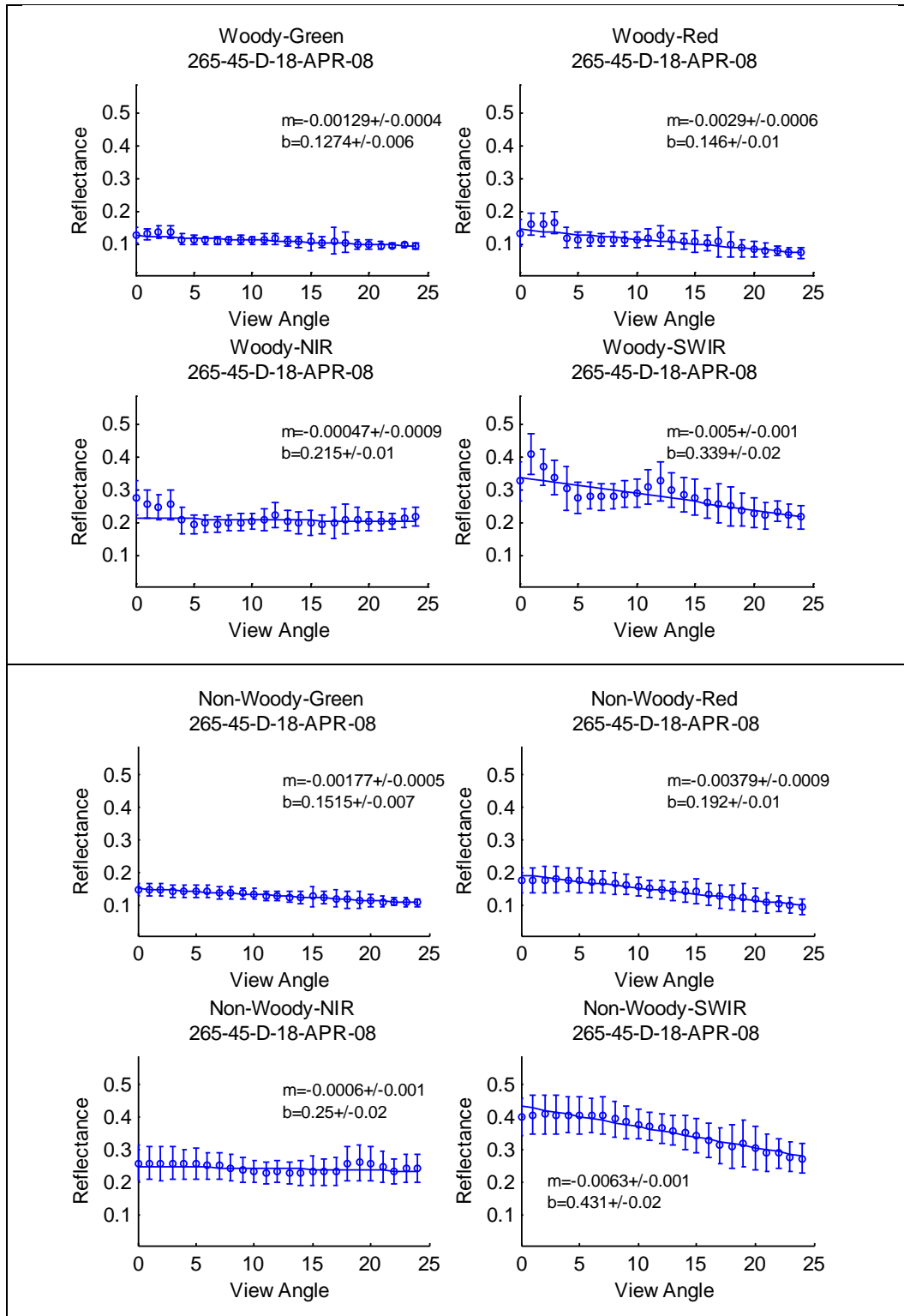
AWiFS Path/Row 265-45 Quad D - Acquired April 18, 2008

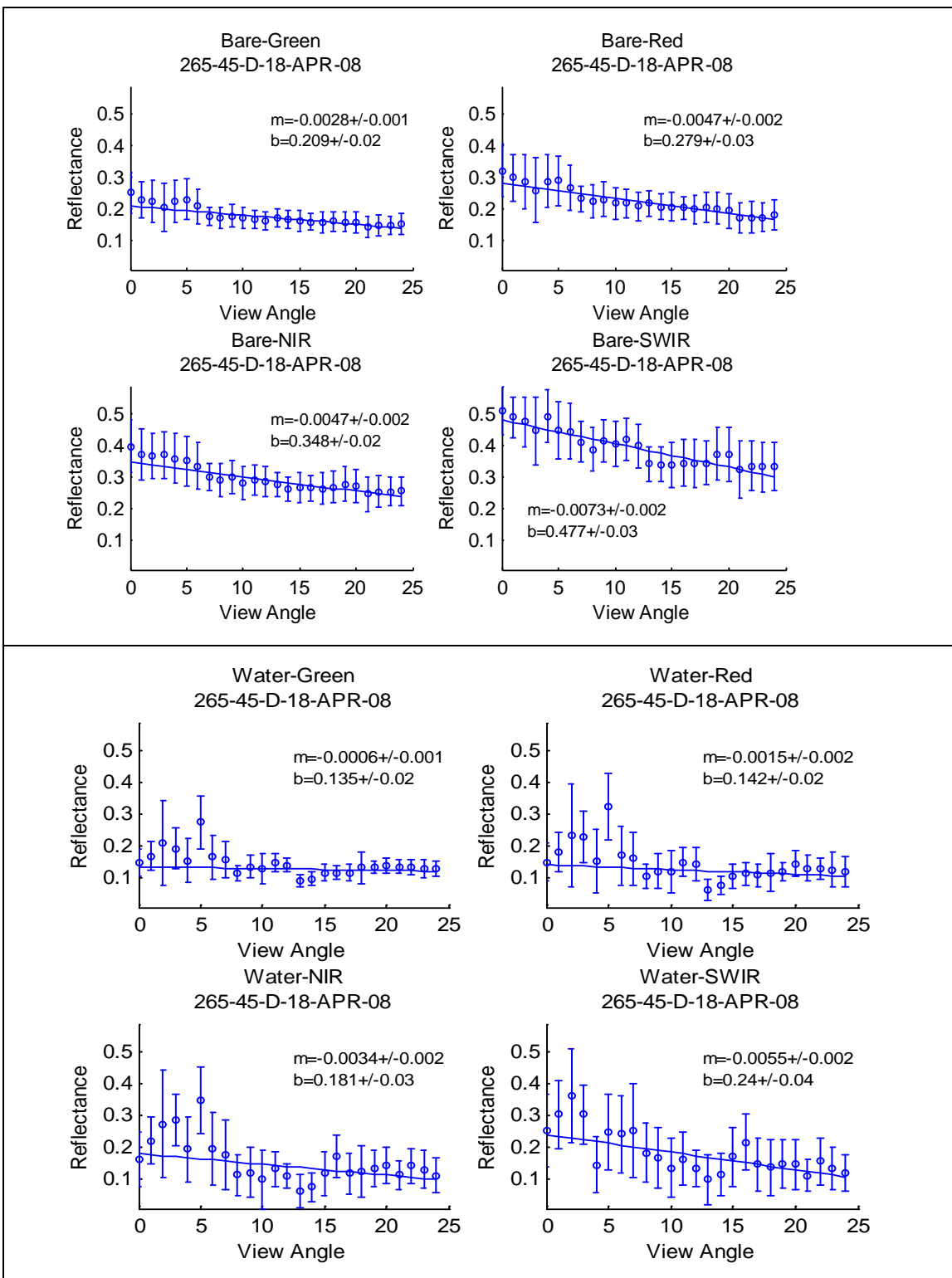
Reflectance as a function of Sensor View Angle based on Maximum Likelihood Classification





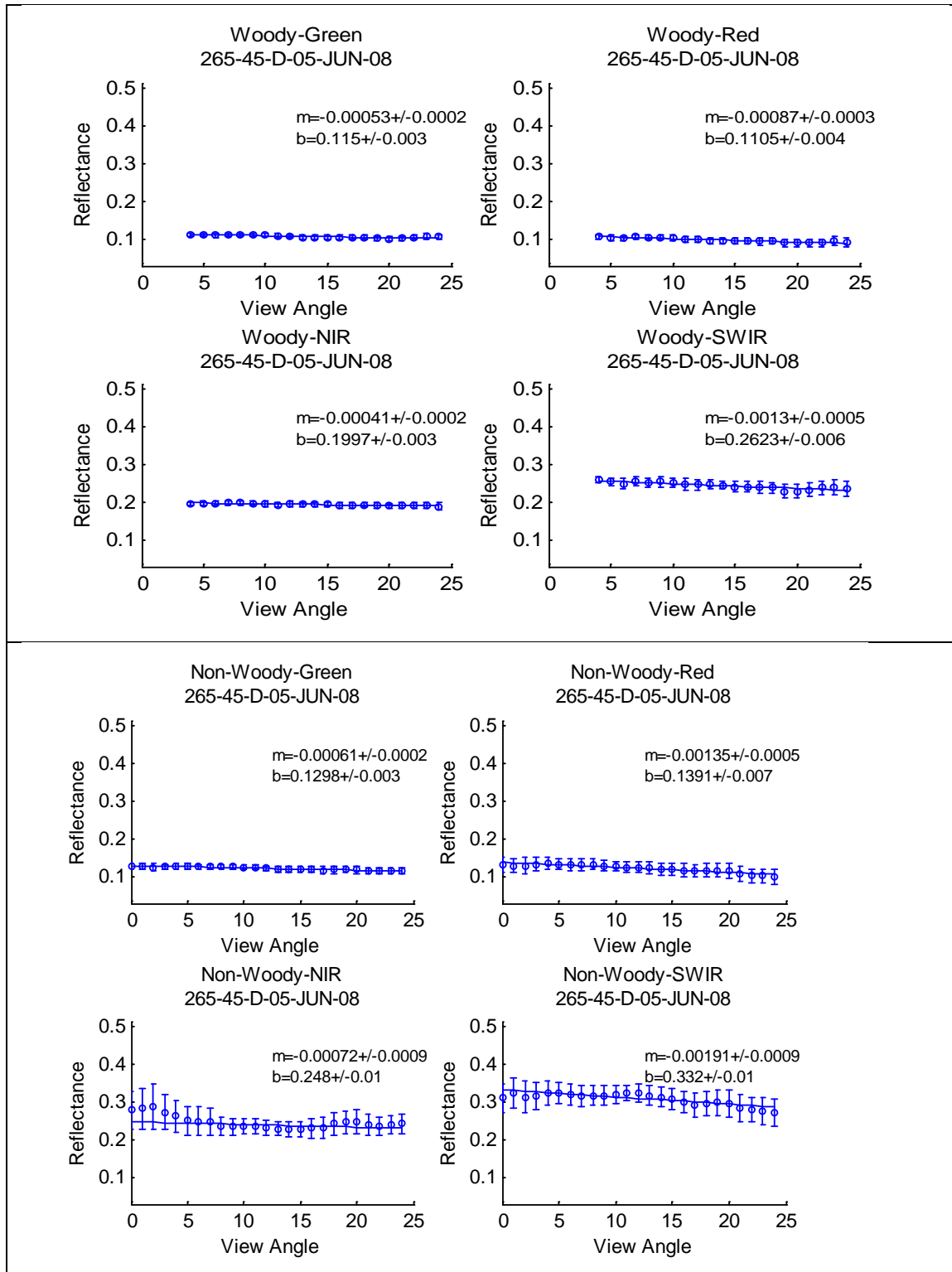
AWiFS Path/Row 265-45 Quad B - Acquired April 18, 2008
Reflectance as a function of Sensor View Angle based on USDA CDL

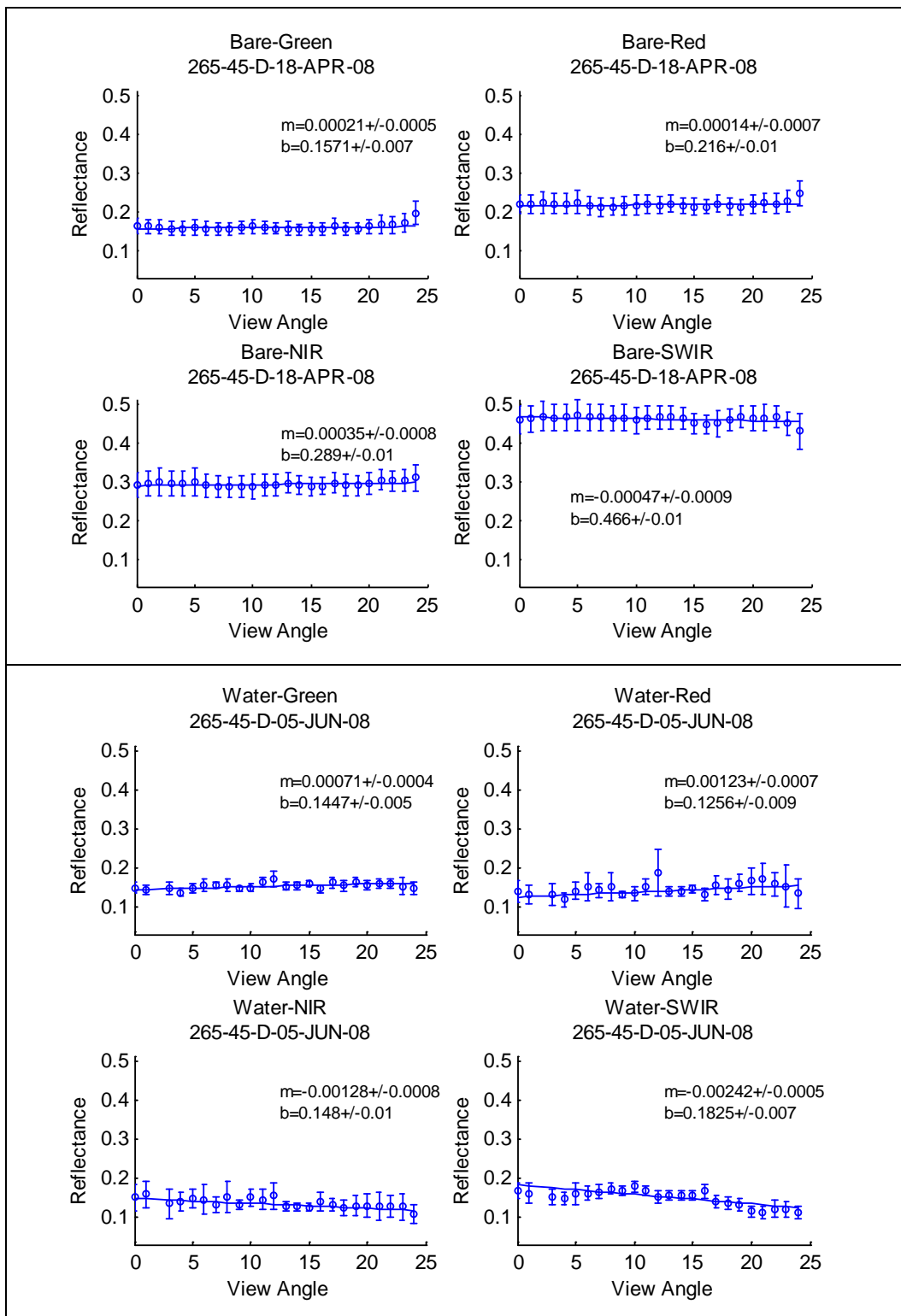




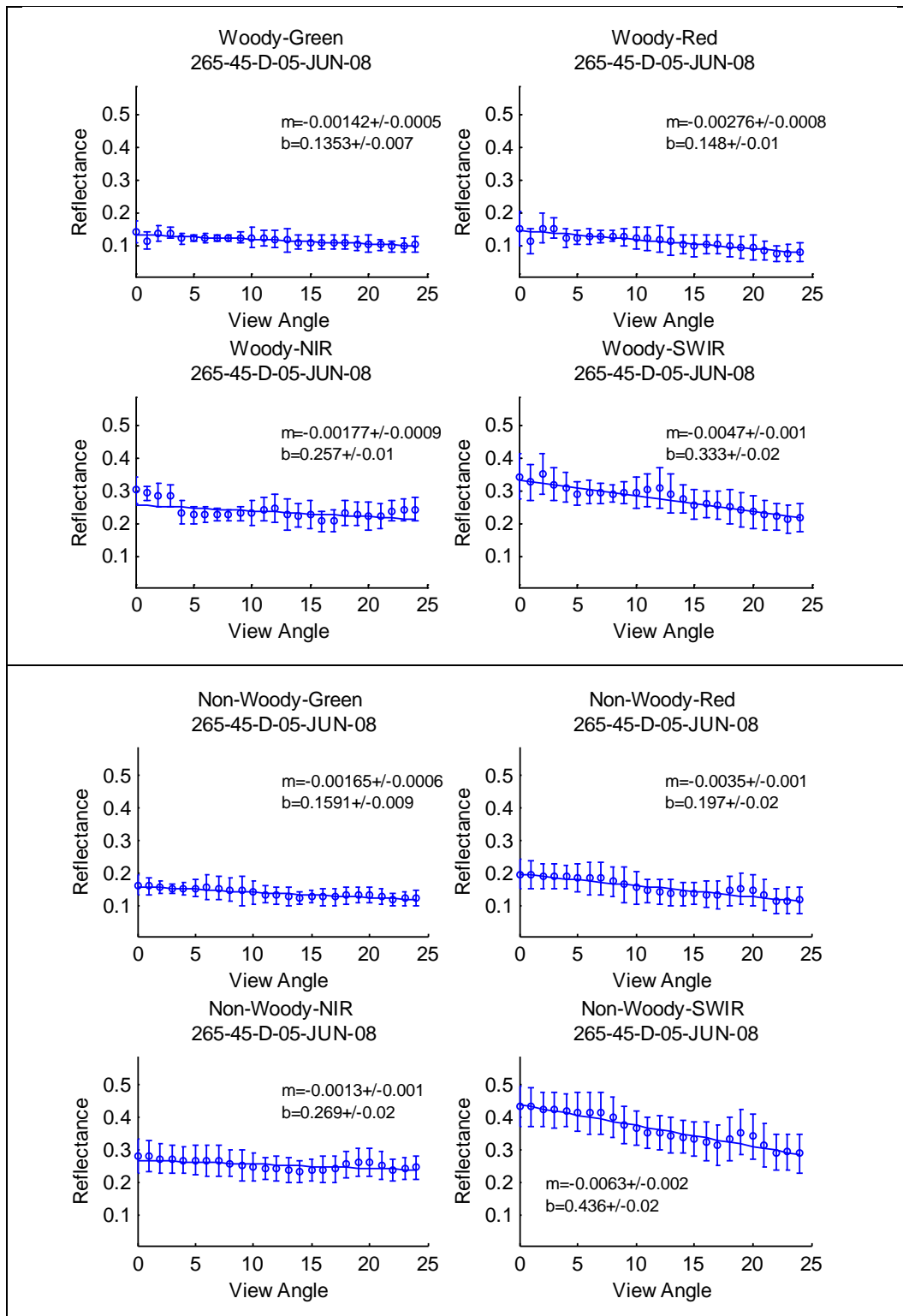
AWiFS Path/Row 265-45 Quad D - Acquired June 5, 2008

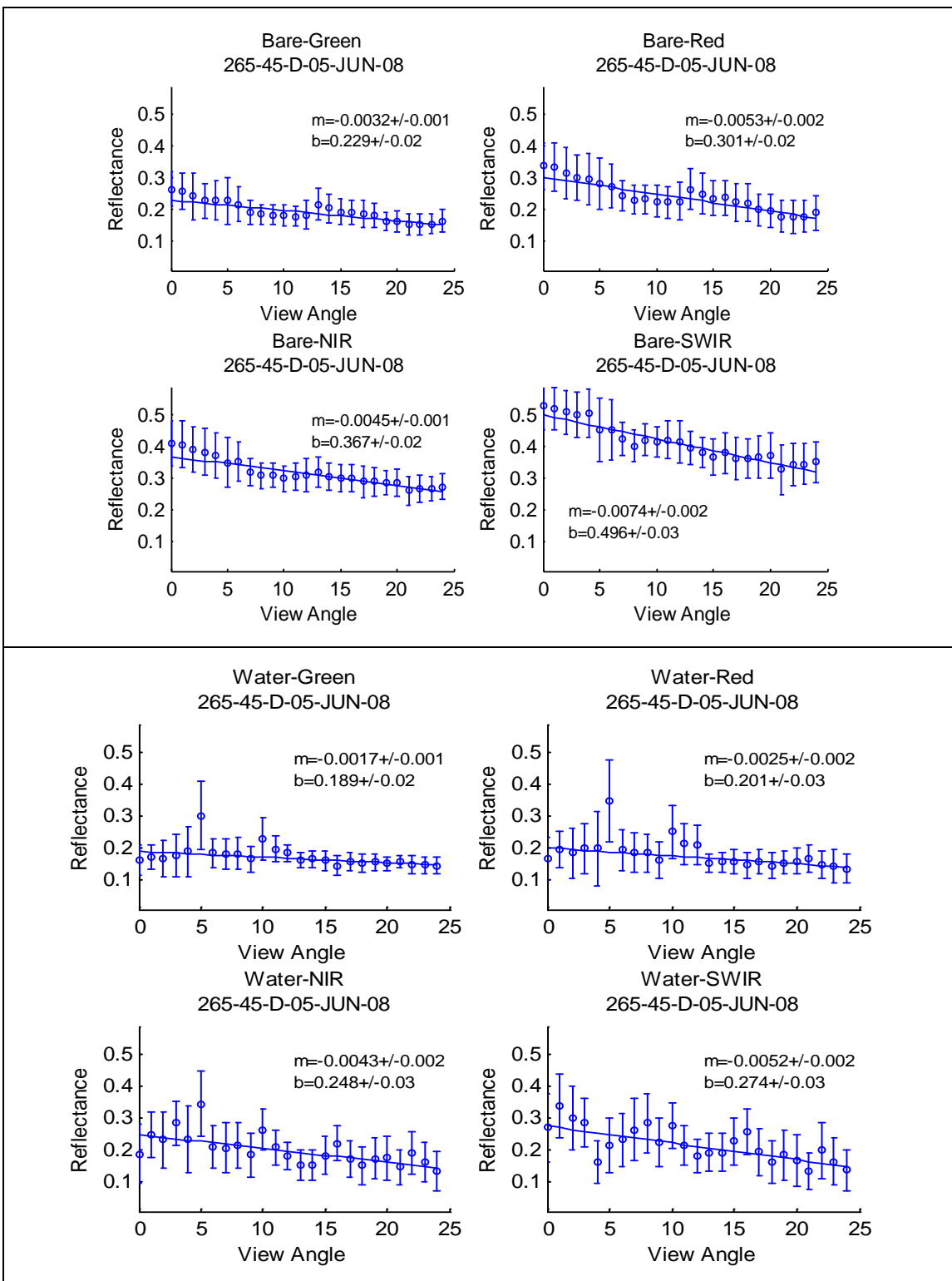
Reflectance as a function of Sensor View Angle based on Maximum Likelihood Classification





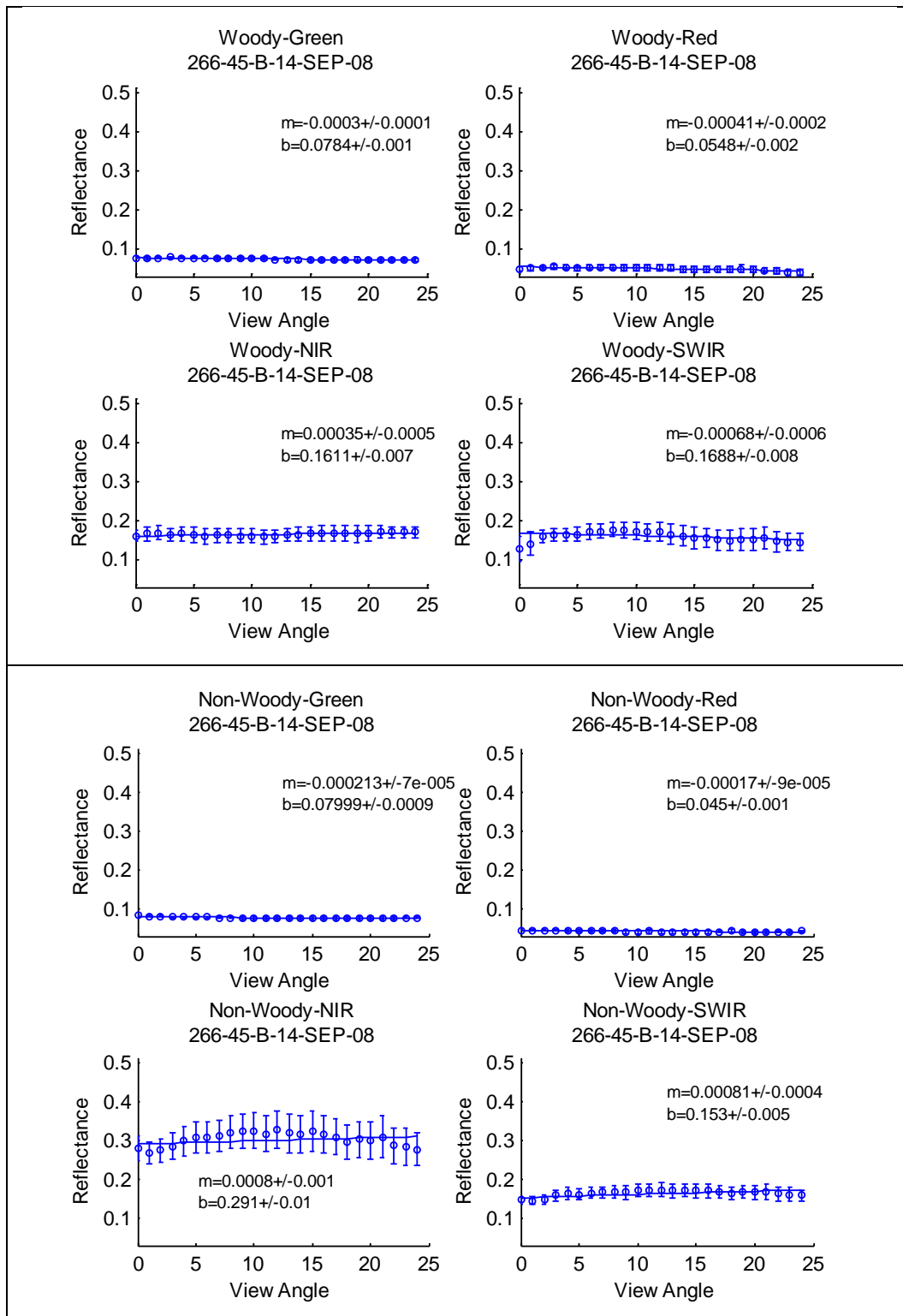
AWiFS Path/Row 265-45 Quad D - Acquired June 5, 2008
Reflectance as a function of Sensor View Angle based on USDA CDL

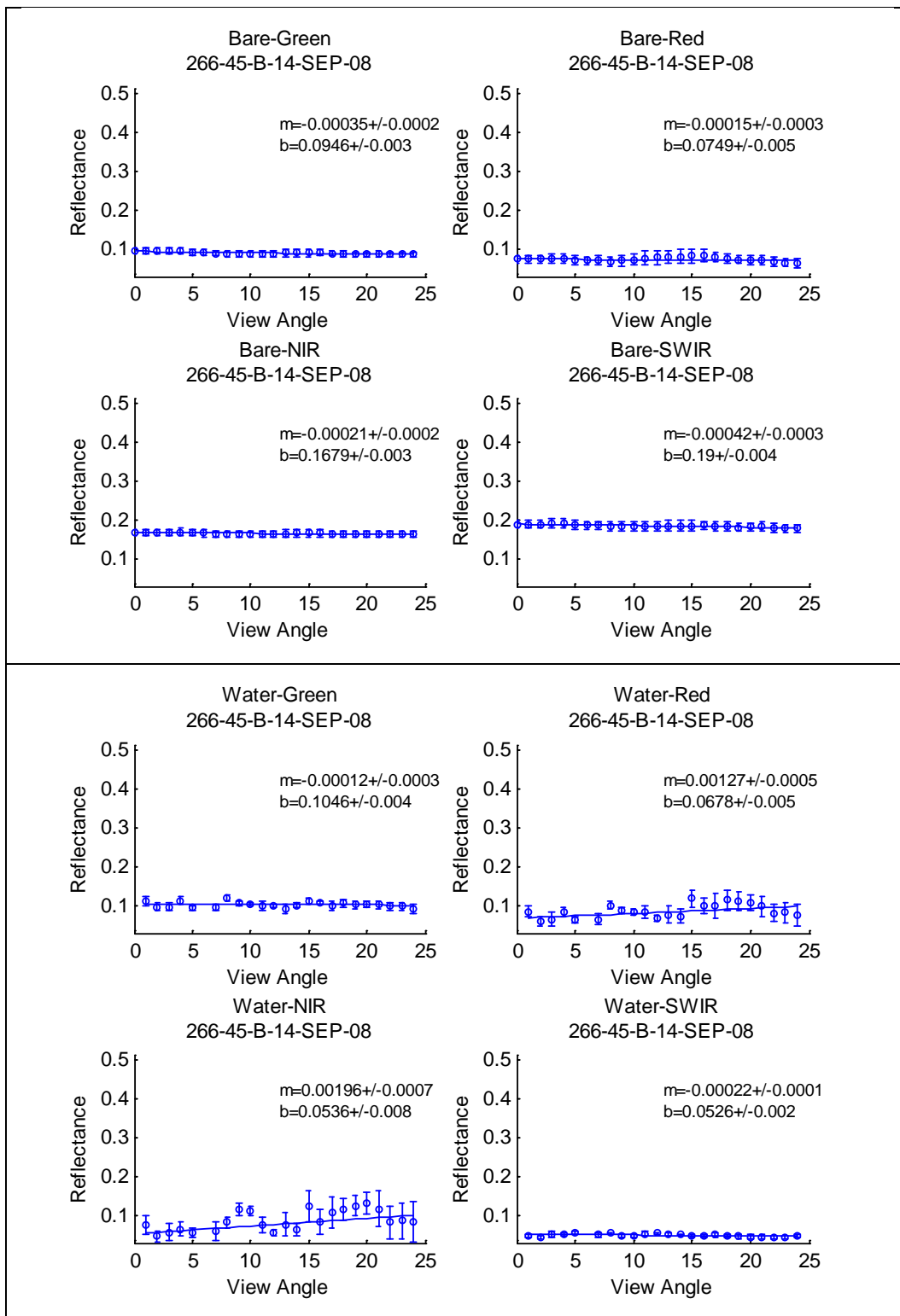




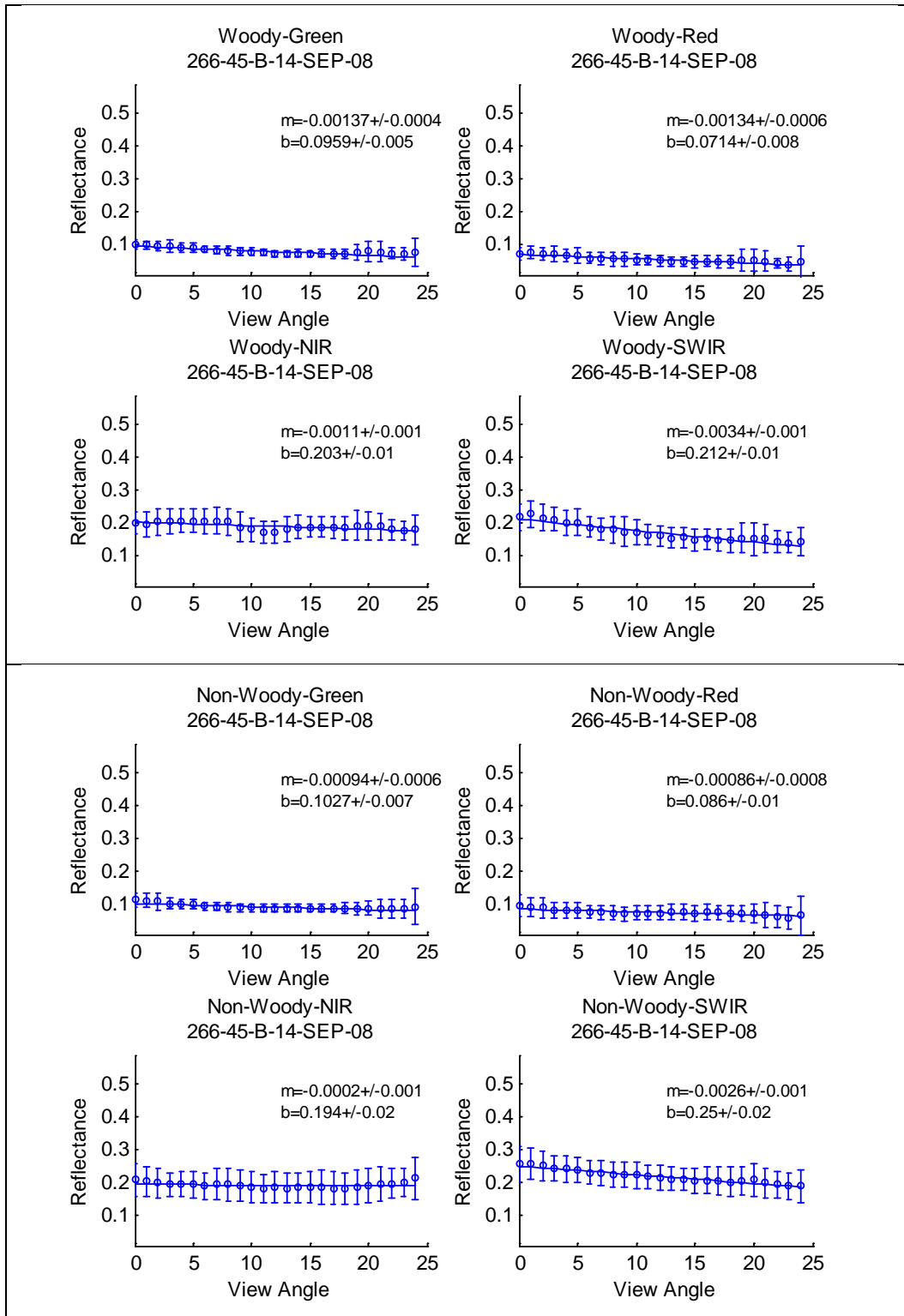
AWiFS Path/Row 266-45 Quad B - Acquired September 14, 2008

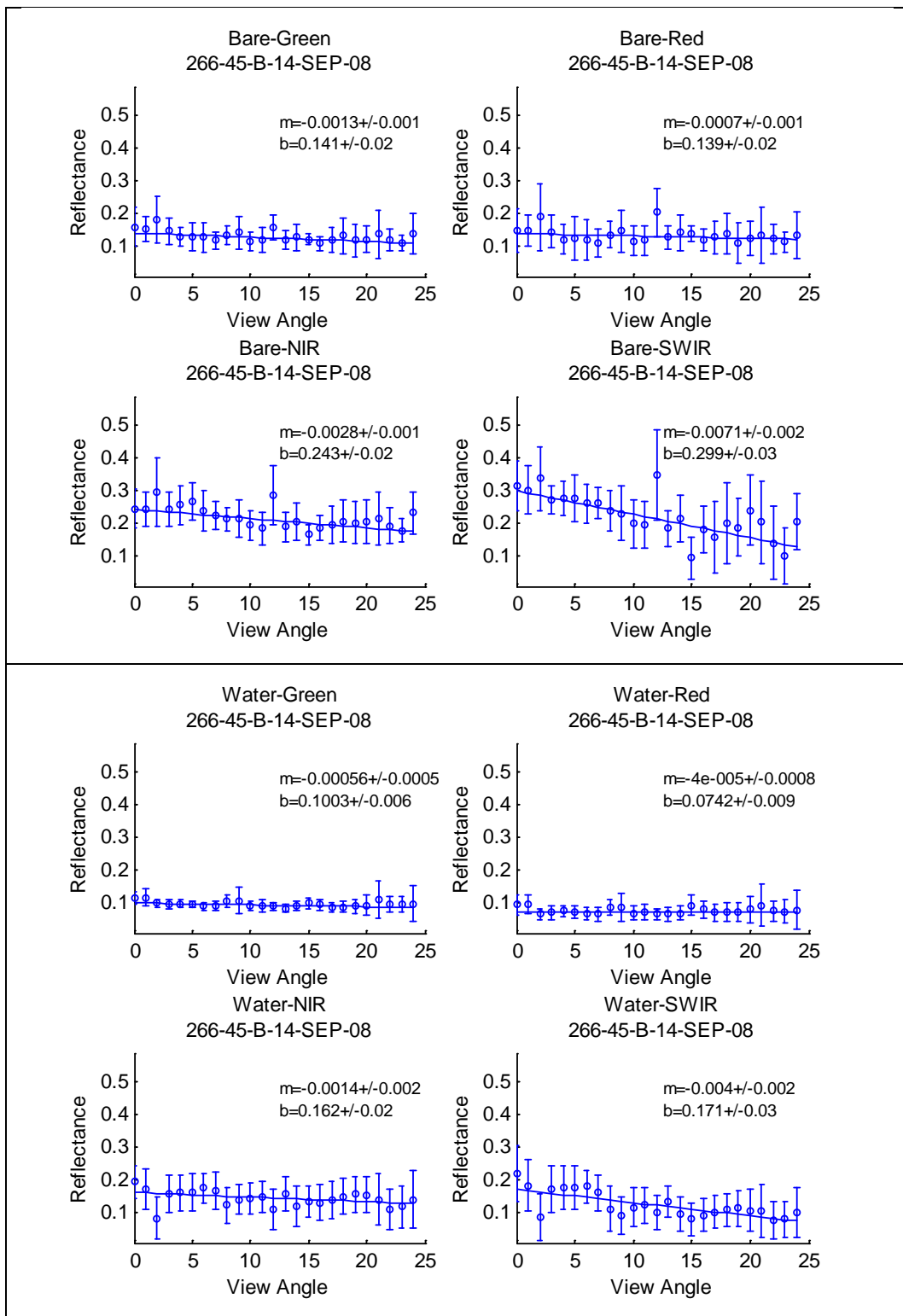
Reflectance as a function of Sensor View Angle based on Maximum Likelihood Classification





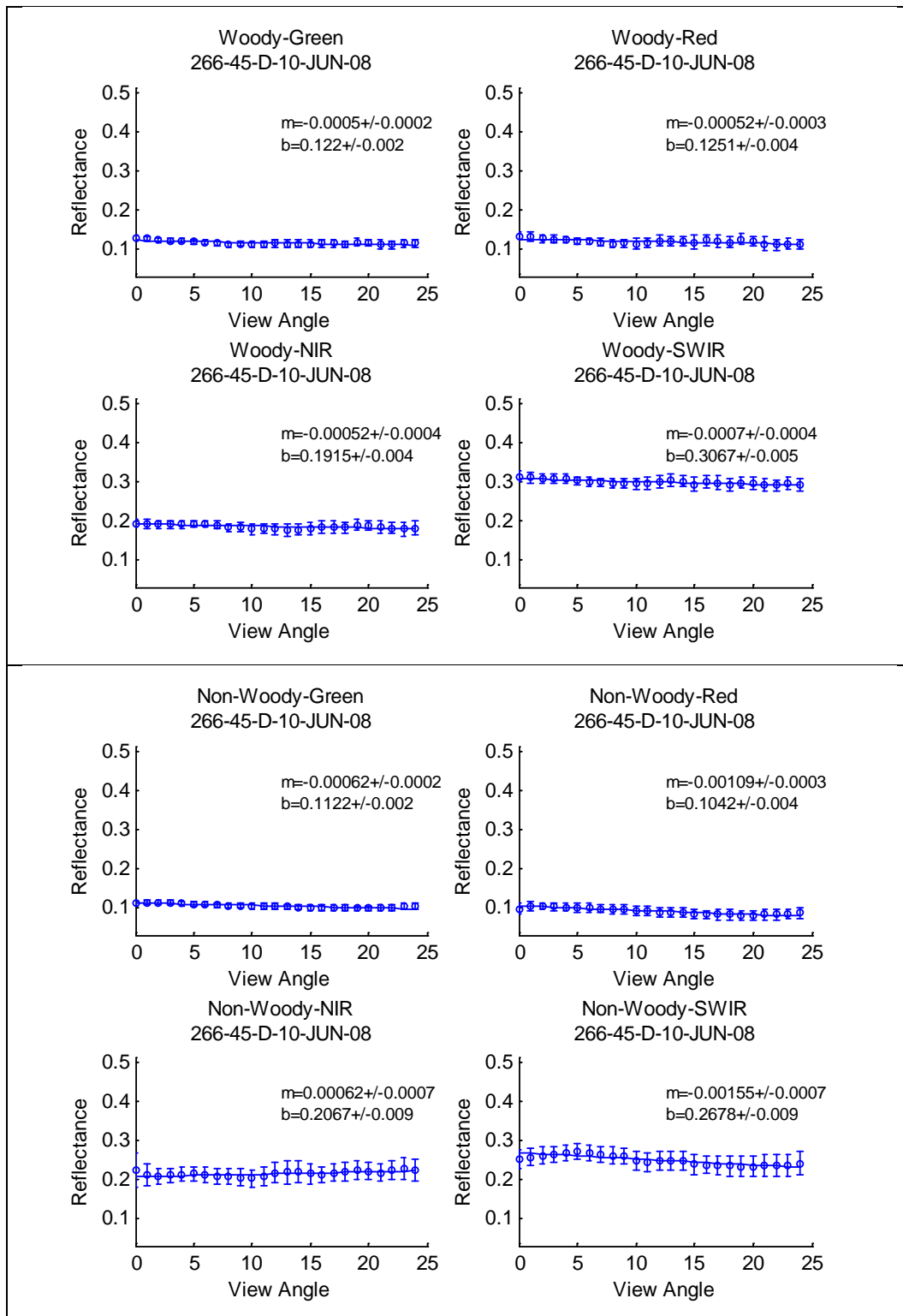
AWiFS Path/Row 266-45 Quad B - Acquired September 14, 2008
 Reflectance as a function of Sensor View Angle based on USDA CDL

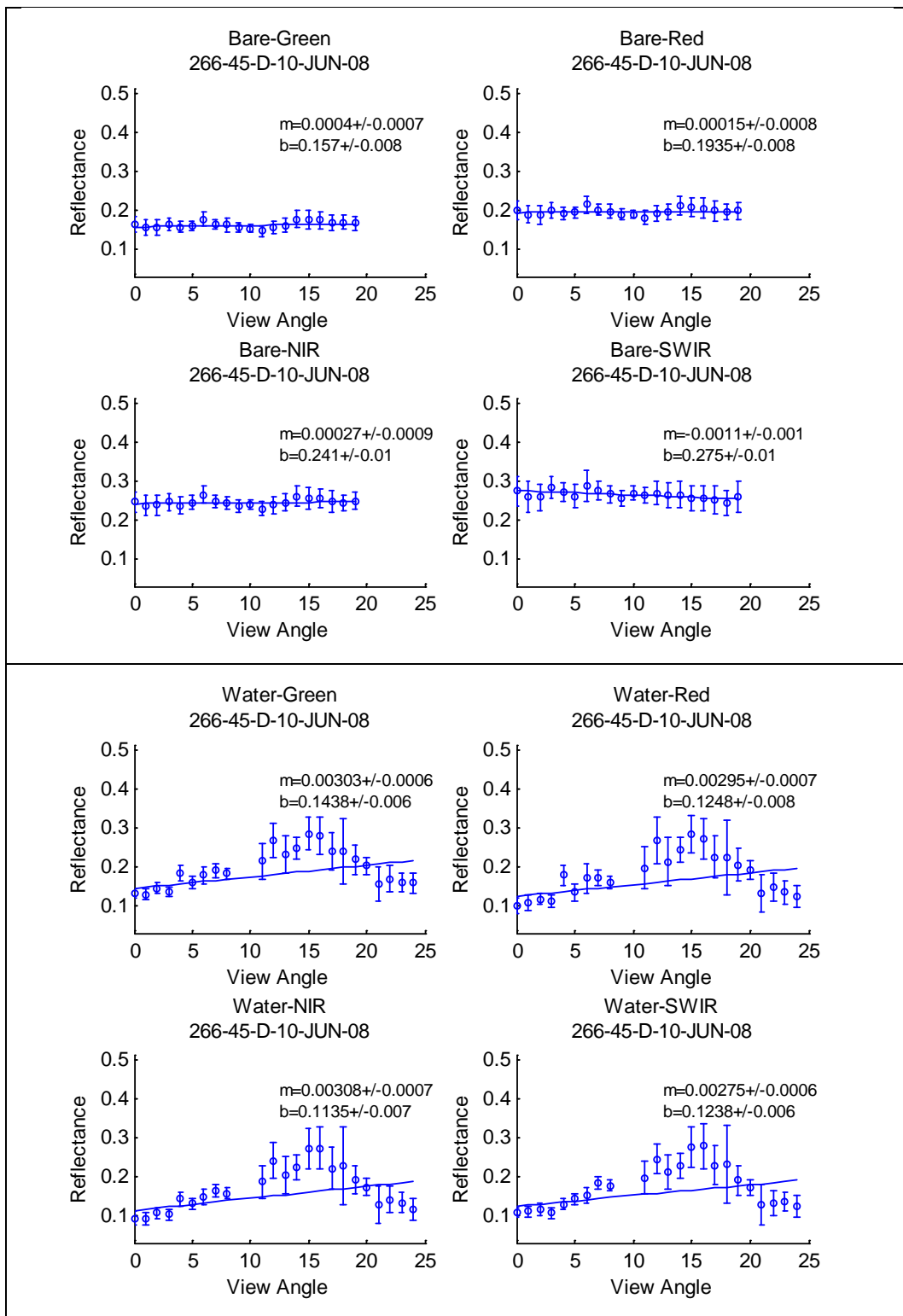




AWiFS Path/Row 266-45 Quad D - Acquired June 10, 2008

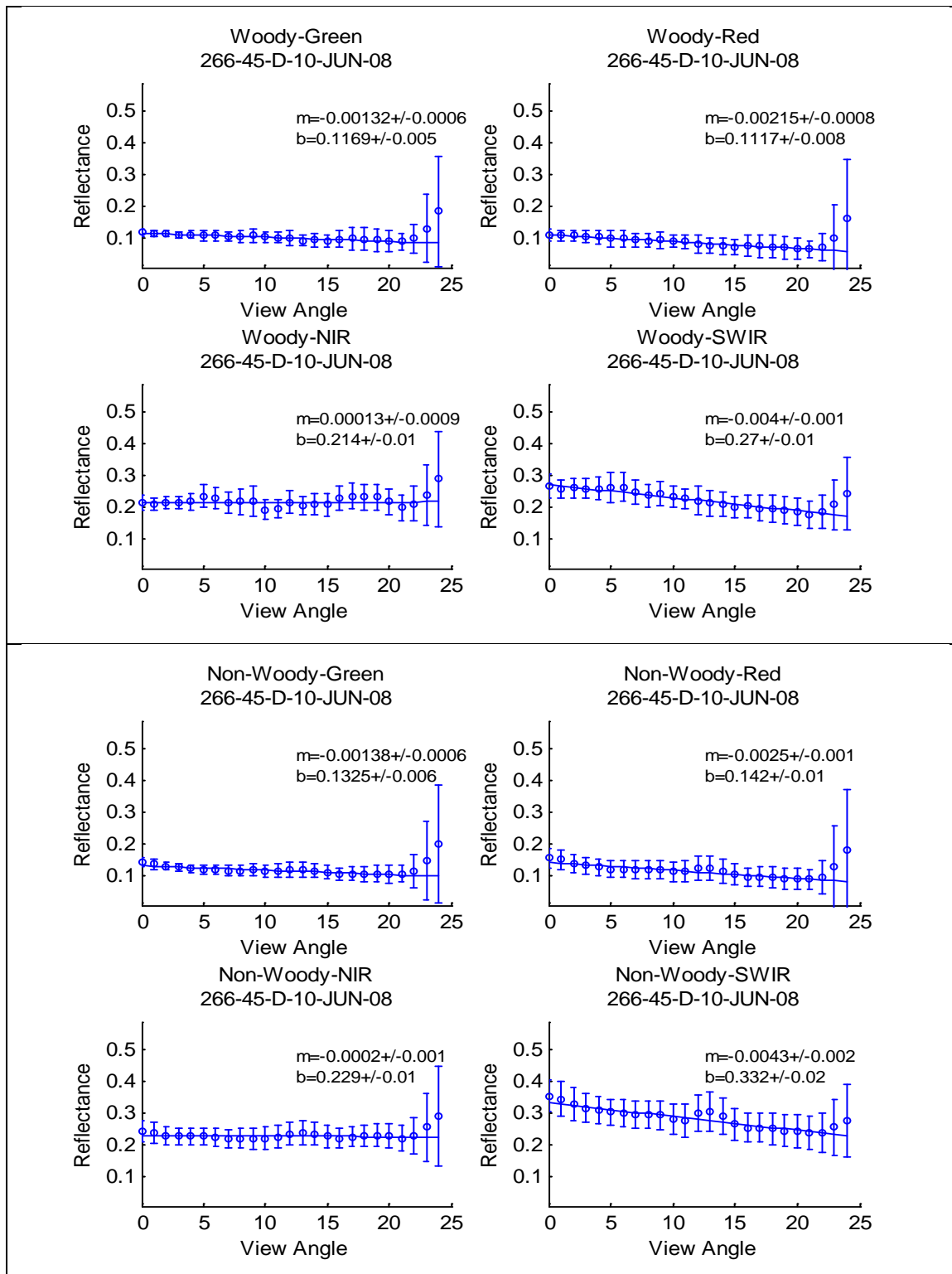
Reflectance as a function of Sensor View Angle based on Maximum Likelihood Classification

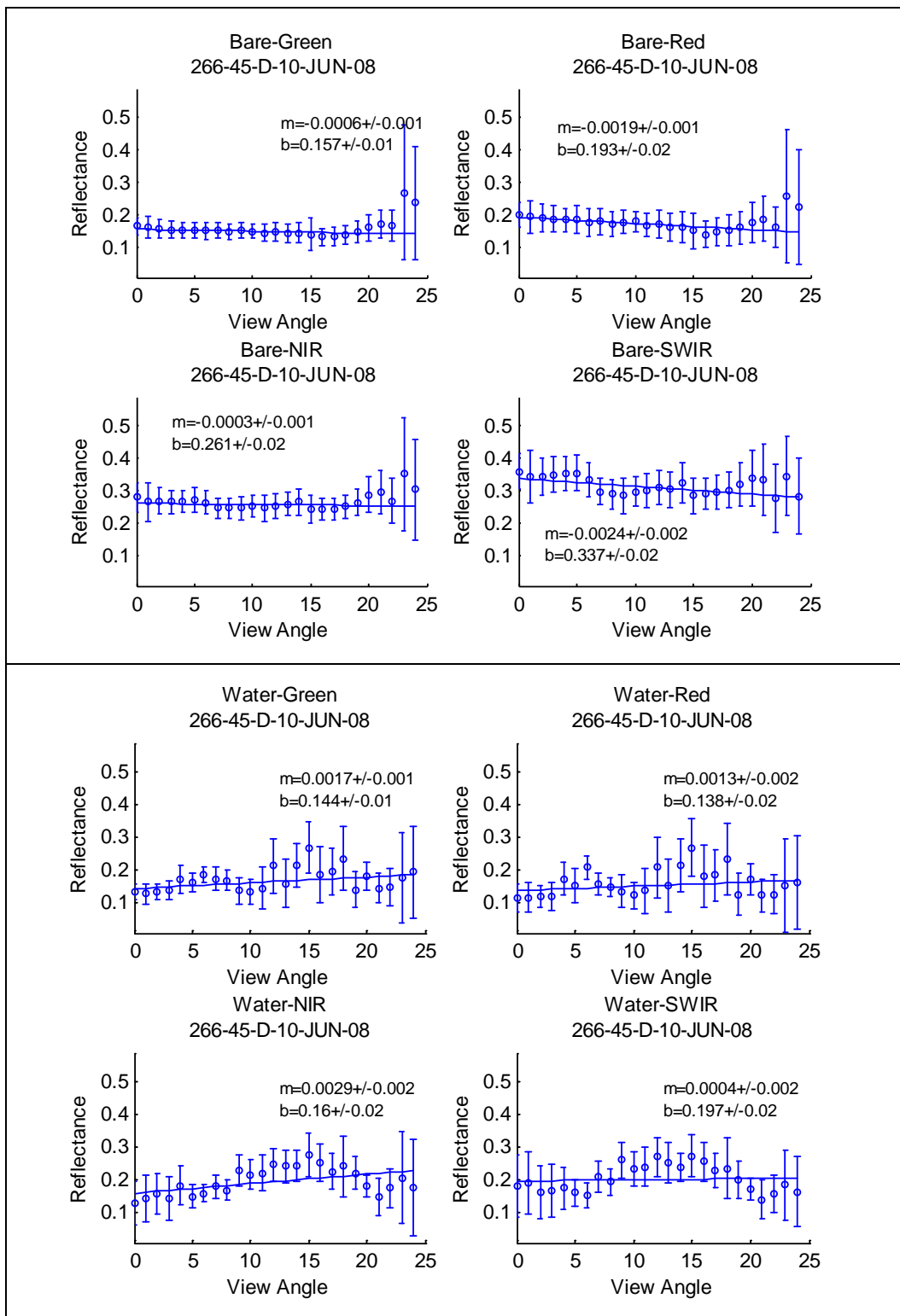




AWiFS Path/Row 266-45 Quad D - Acquired June 10, 2008

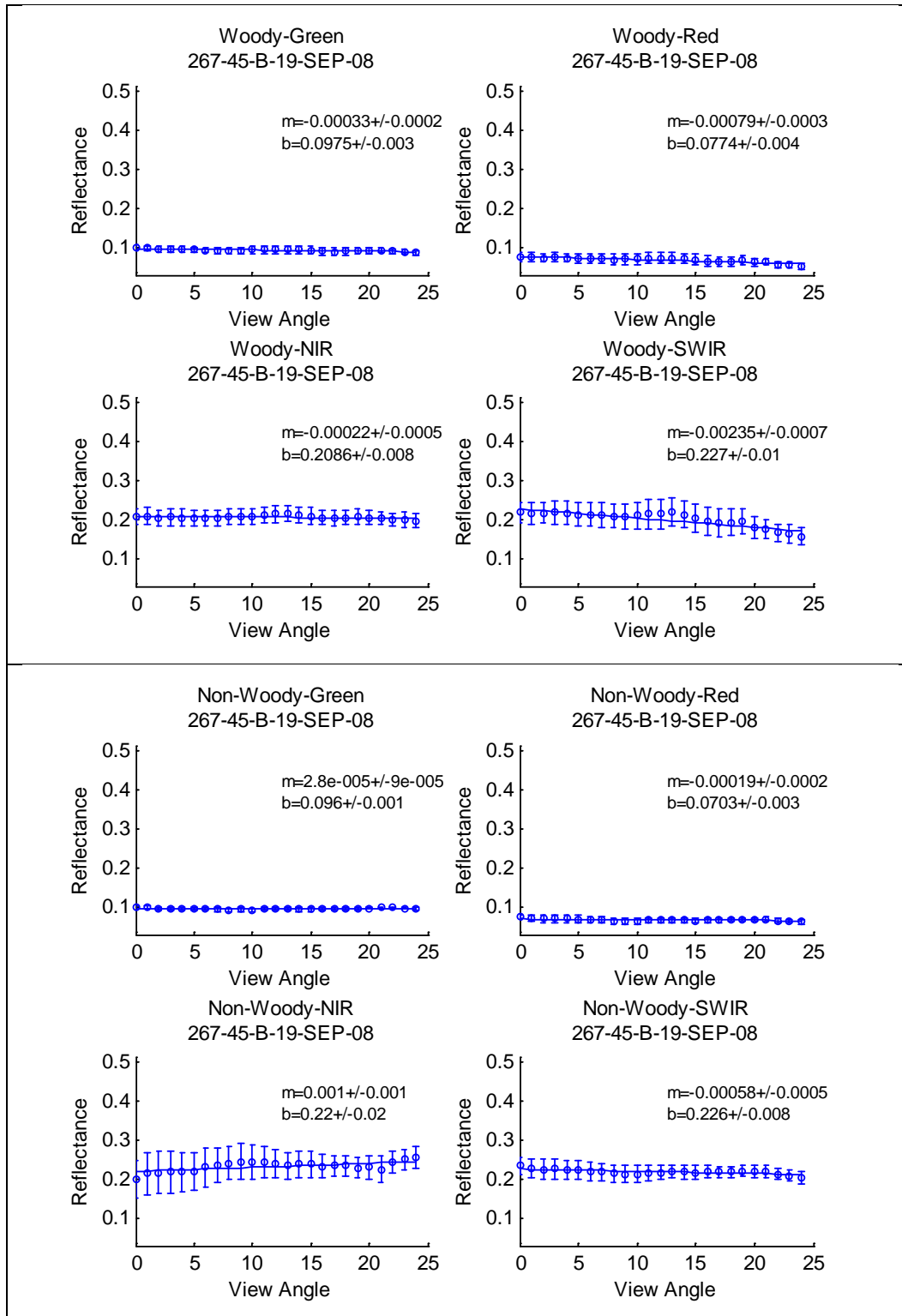
Reflectance as a function of Sensor View Angle based on USDA CDL

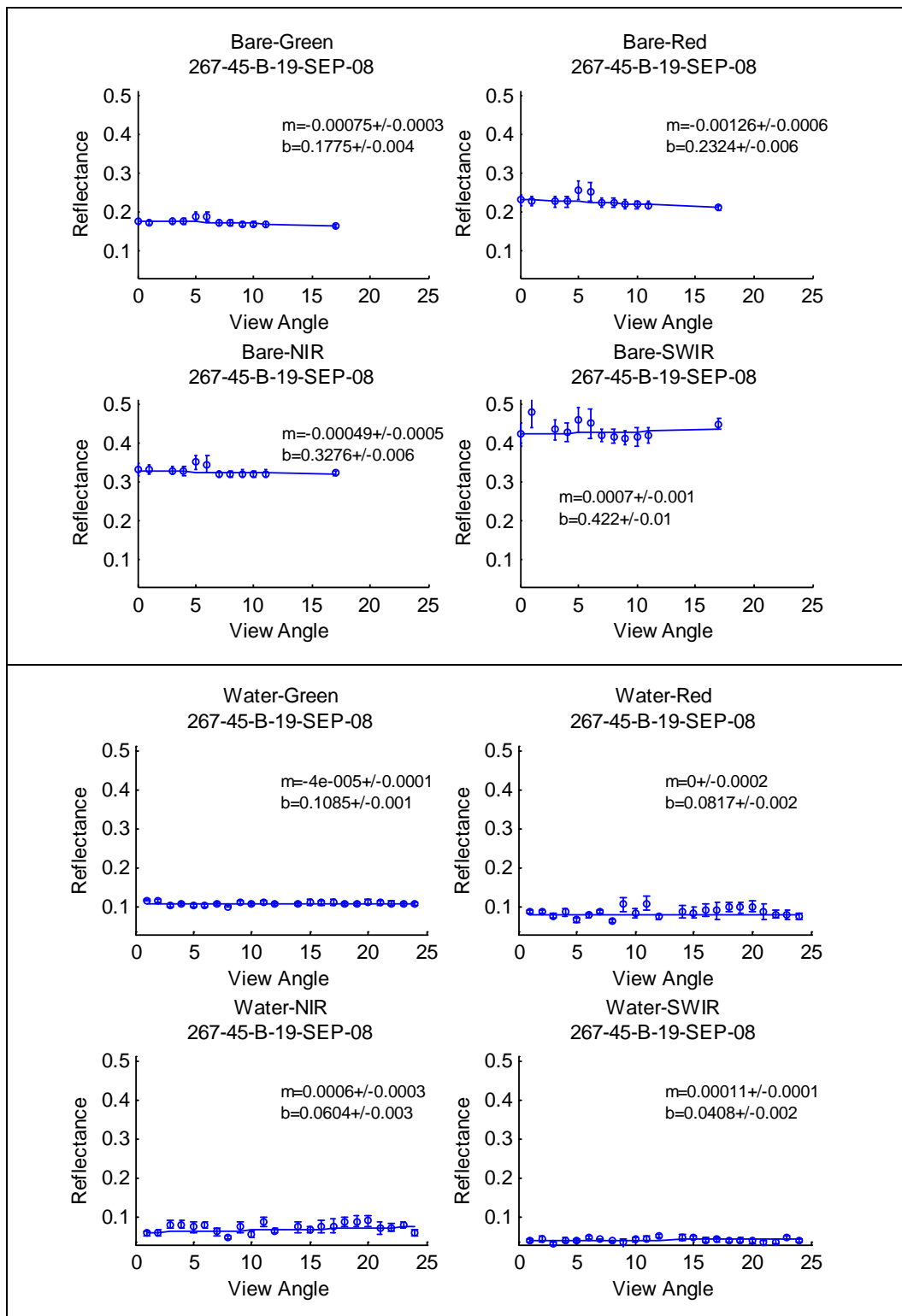




AWiFS Path/Row 267-45 Quad B - Acquired September 19, 2008

Reflectance as a function of Sensor View Angle based on Maximum Likelihood Classification





AWiFS Path/Row 267-45 Quad B - Acquired September 19, 2008
Reflectance as a function of Sensor View Angle based on USDA CDL

